N O T I C E

THIS DOCUMENT HAS BEEN REPRODUCED FROM MICROFICHE. ALTHOUGH IT IS RECOGNIZED THAT CERTAIN PORTIONS ARE ILLEGIBLE, IT IS BEING RELEASED IN THE INTEREST OF MAKING AVAILABLE AS MUCH INFORMATION AS POSSIBLE

NASA Contractor Report 156859

Shape of the Ocean Surface and Implications for the Earth's Interior

Final Report of GEOS-3 Results

M. E. Chapman,
M. Talwani,
H. Kahle,
and
J. H. Bodine

November 1979

NASA

National Aeronautics and
Space Administration

Wallops Flight Center
Wallops Island, Virginia 23337
AC 804 824-3411

National Aeronautics and
Space Administration

Wallops Flight Center
Wallops Island, Virginia
23337

NASA

Reply to Attn of: TL (A-13)

JAN 24 1980

NASA Scientific and Technical
  Information Facility
Attn: Acquisitions Branch
Post Office Box 8757
Baltimore/Washington International
  Airport, MD   21240

Subject: Document Release for NASA CR-156859

Document Release Authorization Form FF 427 and two (2) copies
of the following report are forwarded:

         NASA CR-156859 Shape of the Ocean Surface
         and Implications for the Earth's Interior

We are forwarding, under separate cover, thirty (30)
additional copies of the subject report.

James C. Floyd
James C. Floyd
Head, Administrative Management Branch

Enclosures

Shape of the Ocean Surface and Implications for the Earth's Interior

Final Report of GEOS-3 Results

M. E. Chapman, M. Talwani, H. Kahle, and J. H. Bodine
Lamont-Doherty Geological Institute
Columbia University
Palisades, New York 10964

NASA
National Aeronautics and
Space Administration

TABLE OF CONTENTS

INTRODUCTION

An ancient problem which has intrigued mankind concerns the shape of the planet on which men reside. How big is the Earth and what shape does it have? To answer this question people developed the science of geodesy, the study of the shape and size of the Earth. Traditionally this field has often been isolated from other branches of Earth science, its goal being narrowly defined as the precise determination of the figure of the Earth and distances thereon. As the general shape has been known for quite some time, this principal question has been repeatedly answered with successively better accuracy. At this time however, geodetic research is undergoing a transition towards greater interaction with other Earth sciences such as geophysics and physical oceanography. This change is due to new advances in technology, specifically to the development of radar altimeters mounted on board Earth orbiting satellites. These instruments are capable of mapping the shape of the ocean surface and providing accurate estimates of the geoid height. Such an advance promises to yield new and exciting information about the Earth. As always though in any new field of research there are basic problems and questions prior to any new discoveries. In this thesis such fundamental questions are first addressed, and then this information on the shape of the ocean surface is utilized to make new inferences about the internal structure of the Earth.

For centuries mathematical geodesists have been able to calculate the shape of the Earth. If the internal density distribution is known then an appropriate differential equation can be solved for the ellipticity of the Earth. Alternatively after measurement of the gravity field on the surface of the Earth, Stokes' formula can be utilized to calculate the geoid. The geoid is defined as a gravitational equipotential

surface which most nearly coincides with mean sea level. Quite often it is termed the shape of the Earth.

Rather than calculation of this shape, an alternate approach is the direct measurement of the shape of the Earth. To a good approximation this is possible when utilizing radar altimeters mounted on board orbiting space craft. Such an instrument determines the height of the satellite above the instantaneous ocean surface. After combination with accurate orbital tracking of the satellite motion the height of the ocean surface relative to the Earth's ellipsoid is determined. Technically the instantaneous sea surface height departs from the geoid by up to approximately 1 meter in the deep sea due to oceanographic effects such as tides and currents. Since the geoid signal is much larger than this, up to 100 meters, these oceanographic influences can be termed noise. Thus satellite altimeters determine the height of the marine geoid in the presence of oceanographic noise. For most geophysical purposes this is a suitable approximation.

In April, 1975 an Earth orbiting satellite was launched by NASA. It was called GEOS-3, and its mission dedicated to the mapping of the shape of the ocean surface. This satellite has provided a wealth of new information about the Earth, specifically more than 20 million kilometers of measurements of the marine geoid. In order to use this information to study the interior of the Earth there are basic questions to be answered. Does this instrument really determine the marine geoid, and how well does it function? To partially answer this question it is possible to calculate the marine geoid from ship gravity data and make comparisons with the satellite altimeter data. This is accomplished in chapters 1 and 2. Given measurements of the geoid, what are the techniques necessary to interpret the data and make inferences about

2

internal densities which cause the anomalies? In chapter 3 such methods of interpretation are developed. What are the basic results of satellite altimetry, what types of geoid anomalies have been detected? A basic survey of the various types of geoid anomalies is presented in chapter 4. In utilizing geoid data to study the Earth, it is best applied in combination with marine gravity data. But in utilizing gravity measurements at sea, what corrections are necessary because they were made on the undulating geoid? The need for geoid corrections in marine gravity is demonstrated in chapter 5. Lastly the question is asked, what new information about the Earth has been learned from the GEOS-3 satellite. In the final chapter a study of geoid anomalies over deep sea trenches demonstrates the power of marine geodesy and marine gravity in studying the interior of the Earth.

In order to determine how well the GEOS-3 radar altimeter maps the geoid, it is possible to make comparisons with an independently determined geoid. In the first chapter this procedure is described for the region of the Indian ocean. To calculate the geoid height, a technique using differences in gravity and geoid values is utilized. Initially average values of free air gravity are obtained for 1° x 1° squares in the region. Then values of gravity calculated from the GEM-6 gravitational field model are subtracted from the average values to obtain difference gravity data. Integration of this difference gravity using Stokes' formula results in the calculation of the difference geoid; this is added to the GEM-6 theoretical geoid heights to obtain the total Indian Ocean 1° x 1° gravimetric geoid. This regional geoid has features such as the Indian Ocean low of -130 m as well as a regional high in the Southwest Indian Ocean.

Utilizing the Indian Ocean geoid as well as gravimetric geoids from the North Atlantic and Northwest Pacific Ocean extensive comparisons have

been made with GEOS-3 radar altimeter estimates of geoid height, this is
described in chapter 2. A most obvious conclusion from such comparisons
is the constant offsets between the two data sets. These errors may be
due to scale errors in the reference ellipsoids, lack of atmospheric
corrections for the gravimetric geoid, errors in calculation of the
orbit in the radial direction, or altimeter bias errors. Another observation
is that altimeter data collected with the intensive mode instrument is less
noisy than global mode measurements. Even after elimination of long wavelength
errors, there are still discrepancies between the two data sets. In some
cases this is due to the averaging procedure of the gravimetric geoid con-
struction. It appears though that after correcting for errors in orbital
determination and other long wavelength errors, the satellite radar altimeter
can be utilized for a global mapping of the marine geoid, with resolutions
greater than are easily achieved with gravimetric geoids.

   After establishing the validity of the radar altimeter measurements,
it is necessary to develop new techniques to interpret marine geoid data.
This is accomplished in chapter 3. To demonstrate various properties, ideal
bodies of constant density are first utilized to calculate the geoid anomaly.
While such an approach has a certain initial utility, more realistic direct
methods require the computation of the geoid anomaly due to arbitrary two
and three dimensional bodies. In developing the formula for a two dimensional
polygon, the surface integral expression for geoid height is changed to a
line integral formula via Stokes' theorem and then integrated. For a three
dimensional polyhedron the volume integral expression for geoid height is
first converted to a surface integral by using the divergence theorem and
then to a line integral with Stokes' theorem. To better understand the
geoid anomaly, the relationship in the wavenumber domain between gravity and

4

geoid is developed. This indicates that the geoid has the same phase spectrum as the gravity anomaly but the amplitude spectrum is amplified at long wavelengths.

A basic need in the study of marine geodesy is to characterize the types of geoid anomalies which occur over geological structures. Such results in satellite altimetry are illustrated in chapter 4. Over continental margins the geoid increases by a 5 or 6 meter step at the shelf break. At deep sea trenches there is a 10 to 20 meter low which is 100 to 200 kilometers in width. Over the Bismarck sea region there is a 7 meter high geoid anomaly 500 km in width. At the Southwest Indian ridge there is a broad geoid high at least 500 to 700 km wide and 6 meters in amplitude. Above the Caroline Islands the ocean surface has a 5 meter positive anomaly, while at the Romanche fracture zone the geoid has a 5 meter step similar in shape to the bathymetry.

When measurements of gravity are made at sea they obviously are made on the geoid. However due to undulations of the geoid the free air gravity anomaly is not directly proportional to the gravitational attraction of the mass anomalies. If however a correction is first made for the varying distance from the center of the Earth and for the gravitational effect of mass between the geoid and ellipsoid, then the gravitational attraction of the mass anomalies is obtained. This geoid correction becomes necessary when studying the medium and long wavelength gravitational anomalies associated with the densities inside the mantle. This process for correcting the free air anomaly is discussed in chapter 5.

Finally in the last chapter geoid anomalies over deep sea trenches are discussed. Over all active subduction regions in the Pacific and Indian Ocean the geoid has a characteristic shape, thousands of kilometers in width.

5

Over the Aleutian Trench beginning about 2000 kilometers seaward of the trench axis, the geoid has a constant increase in height as the axis is approached. This slope is approximately a 20 meter rise over a distance of 1800 kilometers. Over the trench itself there is an approximate 13 meter decrease to form a 150 kilometer wide minimum. Immediately landward of the axis there is an 18 meter increase until a maximum is reached over the island arc. Behind the arc the geoid height gradually decreases by about 10 meters over a 1000 kilometer interval. In the vicinity of all major deep-sea trenches certain features form the characteristic geoid anomaly; a gradual long increase as the trench is approached from the ocean basin, a narrow low over the trench axis and a geoid high but with variable slope landward of the trench.

For the Tonga-Kermadec region a modeling study was undertaken to determine the density structure necessary to produce calculated values similar to the observed geoid and gravity anomaly. From this work several conclusions are possible. Shallower depths landward of the trench represent a mass excess which must be mostly compensated. Compensation must occur by the presence of a mass deficit somewhere in the underlying mantle. In our model a thinner uppermost mantle body provides the compensating mechanism. This separation of the mass excess and the underlying mass deficit is the primary cause of the char..cteristic geoid anomaly. Presence of the descending lithosphere is only of secondary importance in explaining the geoid anomaly. For the Kermadec Trench the density contrast of the slab with the surrounding mantle is approximately .02 gm/cm^3. Further studies are necessary for the other trench regions to determine if similar principles can be used to model the characteristic geoid anomaly.

Chapter I

Detailed 1° x 1° Gravimetric Ocean Geoid

and

Comparison with GEOS-3 Radar Altimeter Geoid Profiles

Introduction

A comprehensive set of data on the variation of the sea surface height has been obtained in the past three years by means of the GEOS-3 satellite carrying a radar altimeter. With knowledge of the satellite's position and after corrections for oceanographic effects, one obtains along-track variations of the geoidal height over the world's oceans. These measured undulations of the geoid are extremely valuable for geophysical interpretations because they provide, in part, information about density inhomogeneities in the earth's upper mantle. The distribution of the density inhomogeneities reflected in the geoid will hopefully provide information on convection within the mantle or on other possible driving forces of the earth's lithospheric plates.

Consequently, it is of special interest to determine and study the geoid on a worldwide scale. In the past, the only way to compute the geoid over oceanic areas was to apply Stokes' integral to the gravity anomalies observed over the earth's surface. Gravimetric geoids over oceanic areas have been computed in this way in the western North Atlantic (TALWANI, POPPE and RABINOWITZ, 1972), in the Indian Ocean (KAHLE and TALWANI, 1973) and in the Northwest Pacific (WATTS and LEEDS, 1977).

The knowledge of the geoid derived from surface gravity is essential in order to calibrate the radar altimeter, test its performance and possibly suggest optimum locations at which the altimeter measurements should be performed. Eventually, it will be desirable to compute a gravimetric geoid independent of satellite altimetry in order to obtain the dynamic sea surface height, the slight discrepancy between the geoid and sea surface being important in ocean dynamics.

8

In turn, there are techniques to recover gravity anomalies from GEOS-3 measurements of the sea surface height (e.g. KAHN, SIREY, BROWN and AGRAWAL, 1976). The method for obtaining gravity anomalies on the basis of satellite radar altimetry can be very useful for determining the gravity field in remote areas such as in the southern hemisphere where ship measurements are scarce. In order to test this method and define its accuracy it is necessary to compare the results with independently obtained gravity values from surface ship gravity measurements in surveyed regions.

It is the purpose of this paper to compile a new set of 1° x 1° mean free-air gravity anomalies in the Indian Ocean by using all the gravity data available up to 1976, compute the corresponding gravimetric geoid and compare the results with GEOS-3 altimeter derived geoid profiles (in the Southwest and Northeast Indian Ocean).

Sea Gravity Data in the Indian Ocean

Fig. 1 shows the location of the submarine pendulum observations (VENING MEINESZ, 1948; GIRDLER and HARRISON, 1957; TALWANI, 1962) as well as the ship's tracks along which continuous gravity measurements were obtained.

At present, there are about 100,000 gravity data available in the Indian Ocean.

The data used in this study were obtained by

a) Lamont-Doherty Geological Observatory of Columbia University during VEMA cruises 18, 19, 20, 22, 24, 29 and 33 and during CONRAD cruises 8, 9, 11, 12, 14 and 17.
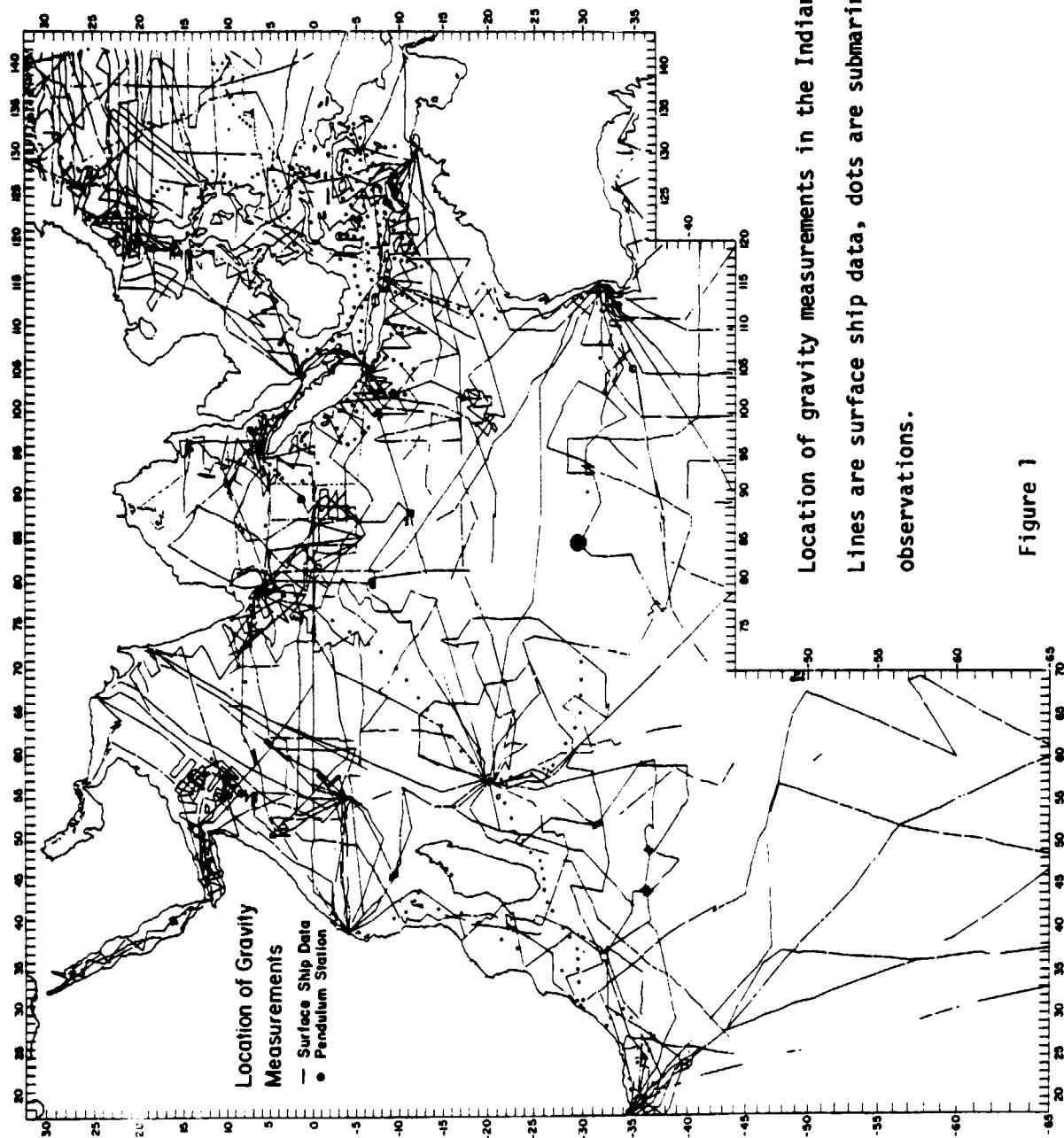
Location of gravity measurements in the Indian Ocean.
Lines are surface ship data, dots are submarine pendulum observations.

Figure 1

Location of Gravity Measurements
— Surface Ship Data
• Pendulum Station

b) Institute of Geophysics and Planetary Physics of the University
   of California at Los Angeles and Scripps Institution of Oceanography,
   San Diego, during ARGO cruises "Monsoon" and "Lusiad" (HELFER,
   CAPUTO and HARRISON, 1963; CAPUTO, MASADA, HELFER and HAGER,
   1964).

c) Department of Geodesy and Geophysics, Cambridge University,
   during OWEN cruises 611 through 619, 621 through 626, 110, 111
   and during DISCOVERY cruises 671 and 672 (HYDROGRAPHIC DEPARTMENT,
   1963, 1966; WILLIAMS, 1968).

d) ESSA (now NOAA) during PIONEER and OCEANOGRAPHER Cruises (U.S.
   DEPARTMENT OF COMMERCE, 1969, 1970).

e) Bundesanstalt für Bodenforschung, Hannover, West Germany, during
   METEOR cruise (PLAUMANN, 1965, personal communication).

f) Woods Hole Oceanographic Institution, U.S.A., during CHAIN
   cruise 100 (BOWIN, 1973, and BOWIN, personal communication).

The data obtained prior to 1971 are included in the gravity maps
(TALWANI and KAHLE, 1975) of the International Indian Ocean Expedition
(IIOE) Atlas of Geology and Geophysics (UDINTSEV, 1975) as well as in
the previous Indian Ocean geoid paper (KAHLE and TALWANI, 1973). During
recent Lamont cruises (1974, 1977) a considerable amount of data of
greater accuracy have been accumulated which made it desirable to recompile
the entire set of 1° x 1° mean gravity data. The main areas of substantial
improvements in the surface gravity field of the Indian Ocean are the
Central Indian Basin including the prominent Indian Ocean gravity low as
well as the South-West Indian Ocean covering the pronounced South-West
Indian Ocean gravity high. In the West Pacific we incorporated 1° x 1°

mean free-air anomalies compiled by WATTS and LEEDS (1977). For the Indian peninsul. we used a set of $1^\circ \times 1^\circ$ anomalies by WOOLARD (1970) and values for Madagascar were provided by the International Gravity Bureau, Paris (CORON, 1972, personal communication).

The new set of $1^\circ \times 1^\circ$ free-air anomalies for the Indian Ocean is listed in Table 1. The gravity values are referred tc the International Reference Ellipsoid (f = 1/297).

The $1^\circ \times 1^\circ$ averages were obtained from revised free-air anomaly contour maps by dividing each $1^\circ \times 1^\circ$ square into nine smaller squares. The values at the centers of these smaller squares were visually inter-polated and averaged to give a value for the $1^\circ \times 1^\circ$ square. In areas such as the southwest Indian Ocean the $1^\circ \times 1^\circ$ values were determined by averaging individual measurements.

Method of Geoid Computation

The following method - proposed and used by many authors including STRANGE, VINCENT, BERRY and MARSH (1972) and TALWANI, POPPE, and RABINOWITZ (1972) - has been adopted in computing the gravimetric geoid for the Indian Ocean:

1) Calculation of the free-air anomalies based primarily on the satellite derived gravity field, in this case the GEM-6 potential field model which includes harmonics up to n = 16 (LERCH et al., 1974; SMITH et al., 1976).

2) Subtraction of the GEM-6 free-air anomalies from the new set of $1^\circ \times 1^\circ$ mean gravity data (: Difference anomalies $\delta\Delta g$).

3) Computation of the difference geoid ΔN (Fig. 2) by applying Stokes' integral to the difference anomalies $\delta\Delta g$.

4) Summation of the GEM-6 geoid N_{GEM-6} (Fig. 3) and the difference geoid ΔN (: Gravimetric geoid $N = N_{GEM-6} + \Delta N$) (Fig. 4).

12
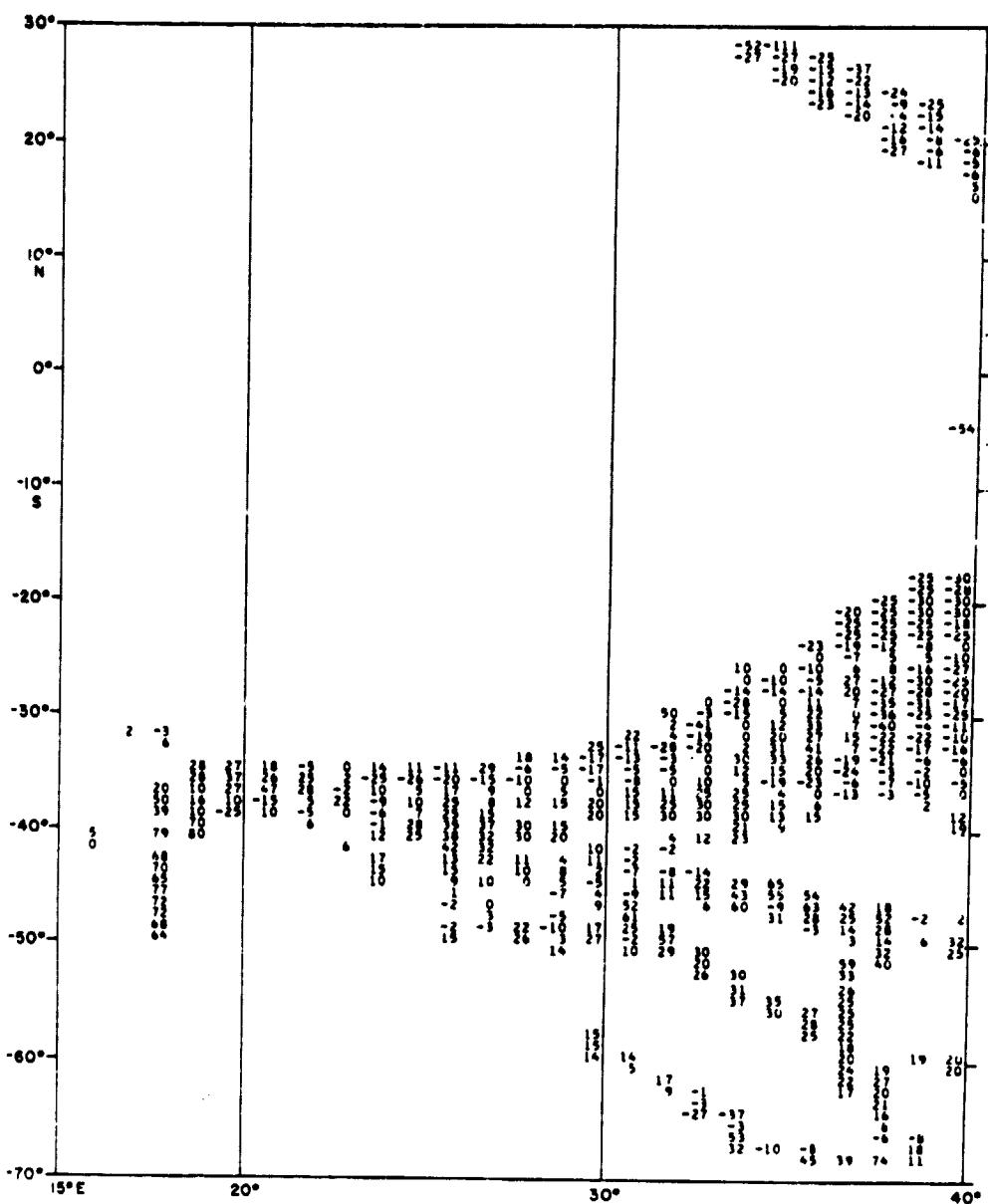
Table 1a

TABLE I

$1° \times 1°$ averages of free-air gravity, referred to the International Ellipsoid.
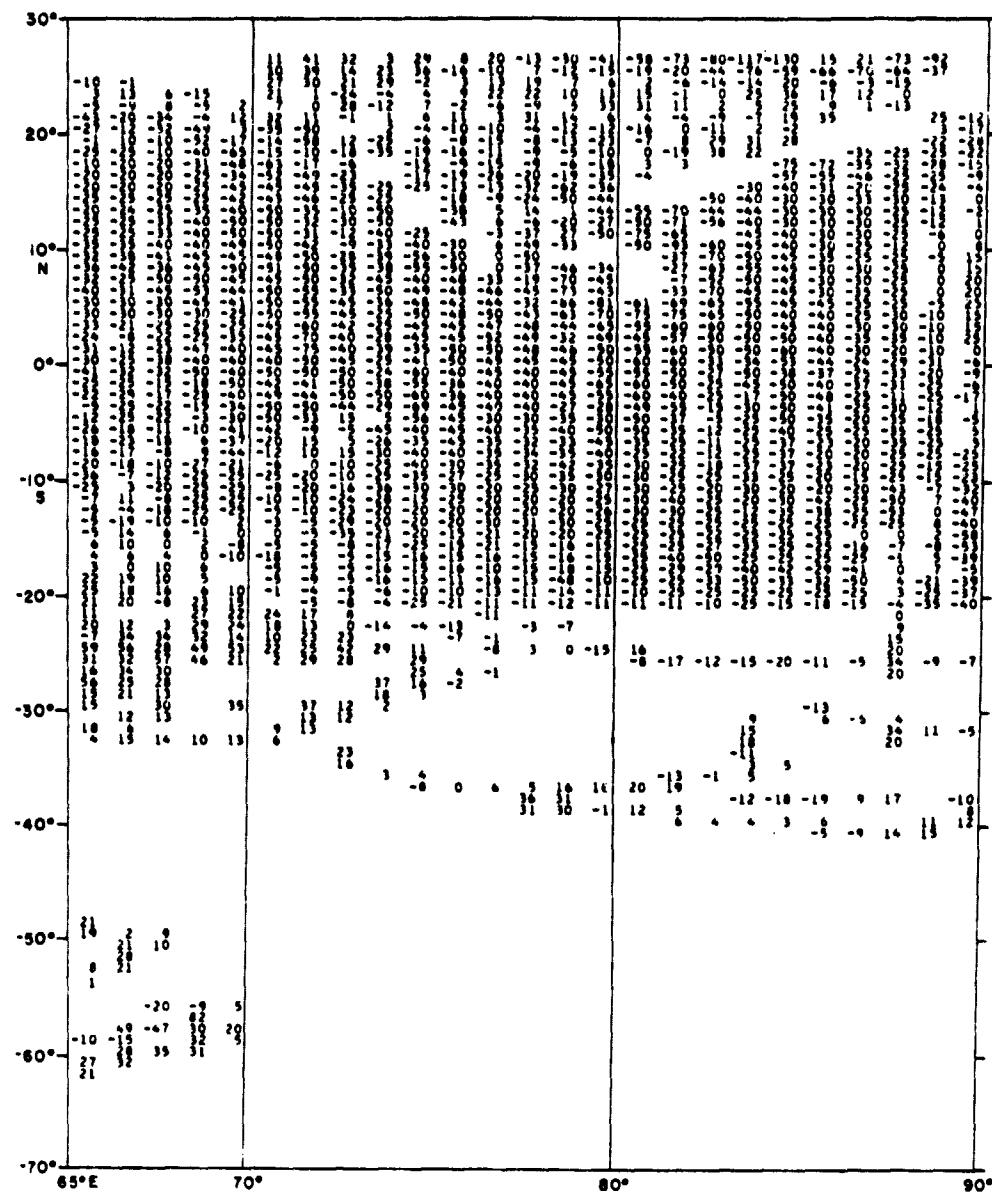
13

Table 1b

Table 1c

Table 1d
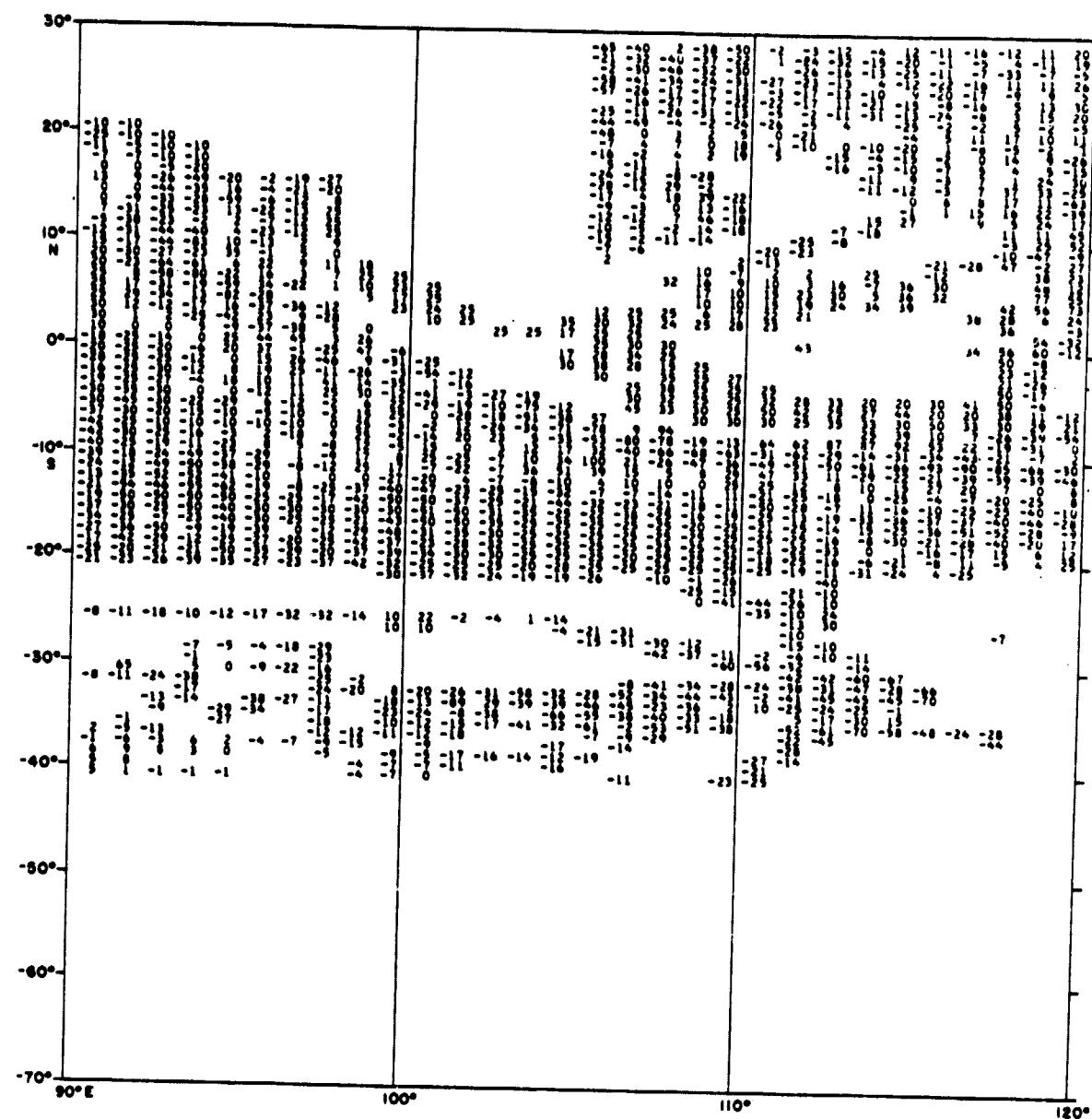
Table 1e

17

DIFFERENCE 1°x1° GEOID

(2 METER CONTOUR INTERVAL)
RELATIVE TO GEM-6

Figure 2

18

GEM-6 GEOID
(10 METER CONTOUR INTERVAL)

REFERRED TO INTERNATIONAL
ELLIPSOID f=1/297

Figure 3

19

GRAVIMETRIC
1°x1° GEOID

(5 METER CONTOUR INTERVAL)

REFERRED TO INTERNATIONAL
ELLIPSOID f⁻¹=²⁹⁷⁄₂₉₇

Figure 4

20
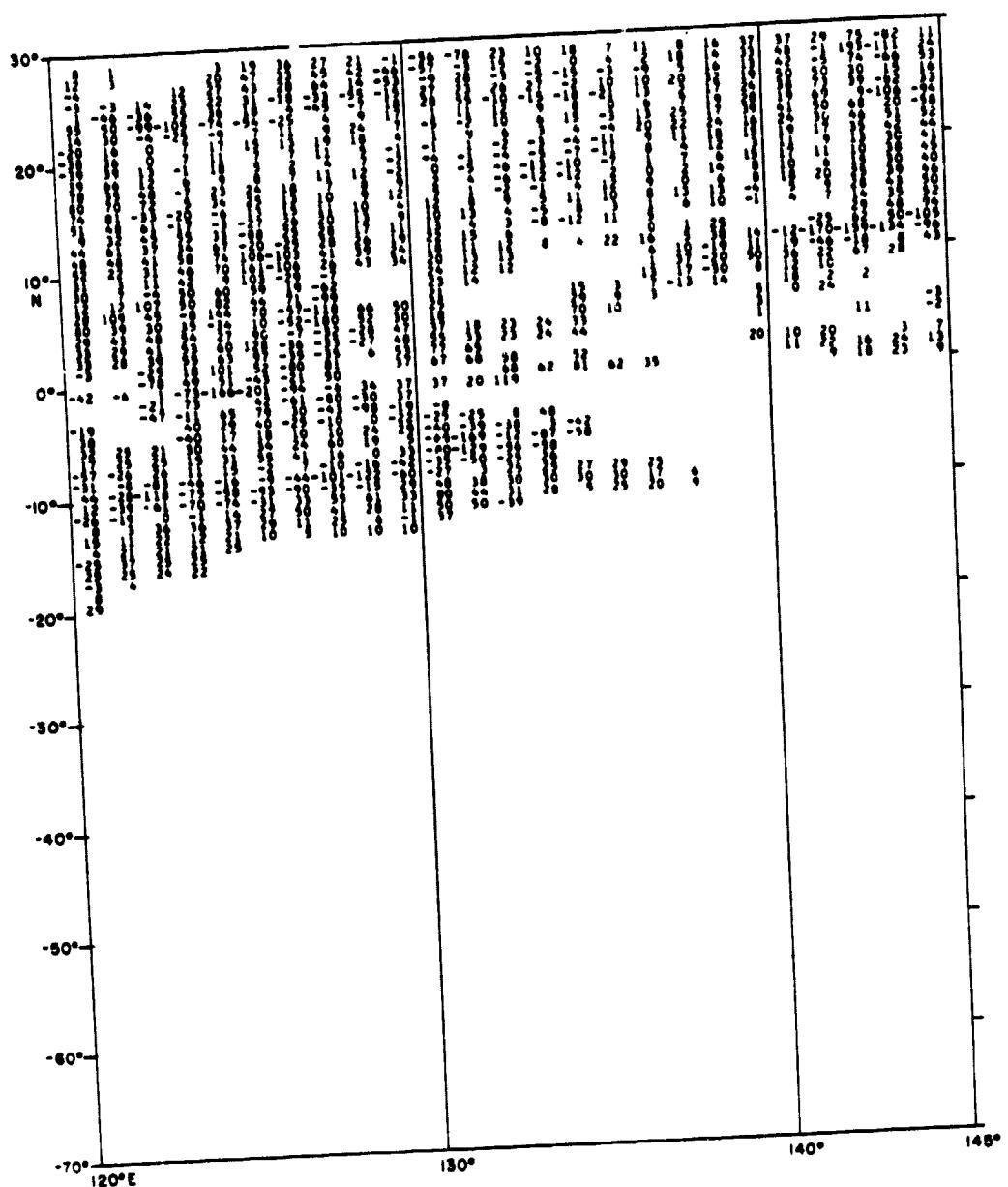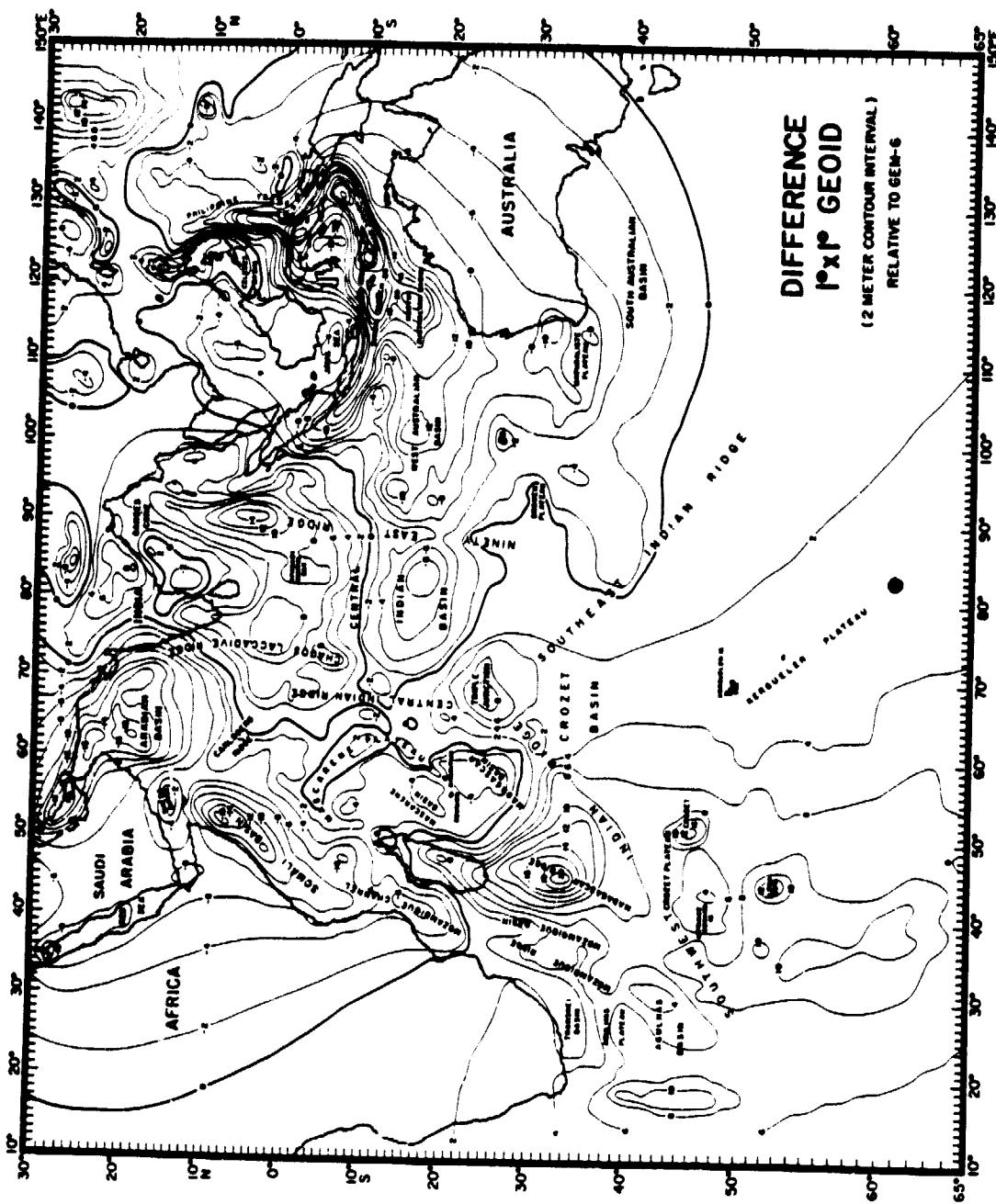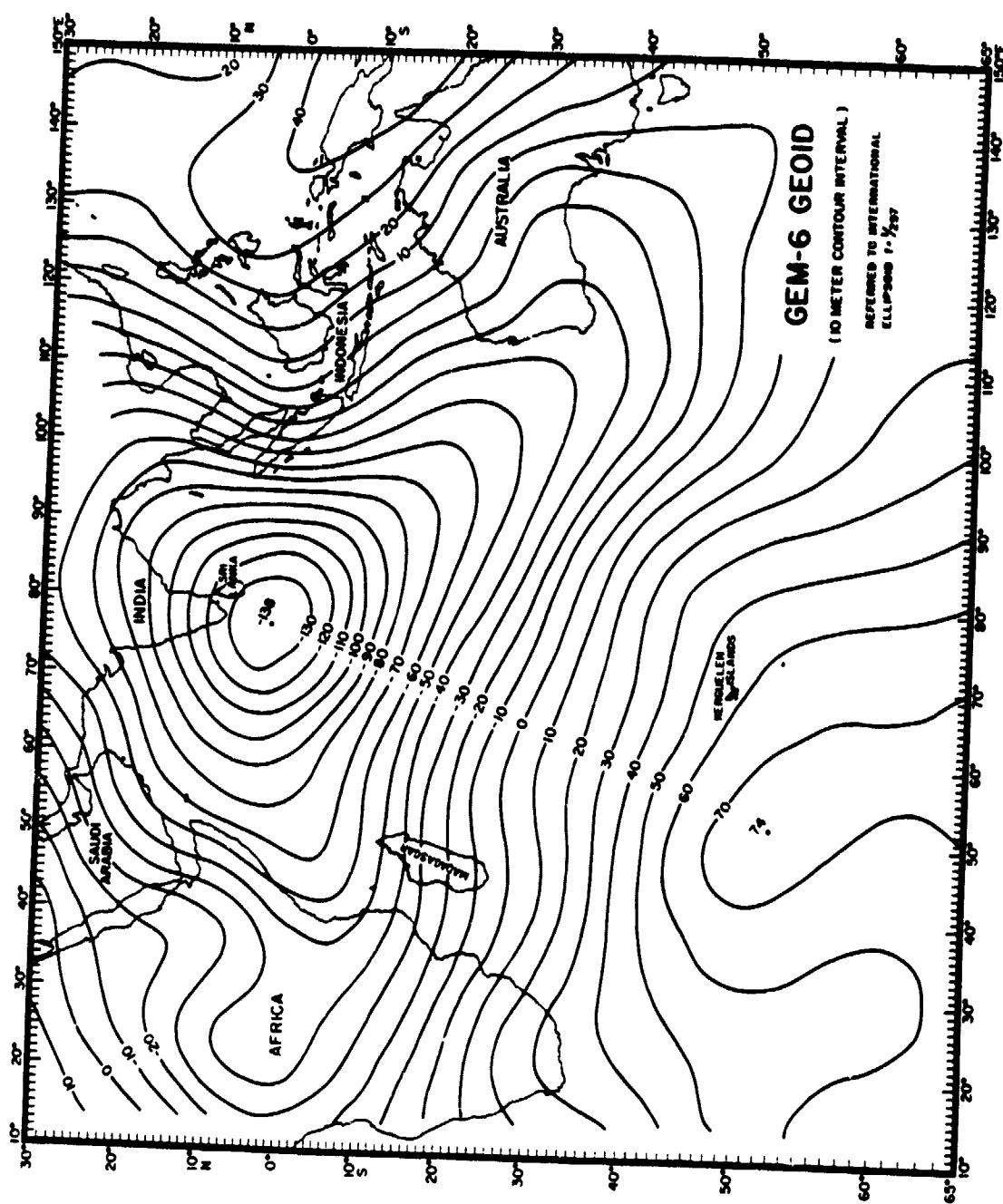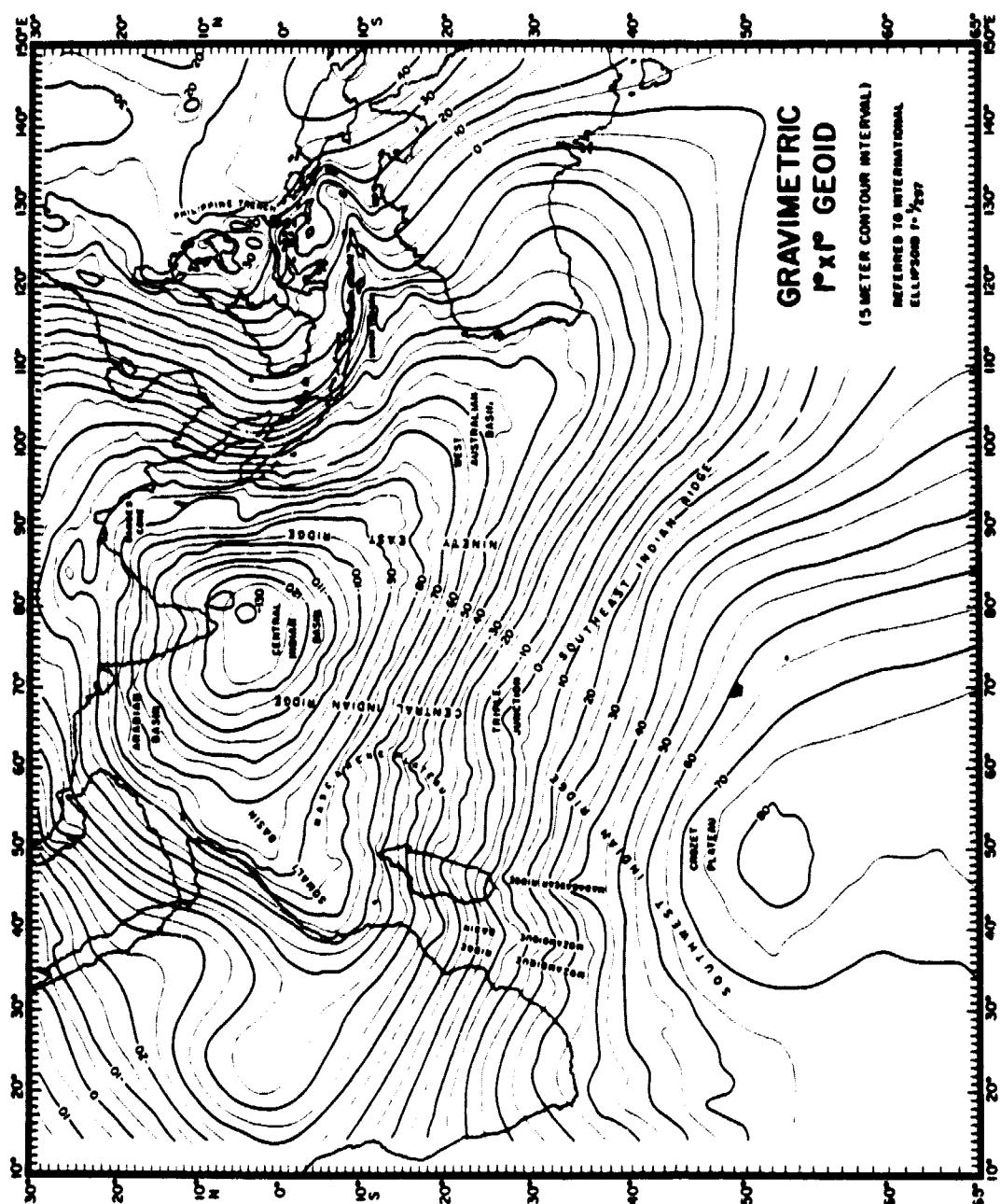
The advantage of this procedure is that Stokes' integration (HEISKANEN and MORITZ, 1967)

$$\Delta N = \frac{1}{4\pi gR} \int S(\psi) \, \delta\Delta g \, da \qquad (1)$$

has to be carried out only over the Indian Ocean because outside this area the difference anomalies $\delta\Delta g$ are assumed to be zero.

We recognize that we are ignoring the difference anomalies outside the Indian Ocean, which will give rise to some errors particularly near the boundaries of our area of integration. These errors however are less than 1 meter (STRANGE et al., 1972). In parts of the Indian Ocean, where gravity averages could not be obtained by the procedure described above - because of scarcity of data - we assumed the difference anomaly $\delta\Delta g$ to be zero. As we shall see in a later section, this gives rise to errors in regions of no ship gravity measurements. This procedure is still superior to methods in which gravity values are truncated after a certain radius.

In Equation (1) ΔN = Difference geoid, R = mean earth's radius, g = mean earth's gravity, ψ = angular distance between the element of area da (at which $\delta\Delta g$ is given) and the point of calculation, $S(\psi)$ = Stokes' function. Stokes' function $S(\psi)$ is defined as

$$S(\psi) = \frac{2}{\sin\psi} \, F(\psi) \qquad (2)$$

where $F(\psi) = \cos\frac{1}{2}\psi + \frac{1}{2}\sin\psi(1-5\cos\psi - 6\sin\frac{1}{2}\psi - 3\cos\psi\ln(\sin\frac{1}{2}\psi + \sin^2\frac{1}{2}\psi))$

Since $S(\psi)$ changes strongly near $\psi=0°$ the effect of a square very close to the computation point cannot be calculated by simply using $S(\psi)$ with ψ being the distance to the center of the square. For this reason the squares close to the computation points were subdivided into smaller squares in such a way that the percentage error in calculating $S(\psi)$ is below 1% (TALWANI et al., 1972).

The GEM-6 Geoid, Difference Geoid and 1° x 1° Gravimetric Geoid

In subtracting the GEM-6 free-air anomalies (n=16) from the 1° x 1° surface data and applying Stokes' integral to the difference anomalies, a difference geoid is obtained which reflects mainly the contributions of harmonics $16 < n < 180$. The order n=180 corresponds to a wavelength of 2 degrees which is approximately represented by the 1° x 1° mean free-air anomalies. As such, the difference geoid containing wavelengths between about 220 km and 2500 km, can be interpreted as a filtered version of the total geoid. This range is of special interest for geophysicists because mass inhomogeneities associated with sea-floor spreading and lithospheric motions may produce geoid anomalies of such wavelengths. Fig. 2 shows the computed difference geoid.

The areal average of the difference gravity anomalies $\delta\Delta g$ is -.54 mgal and that of the difference geoid ΔN is -.47m. Thus, the systematic error in geoid height corresponding to this difference is negligible and may not be considered further. The general pattern of the difference geoid can be characterized by the zero meter contour line, indicated by the heavy line on Fig. 2. The entire Northwest Indian

Ocean including the major basins such as the Somali and Arabian Basins are associated with a negative difference geoid reaching -19 m over the Arabian Basin. Another large area with negative difference geoidal undulation is the Northeast Indian Ocean covering the southern Central Indian Basin, the West Australian Basin and the Indonesian deep sea trench with lowest values over the Sunda Trench (-22 m) and Timor Trough (-30 m).

The northern Central Indian Basin, the major part of the Bay of Bengal (Ganges Cone) and the entire Southwest Indian Ocean is characterized by a pronounced difference geoid high with highest values over the Madagascar Ridge (+20 m). While the major actively spreading   es are not well expressed in the difference geoid, the triple junction of the three Indian Ocean ridge branches at 25°S, 70°E clearly stands ou'   a positive feature (+8 m). Also aseismic ridges including the Madagascar Ridge, the Mascarene Plateau, the Ninetyeast Ridge (+14 m) and the Afanasy Nikitin Seamount chain are associated with a positive difference geoid.

The total 1° x 1° geoid obtained by adding the difference geoid to the GEM-6 geoid (Fig. 3) is shown in Fig. 4. While the difference geoid

reflects wavelengths between 220 and 2500 km, the total geoid reveals information with all wavelengths greater than 220 km. As might be expected, the long wavelength features are still present in the total geoid. The prominent Indian Ocean geoid low (-130 m) as well as the geoid highs in the Southwest Indian Ocean and over the western Pacific are clearly expressed in the 1° x 1° total gravimetric geoid. In addition the short and intermediate wavelength features such as the Mozambique Ridge and Basin, the Madagascar Ridge and Mascarene Plateau, the Triple Junction, the Ninetyeast Ridge and the Sunda Trench are evident by the bending of contours around those structures. The minimum south of India has shifted towards the northeast and has decreased in amplitude by 8 m. The Somali Basin low appears to connect with the Arabian Basin low.

GEOS-3 Profiles in the Indian Ocean

Classically the geoid height has been determined by the Stokes' integration of gravity values, as demonstrated in the previous section. The altimeter in the GEOS-3 satellite now makes it possible to directly measure the elevation of the satellite over the ocean surface. When combined with precise orbital tracking one obtains the height of the ocean surface relative to an earth ellipsoid. The sea surface is not at a constant gravitational potential; nongravitational forces can cause slight deviations between the geoid and sea surface. Dynamic topography due to ocean currents can be 100 cm in amplitude (DEFANT, 1941), tidal heights in the deep ocean can also be 50 cm in amplitude (SCHWIDERSKI, 1977). After correction for such deviations, measurements of the geoid height may be obtained along the sub satellite track.

24

While this procedure for obtaining geoid heights from altimeter measurements is valid, it is subject to certain errors. An extensive error analysis has been made for GEOS-3 measurements in the calibration area between Florida and Bermuda (Martin and Butler, 1977). This showed an average noise level of .72 m in the intensive mode and 1.81 m in the global mode for cumulative altitudes every .1 seconds. Additionally, bias values of -5.3 m (intensive mode) and -3.55 m (global mode) were discovered for altitude determinations by the altimeter. Accuracy of the sea surface height measurements is primarily limited by the orbit computations. Long wavelength errors in orbital height can be between 1-2 m rms and 10 m rms depending upon the method of tracking (H.R. Stanley, personal communication). A consistent set of altimeter data can be constructed by analyzing measurement differences where two satellite tracks cross. By least square reduction of such crossover errors Rummel and Rapp (1977) were able to effectively eliminate any long wavelength orbital discrepancy. In this paper we are primarily interested in comparing original GEOS-3 data (from NASA Wallops Flight Center) with a gravimetric geoid in the Indian Ocean to see the influence of such errors. The orbit numbers and dates for the satellite tracks are listed in Table 2.

Operation of the altimeter is conceptually simple. A radar pulse is transmitted downward and the return pulse is received after reflection from the sea surface. As there is a finite beam width, the instrument measures the sea surface height over a limited area, with a 14.3 km radius for global mode and 3.6 km radius for intensive mode. Operation of the altimeter is in one of two modes; global mode or intensive mode during which measurements are made every .01024 seconds. This is a sampling rate of approximately every 65.5 meters. During data processing the sea surface height measurements are averaged over a finite time.

25

Table 2

ORBITS AND DATES FOR SATELLITE TRACKS

Track Designation	Orbit Number	Day	Year	Altimeter Mode	Orbital Accuracy
G0141	1194	184	1975	Global	A
G0154	1237	187	1975	Intensive	A
G0192	1647	216	1975	Intensive	J
G0193	1653	216	1975	Global	D
G0195	1667	217	1975	Intensive	D
G0212	2061	245	1975	Intensive	D
G0219	2104	248	1975	Intensive	D
G0223	2189	254	1975	Intensive	D
G0224	2190	254	1975	Intensive	D

A 10^{+}m rms

D   3 - 10m rms

J   3m rms

This is a low pass filtering operation. In this paper we only use time averaged data usually over a 2.048 second interval. Consequently the resultant datum is an average measurement of the sea surface height over an area of 14.3 by 13.4 km (global mode) or 3.6 by 13.4 km (intensive mode). Knowledge of the beam footprint and the altimeter accuracy is necessary in understanding the utility and ultimate resolution of GEOS-3 measurements.

The geoid measurements made by the radar altimeter are shown in Figure 5 and 6. The sub satellite track is plotted on a Mercator projection, the geoid height is plotted perpendicular to the track with positive values on the north side. An arbitrary constant offset has been subtracted from each profile because we are interested only in the relative changes of the geoid. Figure 5 is the Indonesian Island arc region and Figure 6 is the Southwest Indian Ocean.

Three GEOS-3 tracks, all approximately perpendicular to the Java Trench, are illustrated in Figure 5. Each profile shows a steep long wavelength increase in the geoid height of 90 m over a distance of approximately 2400 km, with highest values towards the northeast. Not being symmetric about the trench axis, the geoid continues to increase across the trench until leveling off in the Philippine Sea (Fig. 4). Directly over the Java Trench the profiles indicate a geoid low of -10 m amplitude and 250 km wavelength. Analogous with the gravity low over deep sea trenches (WATTS and TALWANI, 1974), this geoid low is primarily caused by the bottom topography.

While the principal features of the Northeast Indian Ocean are deep sea trenches and an island arc, the Southwest Indian Ocean is the location
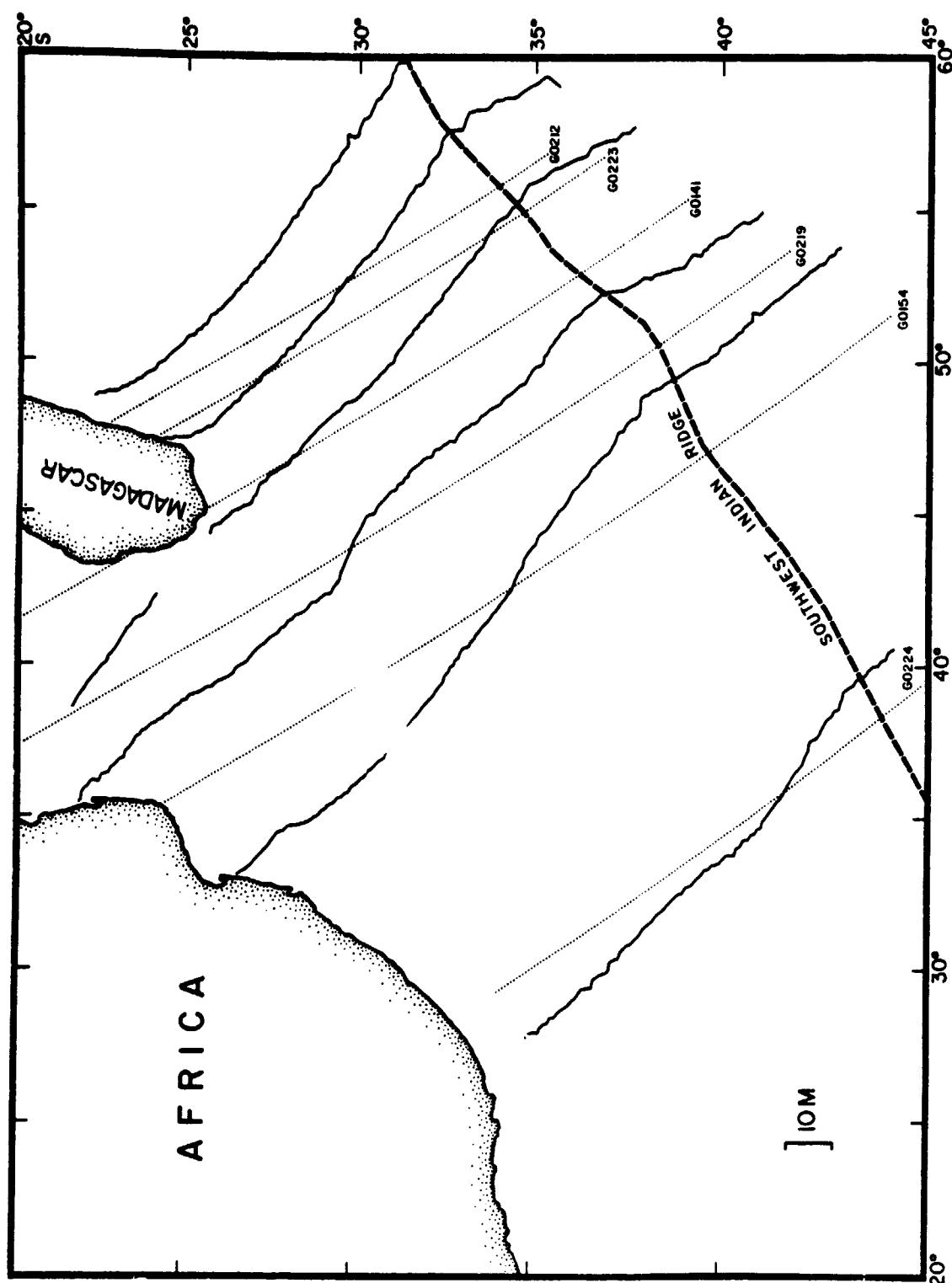
Figure 6

GEOS-3 profiles in the Southwest Indian Ocean. Sub satellite track is
dotted line, track designation (e.g. GO154) is at start of pass. Geoid
height is plotted perpendicular to track, positive values are northwards
and the scale is indicated. An arbitrary constant was removed from each
track.   28
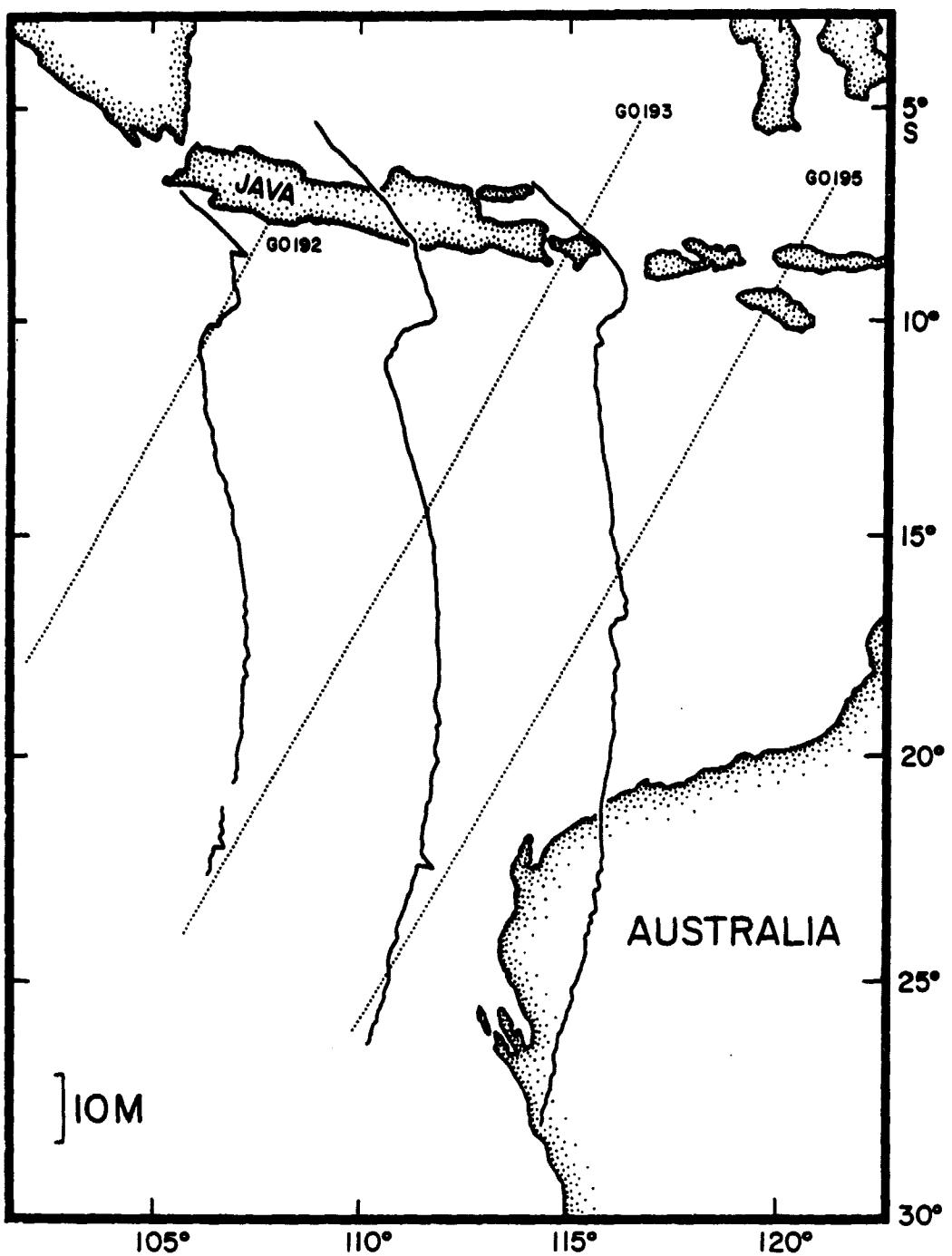
Figure 5

GEOS-3 profiles in the Indonesian Island Arc region. Sub satellite
track is dotted line, track designation (e.g. GO193) is at start of the
pass. Geoid height is plotted perpendicular to track, positive values
are northwards and the scale is indicated. An arbitrary constant was
removed from each track.

of a seismically active spreading center - the Southwest Indian Ridge. Topographically high, it is associated with a 6 m positive geoid anomaly, 500 km wide (Figure 6 and 7, especially tracks G0219 and G0224). Additionally a longer wavelength geoid gradient exists, increasing towards the southeast and leveling off at the ridge axis (Figure 4 and 6).

Comparison of gravimetric geoid with GEOS-3 altimeter measurements

Being a new scientific instrument, the accuracy and precision of the GEOS-3 altimeter must be determined. Obviously a useful test would be the comparison of the gravimetric Indian Ocean geoid with geoid heights measured directly by the GEOS-3 radar altimeter. In making the comparison characteristics of each method must be understood. The gravimetric geoid contains information from the GEM-6 gravity model up to n = 16, the higher harmonics (to n = 180) being dependent upon the accuracy and availability of ship gravity data. Resolution of features with wavelengths less than about 200 km cannot be expected in the gravimetric geoid due to our averaging procedure over 1° x 1° squares. With the GEOS-3 altimeter sea surface features with wavelengths of 1.31 km can technically be resolved (with average values every 655 m), however with the averaged data we utilized resolution is limited to 28 km. Also inaccurate orbit determinations result in constant and very long wavelength errors in the altimeter measurements. Consequently we only make comparisons of geoid information with wavelengths shorter than several thousand km.

GEOS-3 measurements of geoid height are referred to an ellipsoid with flattening f = 1/298.255 and semi-major axis a = 6378145 m, thus the gravimetric geoid was converted to this ellipsoid prior to comparison. Linear interpolation of the gravimetric geoid with the nearest three

geoid values was used in order to compute the gravimetric geoid height
along the sub satellite track. Results of this comparison are in Figure
7, each track location is plotted in Figure 5 or 6 and the track designation
(e.g. GO195) is at the start of the pass (time = 0 seconds).

Obviously the radar altimeter cannot measure the geoid over land,
thus such measurements have been deleted (e.g. Madagascar). GEOS-3
measurements in Figure 7 are indicated by the thin line and the gravimetric
geoid by the thick line. An obvious feature of this comparison is the
offset values of up to 25 m, probably due to error in orbit determination.
These profiles indicate a great similarity (except for a constant shift)
between GEOS-3 data and the gravimetric geoid wherever good gravimetric
control exists (see e.g. GO242). In some areas (south of 39°S in SW
Indian Ocean) only few sea gravity measurements exist. Consequently, in
this area the gravimetric geoid contains little information for wavelengths
shorter than n = 16 (2500 km). This is seen in tracks GO224 and GO219
between 0 and 120 seconds over the Southwest Indian Ridge. The GEOS-3
data indicate a clear anomaly over the ridge while the gravimetric geoid
does not. As there is poor gravity control in this area and the anomaly
is seen on both tracks, we conclude the gravimetric geoid is incorrect
along this part of profiles GO224 and GO219, whereas GEOS-3 measures the
true geoid anomaly over the Southwest Indian Ridge.

In finer detail, the GEOS-3 altimeter has greater resolution than
the 1° X 1° gravimetric geoid (of this paper), due to a smaller sampling
interval for the altimeter. Over the Java Trench (tracks GO195, GO193
in Figure 7) the effect of the averaging procedure for the calculation
of the gravimetric geoid is clear: GEOS-3 data indicate a 250 km wide
low, 10 m deep. The gravimetric geoid barely defines the low. Due to
the information content in wavelengths shorter than about 200 km, it is
understandable that the GEOS-3 altimeter with a smaller sampling interval
would measure the geoid more accurately in this region.

# COMPARISON OF GRAVIMETRIC GEOID WITH GEOS-3 ALTIMETER MEASUREMENTS

Figure 7

32
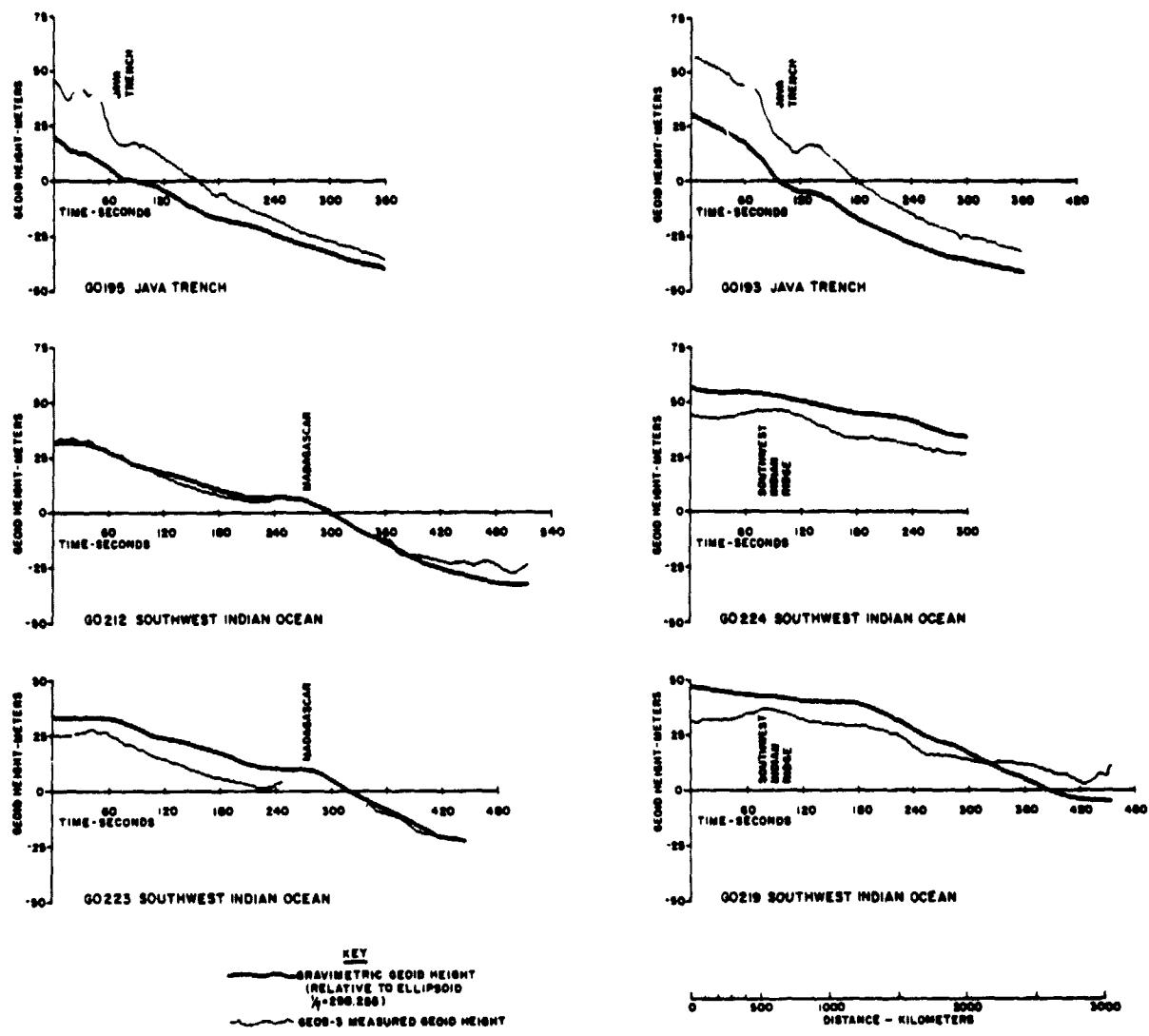
Conclusions

On the basis of marine gravity measurements in the past three decades, we have compiled and listed in Table 1 1° x 1° mean free-air gravity anomalies for the Indian Ocean. These values are useful in geoid computations and as a test for techniques of gravity recovery from GEOS-3 geoid measurements. Utilizing these 1° x 1° averages we have computed a difference and total gravimetric geoid for the region.

The difference gravimetric geoid contains information with wavelengths between about 200 km and 2500 km, such wavelengths being determined by lateral density inhomogeneities within the crust and upper mantle. Anomalies of -18 m in the difference geoid exist over the Arabian Basin, another large area with negative values is the Northeast Indian Ocean with lowest values over Sunda Trench (-22 m) and Timor Trough (-30 m). Over the Madagascar Ridge there is a 20 m difference geoid high, another positive feature is the triple junction of the three Indian Ocean ridges, +8 m amplitude. Aseismic ridges such as Madagascar Ridge, Ninetyeast Ridge and Afanasy Nikitin seamount chain are also associated with a positive difference geoid.

The total gravimetric geoid contains information on all wavelengths down to about 200 km; thus it has both long and intermediate wavelength features. Over the Central Indian basin is the most prominent long wavelength feature, the -130 m Indian Ocean geoid low. Steep geoidal gradients exist over the Indonesian Island Arc up to a flat region of the geoid in the Phillipine Sea. Another level portion of the geoid exists south of the Crozet Plateau. Intermediate wavelength anomalies in the total geoid are over the same features as in the difference geoid.

33

GEOS-3 profiles of geoid height show anomalies across topographic features in the Indian Ocean. Over the Southwest Indian Ridge there is a 6 m positive geoid anomaly, 500 km wide. Across the Java Trench there is a steep increase in the geoid of 90 m over a distance of 2400 km, with highest values towards the northeast. Directly over the Java Trench there is a -10 m geoid low, 250 km wide. If this relative low is removed, an overall geoid high remains. This is an interesting result because it might shed some light on the density inhomogeneities associated with the descending Indian lithospheric plate. In part, this pronounced geoid high - verified in the GEOS-3 profiles - can be explained by the positive density contrast of the cold lithosphere with respect to the less dense adjacent asthenosphere. On the basis of gravity data Watts and Talwani (1974) concluded this effect is not the only component because unrealistically high density values would have to be postulated to explain both the "outer gravity high" and the overall high. It is further interesting to note that in our GEOS-3 profiles an "isolated" outer geoid high does not exist. The increase in geoid height seaward of the Indonesian Trench appears to be a portion of the overall long-wavelength high - only interrupted by the relative small-wavelength low over the trench proper. Another possible source for part of this long-wavelength geoid high may be associated with the downwarped isotherms caused by the cold sinking lithosphere. If the temperature is lowered at the Olivine-Spinel transition zone (at depths between 300 and 400 km) this phase change migrates upwards, thus providing a positive density contrast of about 0.2 gm/cm^3 (BOTT, 1971; RINGWOOD, 1976). To explain this long wavelength geoid anomaly at the Java Trench, a detailed modeling study should be undertaken; only then will the cause of this anomaly be better defined.

34

Comparisons of GEOS-3 data with the gravimetric geoid show a great similarity where good gravimetric control exists. Due to the shorter sampling interval (14 km versus about 100 km averaging for the gravimetric geoid) for the altimeter the GEOS-3 satellite can better detect short wavelength features such as the low over the Java Trench. On the basis of these comparisons we conclude the GEOS-3 altimeter is an accurate and highly useful instrument for mapping the geoid at sea.

CHAPTER I ACKNOWLEDGEMENTS:

REFERENCES

Bott, M.H.P., 1971. The mantle transition zone as a possible source of global gravity anomalies, Earth and Planetary Science Letters, 11, 28.

Bowin, C., 1973. Origin of the Ninety-East Ridge from studies near the equator, J. Geophys. Res., 78, 6029.

Caputo, M., Masada, R., Helfer, M.D., and Hager, C.L., 1964. Gravity measurements in the Atlantic, Pacific and Indian Oceans, May 1962 - August 1963, R/V ARGO. Interim Report, Univ. of Calif, Inst. of Geophysics and Planetary Physics.

Defant, A., 1941. Quantitative Untersuchungen zur Statik und Dynamik des Atlantischen Ozeans, Die relative Topographie einzelner Druckflächen in Atlantischen Ozean, Deutsche Atlantische Exped. Meteor, 1925-1927, Wiss. Erg., VI, 183.

Girdler, R.W. and Harrison, J.C., 1957. Submarine gravity measurements in the Atlantic Ocean, Indian Ocean, Red Sea and Mediterranean Sea. Proc. Roy. Soc., A 239, 202.

Heiskanen, W.A. and Moritz, H., 1967. Physical Geodesy, W.H. Freeman and Co., San Francisco, Calif.

Helfer, M.D., Caputo, M. and Harrison, J.C., 1963. Gravity measurements in the Pacific and Indian Oceans, MONSOON Expedition 1960-1961. Interim Rept., Univ. of Calif., Inst. of Geophysics and Planetary Physics.

Hydrographic Department, Admiralty, 1963, 1966: Bathymetric, magnetic and gravity investigations H.M.S. OWEN 1961-1962, 1962-1963, Admiralty Marine Sci. Publ., no. 4, parts 1, 2; no. 9, parts 1, 2.

Kahle, H.G. and Talwani, M. 1973. Gravimetric Indian Ocean Geoid. Z. für Geophysik, 39, 167 and 491.

Kahn, W.D., Sirey, J.W., Brown, R.D. and Agrawal, B.B., 1976. Gravity
anomaly determination by means of GEOS-3 altimetry data. (Abstract
only) EOS, 57, 901.

Lerch, F., Wagner, C.A., Richardson, F.A., Brown, F.E., 1974. Goddard
Earth Models 5 and 6 Rep. X-921-74-145, Goddard Space Flight Center,
Greenbelt, Md.

Martin, C.F. and Butler, M.L., 1977. Calibration results for the
GEOS-3 altimeter, NASA Contractor Report CR-141430.

Ringwood, A.E., 1976. hase transformations in decending plates and
implications for mantle dynamics, Tectonophysics, 32, 129.

Rummel, R. and Rapp, R., 1977. Undulation and anomaly estimation
using GEOS-3 altimeter data without precise satellite orbits, Bull.
Geod., 51, 73.

Schwiderski, E.W., 1977. Ocean tides and GEOS-3, Trans., A.G.U., 58,
370 (Abstract only).

Smith, D.E., Lerch, F.J., Marsh, J.G., Wagner, C.A., Kolenkiewicz, R.,
and Kahn, M.A., 1976. Contributions to the National Geodetic
Satellite Program by Goddard Space Flight Center, J. Geophys.
Res., 81, 1006.

Strange, W.E., Vincent, S.F., Berry, R.H. and Marsh, J.G., 1972. Detailed
gravimetric geoid for the United States, In: The Use of Artificial
Satellites for Geodesy, S. Henriksen, A. Mancini, and B. Chovitz
(eds.), Washington, D.C., 169.

Talwani, M., 1962. Gravity measurements on H.M.S. ACHERON in South
Atlantic and Indian Oceans, Geological Society of America Bull.,
73, 1171.

Talwani, M., Poppe, H. and Rabinowitz, P., 1972. Gravimetrically
determined geoid in the western North Atlantic. In: Sea surface
topography from space, NOAA Tech. Rept. ERL-228 - AO ML 7-2, 34p.

Talwani, M. and Kahle, H.-G., 1975. Maps of free-air gravity anomalies
in the Indian Ocean, In: The International Indian Ocean Expedition
Geological - Geophysical Atlas of the Indian Ocean, G. Udintsev
(ed.), Moscow, 87.

Udintsev, G. (ed.), 1975. The International Indian Ocean Expedition
Geological - Geophysical Atlas of the Indian Ocean, Moscow.

U.S. Department of Commerce, Environmental Science Services Administration,
1969. International Indian Ocean Expedition USC & GS Ship PIONEER,
1964, v. 1 & 3. Washington.

U.S. Department of Commerce, Environmental Science Services Administration,
1970. Technical Report ERL 152-OD 4. Global Expedition USC & GS
Ship OCEANOGRAPHER - 1967 Cruise Narrative and Scientific Program.
Boulder.

Vening Meinesz, F.A., 1948. Gravity expedition at sea 1923-1938, v.IV,
Publ. Neth. Geod. Commission, Delft.

Watts, A. B. and Talwani, M., 1974. Gravity anomalies seaward of deep-
sea trenches and their tectonic implications, Geophys. J. Roy.
Astr. Soc., 36, 57.

Watts, A.B. and Leeds, A., 1977. Gravimetric geoid in the Northwest
Pacific Ocean, Geophys. J. Roy. Astr. Soc., 50, 249.

Williams, C., 1968. R.R.S. DISCOVERY cruise 16 Indian Ocean 1967,
bathymetric, gravity and magnetic data report.

Woollard, G.P., 1970. 1° x 1° square free-air gravity averages in
India, Publ. Hawaii Inst. of Geophys.

Chapter II

Comparison of Gravimetric Geoids with GEOS-3 Altimetric Geoid

INTRODUCTION

With the aid of a radar altimeter mounted on board the GEOS-3 satellite it is now possible to rapidly determine the shape of the ocean surface. This information can be used to provide an estimate of the marine geoid. However, because the altimeter is a new instrument, it is of considerable interest to compare such measurements with other types of data. Thus we examine how well GEOS-3 estimates of geoid height compare with data from independently determined gravimetric geoids.

GRAVIMETRIC GEOIDS

On land the geoid may be constructed using astrogeodetic methods; or alternatively utilizing gravimetric methods and Stokes' integration of the measured values of gravity. At sea direct determination of deflection of the vertical is a difficult task, consequently only about 20 measurements have ever been made (Von Arx, 1966). Due to this difficulty, only with measurements of gravity at sea can geoid computations be performed. This technique for oceanic geoid construction was demonstrated in the western North Atlantic Ocean (Talwani, et al, 1972). Subsequent studies have involved construction of oceanic geoids in the Indian Ocean (Kahle and Talwani, 1973), Northwest Pacific (Watts and Leeds, 1977) and an updated Indian Ocean geoid (Kahle, Chapman and Talwani, 1978). Worldwide geoids have been constructed by Heiskanen (1957) and Marsh and Vincent (1974).

Basically our technique of geoid construction involved a series of computational steps:

1. Compilation of marine gravity data and averaging over a specified area - in this case 1° x 1° averages.

2. Calculation of free air anomalies on the basis of a certain gravitational potential model; our computations utilized the GEM-6 model (Smith et al., 1976).

3. Subtraction of the calculated free-air anomalies (GEM-6) from the areal averages of measured gravity; this is the set of difference gravity anomalies.

4. Application of Stokes' integral to these difference gravity values to obtain the difference geoid.

5. Addition of this difference geoid to the geoid of the gravitational potential model (GEM-6) to obtain the total gravimetric geoid.

Computationally this procedure is efficient because it eliminates the need for calculation of Stokes' integral over the entire earth. As the integration is done only over the area of study, this is equivalent to utilizing GEM-6 gravity values outside the area of computation. Some errors can be introduced, especially near the boundaries; however, such errors are less than 1 meter (Strange et al., 1972).

Due to this procedure there are several inherent characteristics of these gravimetric geoids. Outside a certain region the values of gravity due to a satellite model are utilized, consequently the long wavelength (roughly $N \leq 16$) components in these geoids are determined by that particular gravity model. In our case the long wavelength components of the gravimetric geoids are determined by the GEM-6 field. Another property of these geoids results from the initial procedure of

42

averaging gravity values over a finite region. Averaging over a certain

interval and subsequent decimation of data corresponds to a low pass

filter operation with a gradual cutoff band. In our gravimetric geoids

this procedure would eliminate most wavelengths shorter than 2° which is

twice the sampling period. At a latitude of 23° then one could state

that our 1° x 1° gravimetric geoids do not contain much information in

the wavelengths shorter than about 200 km. Another characteristic of

the present marine geoids is that in some regions where there are few

ship tracks there is difficulty in obtaining average gravity values. As

Stokes' function is most sensitive to adjacent locations, it would be

expected that in regions where gravity averages are poorly determined,

the geoid would likewise not be accurately calculated.

In constructing these geoids there were no corrections made for the

effect of mass of the atmosphere external to the geoid (Moritz, 1974).

In ignoring this problem, errors of several meters in geoid height are

possible (Rapp, 1975). Such errors would be manifest as very long

wavelength differences or constant offsets in geoid height.

Prior to our comparison study, the gravimetric geoids were first

transformed to be relative to a best fitting ellipsoid with flattening

1/298.255. During the transformation only the J_2 and J_4 terms were

altered; there was no change in the zero'th order undulation. Theore-

tically then the radius of this new reference ellipsoid corresponds to

the actual radius of the earth. GEOS-3 data is referred to an ellipsoid

with flattening 1/298.255 and radius 6378142 m. There is a possible

scale difference between the reference ellipsoids for gravimetric geoids

and altimetric geoids. They do, however, have identical values of

flattening.

43

For purposes of comparison in this study we utilize gravimetric geoids in the Indian Ocean (Kahle, Chapman and Talwani, 1978) as shown in Figure 1, Northwest Pacific (Watts and Leeds, 1977) in Figure 2, and North Atlantic (Talwani and Leeds, in preparation) in Figure 3.

GEOS-3 ALTIMETER

Several characteristics of the GEOS-3 radar altimeter have a bearing on our study. On board the satellite there are two transmitters, one designated the global mode and the other termed intensive mode. Both measure the height of the satellite above the sea surface every .01 seconds. In practice it has been found that the global mode results in a signal with higher noise; consequently this mode was little used after the initial stages of the mission (H.R. Stanley, personal communication). During computer processing of this data an average measurement is determined. For the low rate telemetry format this is a 2.048 second average and for the high rate telemetry format a 3.277 second average. At an average ground track speed of 6.55 km/sec this results in a measurement every 14.3 km (low rate) or 21.5 km (high rate). Due to this averaging procedure most wavelengths shorter than 28.6 km (low rate) or 43 km (high rate) will be eliminated from our GEOS-3 measurements.

After the radar altimeter measures the altitude of the spacecraft, orbit calculations are utilized to locate the satellite relative to the center of mass of the earth. During the orbit computation a satellite derived gravity field is used; any errors in the assumed geopotential coefficients will generate uncertainty in the radial position of the satellite. In a comparison study of the SKYLAB radar altimeter and

44

GRAVIMETRIC
1°x1° GEOID

(5 METER CONTOUR INTERVAL)

REFERRED TO INTERNATIONAL
ELLIPSOID f=½₂₉₇

Figure 1

TOTAL GEOID
Flattening 1/298·2
Contour Interval 2 meters

Figure 2

Figure 3

47
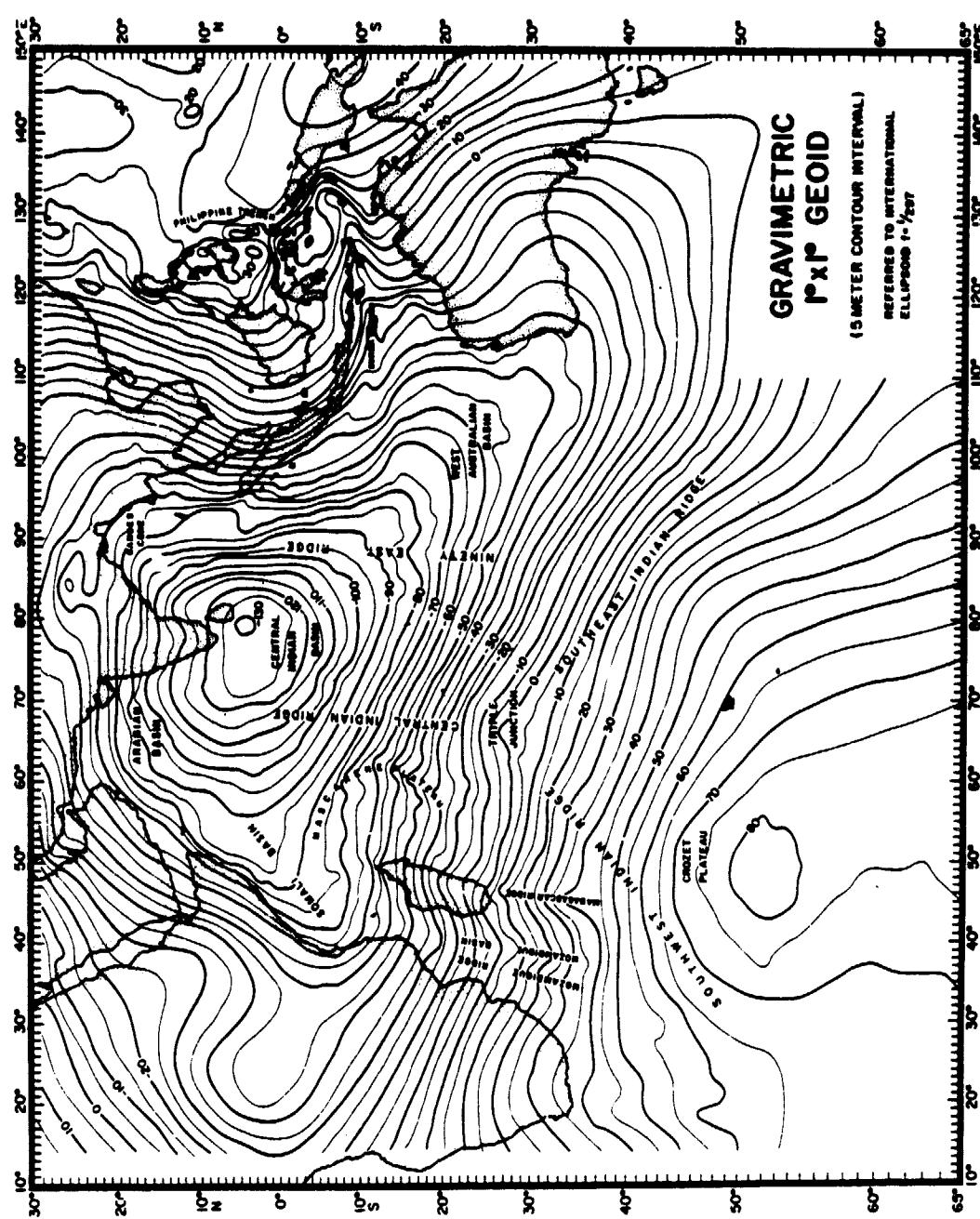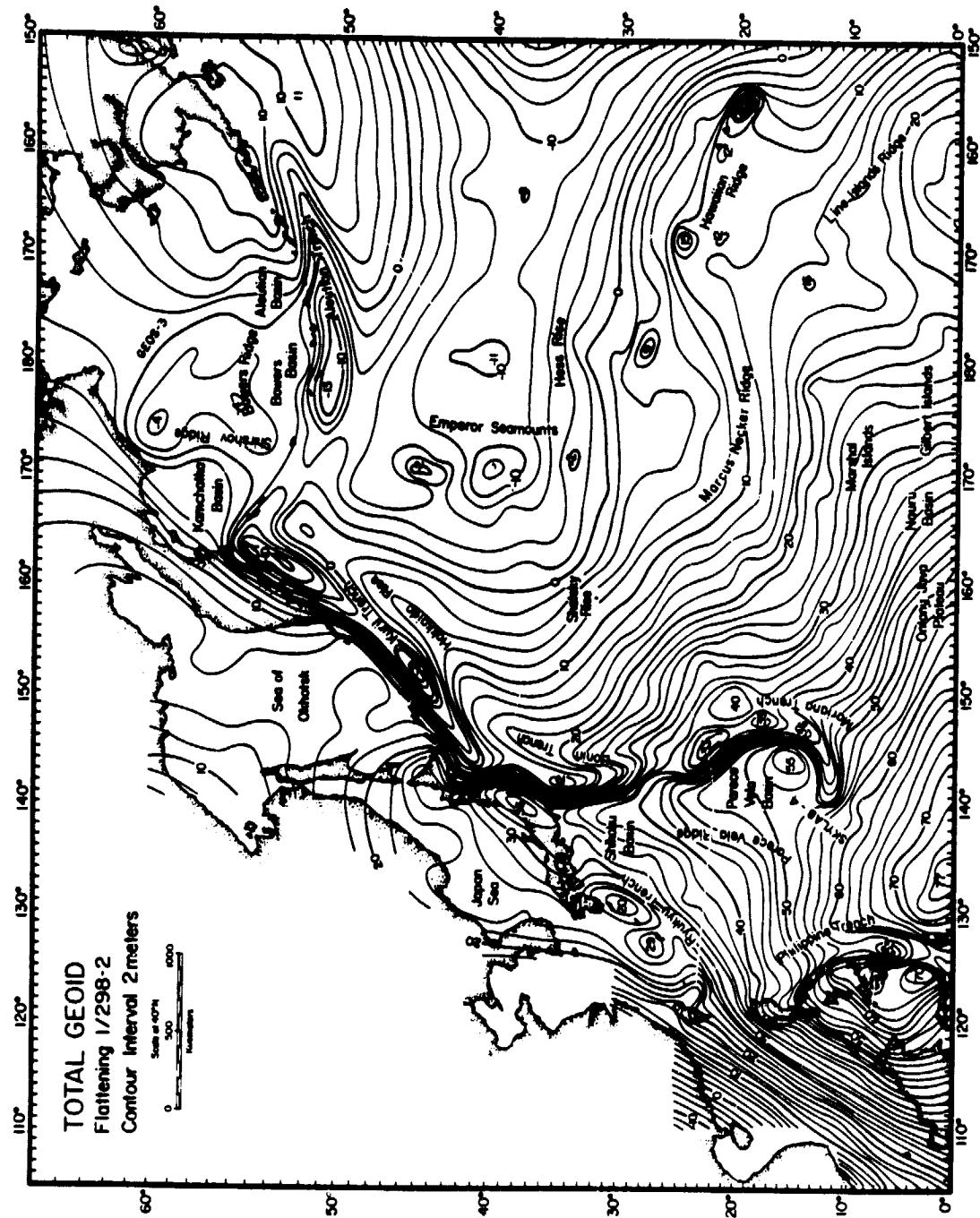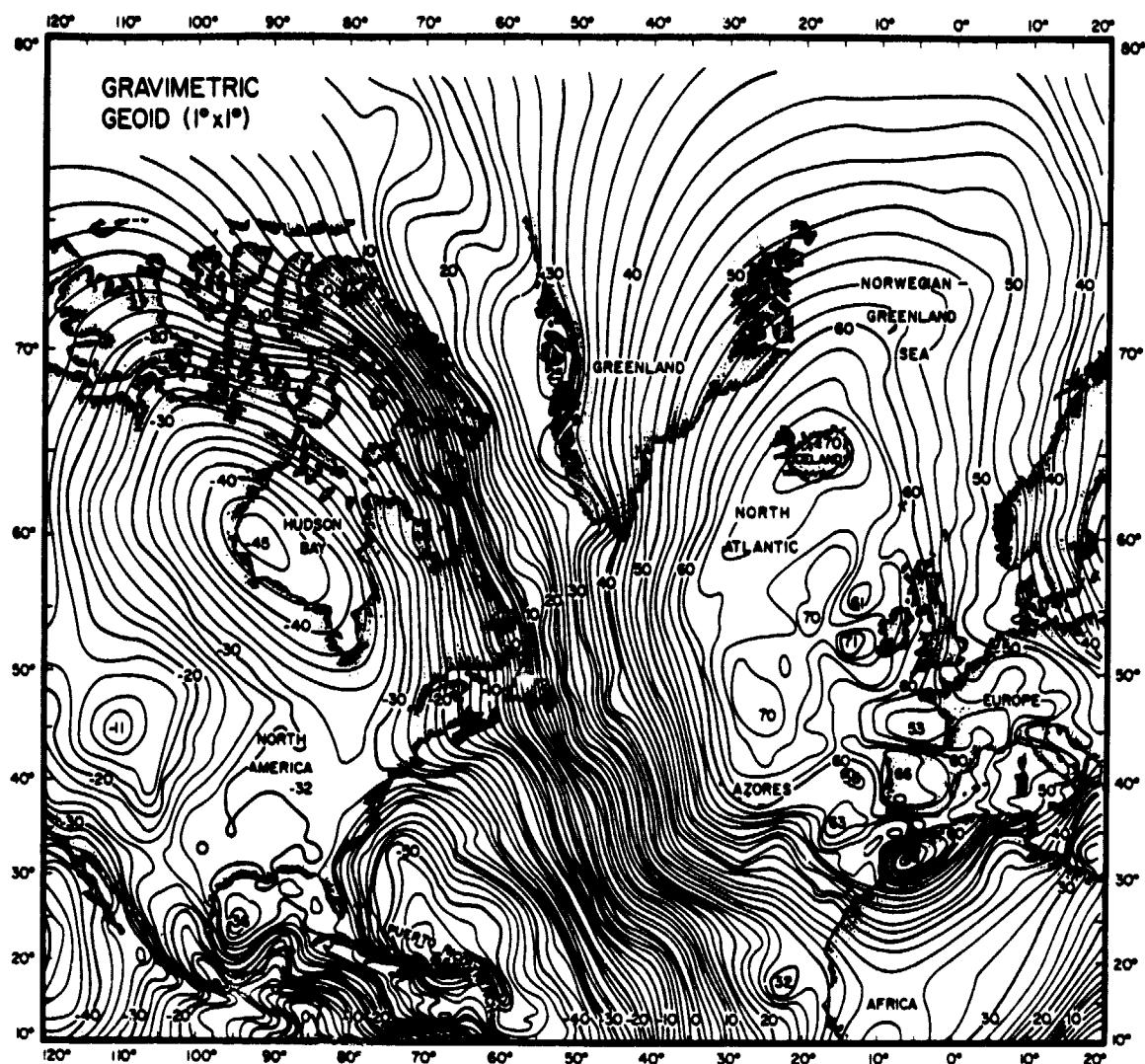
satellite geoids, an error analysis of orbital uncertainty was performed by Marsh et al. (1976). Due to possible errors in the quantity GM there was a mean radial uncertainty of 2.8 m in the SKYLAB orbit. Possible errors in geopotential coefficients and station coordinates generated radial orbit uncertainty of approximately ± 1 m about the mean value. This uncertainty in radial position of SKYLAB was slowly varying over a given orbit. Certainly for the GEOS-3 satellite an orbital error analysis would indicate different numerical values; however, similar inferences can still be made. Any errors in the quantity GM, coefficients of the geopotential, and station coordinates will all result in mean radial uncertainties and slowly varying errors in the radial position of GEOS-3. What causes additional confusion with this satellite (GEOS-3) is that several different gravitational field models were utilized for the orbit computations; for the data in this paper it was a GEM-8 (Wagner et al., 1976) or an NWL model. Another possible source of uncertainty is caused by any bias in altimeter range data. This is discussed in detail by Martin and Butler (1977).

After altitude measurement and orbit calculation, the sea surface height is determined. To obtain an estimate of geoid height, tidal corrections should be made. Our GEOS-3 data were corrected with the tide model of Hendershott (1973).

COMPARISON OF GRAVIMETRIC GEOIDS WITH GEOS-3 ALTIMETER

Using GEOS-3 altimeter estimates of geoid height, we have made comparisons with the gravimetric geoids presented in the previous section. The gravimetric geoids were interpolated at the point of altimeter measurement; interpolation was linear relative to the nearest

three gravimetric geoid values. A track chart of the location of altimeter measurements, and the extent of the gravimetric geoids is shown in Figure 4; a listing of orbit numbers for each track is in Table 1.

In Figure 5 there is a comparison of data with the Indian Ocean geoid, the altimeter data is plotted as a function of time of acquisition from the first data point. The first obvious fact from this comparison is that GEOS-3 data often differs from the gravimetric geoid by a constant level. RMS differences between the two sets of data are in the range 3.69 m to 13.27 m as listed in Table 2.

In analyzing the causes for this discrepancy there are a variety of possible causes. These include bias in altitude determination (Martin and Butler, 1977), radial orbital uncertainty, scale errors in the geoid, and long wavelength errors in either the gravimetric geoid or radial orbital position. To test for the effect of bias in altitude measurement, corrections for this error were made using the results of Martin and Butler (1977). After correction for the effects of bias utilizing the results of Martin and Butler, the rms differences were recomputed and results listed in Table 2. In general this bias correction often increases the discrepancies. This shows that our comparisons of the GEOS-3 values are mostly lower than the gravimetric geoid, and the bias correction enlarges this difference. Due to small uncertainties in the geopotential coefficients, value of GM, and tracking station coordinates, there may be uncertainty in the radial orbital position of GEOS-3. Such errors would be manifest as either constant or slowly varying radial uncertainty. This has been proven in a quantitative manner for the SKYLAB altimeter by Marsh et al. (1976). Any radial error in orbit determination can generate apparent constant

49
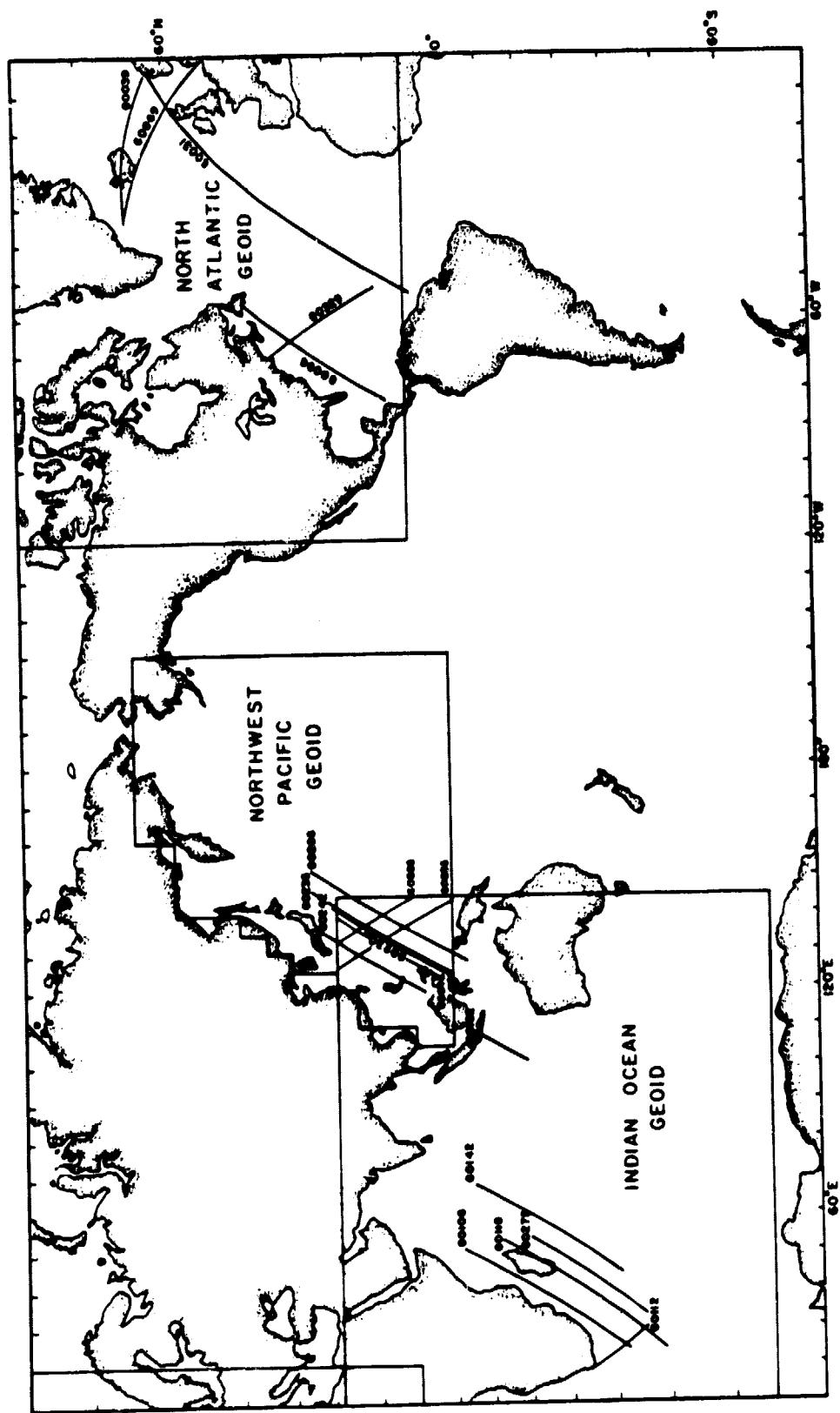
Location of GEOS-3 tracks utilized in this study. Track designations are the L-DGO numbers, orbit numbers for each track are listed in Table 1. Outlines of each region covered by each gravimetric geoid are also shown.

Figure 4

50

Table 1

| Track no.	Orbit	Telemetry mode	Transmitter mode
INDIAN OCEAN			
GO118	646	Low	Intensive
GO275	461	Low	Intensive
GO142	1200	Low	Global
GO182	1568	Low	Intensive
GO106	362	High	Intensive
GO112	584	Low	Intensive
NORTHWEST PACIFIC			
GO242	2037	Low	Intensive
GO230	1795	Low	Intensive
GO235	416	Low	Global
GO266	430	Low	Global
NORTH ATLANTIC			
GO329	3245	Low	Intensive
GO039	184	Low	Global
GO096	325	Low	Global
GO069	398	High	Intensive
GO031	210		
NORTHWEST PACIFIC			
GO846	1724	Low	Intensive
GO855	1616	Low	Intensive
GO565	2028	Low	Intensive
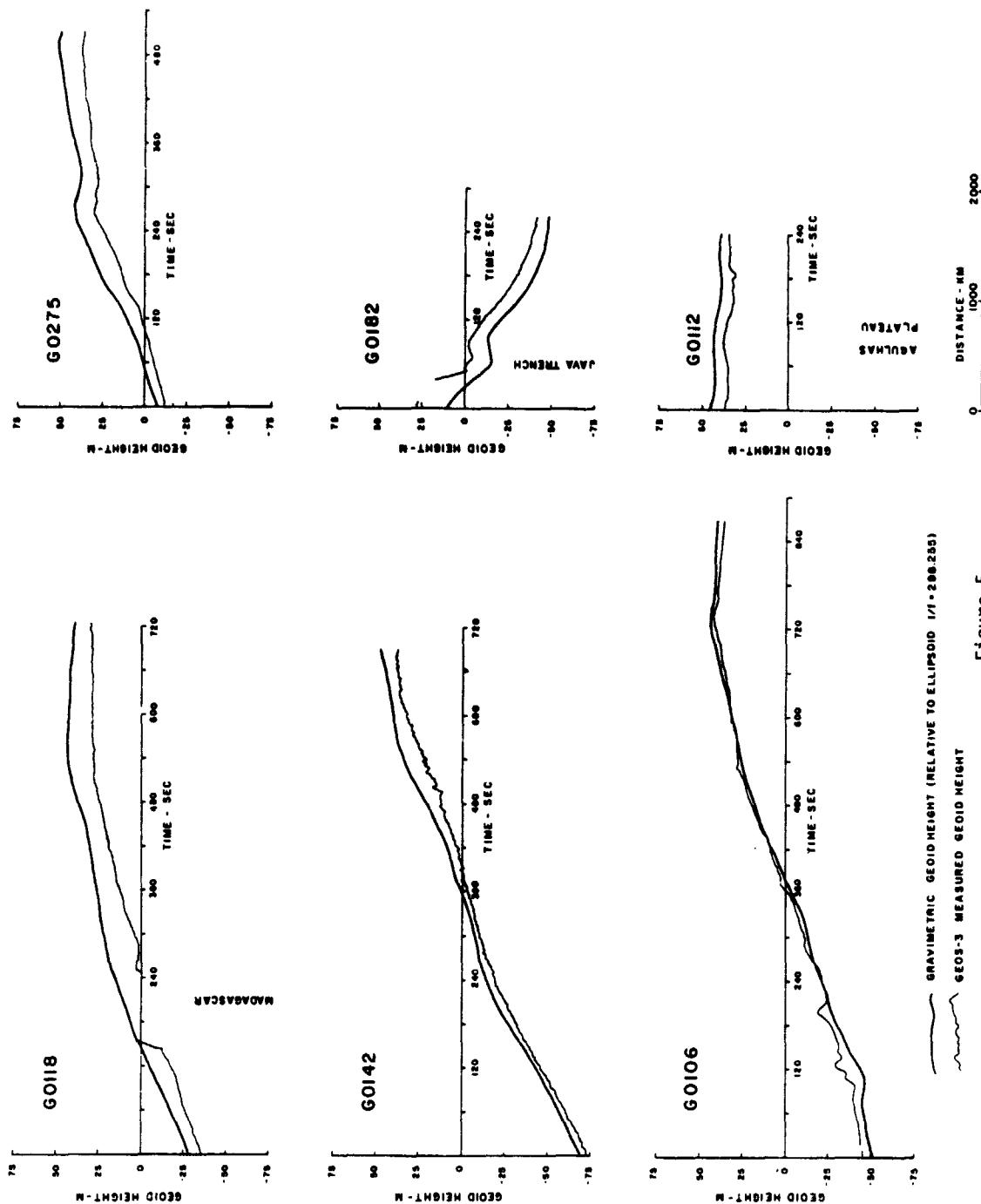
Comparison of Indian Ocean gravimetric geoid with GEOS-3
estimates of geoid height. Geoid height is plotted as a
function of time of acquisition from first point. The sub-

52

Table 2

RMS discrepancies between gravimetric geoids and GEOS-3 estimates of geoid

Track no.*	RMS difference	RMS difference after bias correction	A priori orbital error
		INDIAN OCEAN	
G0106	3.69 meters	4.78 meters	$10^{\pm}$ meters
G0112	6.99	12.26	$10^{\pm}$
G0118	13.27	18.37	$10^{\pm}$
G0142	6.67	10.01	$10^{\pm}$
G0275	10.84	16.02	$10^{\pm}$
G0182	11.15	6.46	3
		NORTHWEST PACIFIC	
G0242	17.87	15.87	3
G0230	18.00	23.61	3 ± 10
G0235	5.86	11.07	$10^{\pm}$
G0266	6.82	10.27	$10^{\pm}$
		NORTH ATLANTIC	
G0031	18.99		
G0039	23.93	37.23	$10^{\pm}$
G0069	13.18	15.65	$10^{\pm}$
G0096	13.18	15.65	3-10
G0329	3.07	8.05	3

*Orbit numbers listed in Table 1

offsets between the gravimetric and altimetric geoids. If the actual orbit error is slowly varying, then over the short segment during which altimeter data is acquired it may appear to have a constant offset or tilt which in reality is only one part of a mucn longer wavelength error in radial position of the satellite. A complicating factor with GEOS-3 is that several different sets of geopotential coefficients have been utilized for the orbit calculations. These gravity models are either GEM-8 (Wagner et al., 1976), GEM-10 (Lerch et al., 1977), or a NWL model. In properly utilizing GEOS-3 data it is mandatory that all orbits be calculated with only one geopotential model. This would provide a consistent data set.

During orbit calculations by NASA a priori estimates of rms orbital errors were made. These are listed in Table 2. For example, track GO106 has an a priori radial uncertainty of greater than 10 m rms while the rms discrepancy between the gravimetric and altimetric geoid is 4.78 m. In other cases the actual rms difference exceeds the prior estimates. Additionally constant offset discrepancies between the two data sets may occur due to scale errors in the gravimetric geoid or ellipsoid for GEOS-3 data and to the lack of atmospheric corrections with the gravimetric geoids. In this type of comparison study it is virtually impossible to isolate the cause of the observed constant offsets between GEOS-3 geoids and gravimetric geoids. They may be caused by any or all of the aforementioned sources of error. These large constant offsets do indicate the need for high quality orbital computations with a consistent gravity model, atmospheric corrections in gravimetric geoids, elimination of errors in reference ellipsoids, and analysis of internal consistency of the data.

By analyzing altimeter data at crossover locations and least square reduction of crossover errors, Rummel and Rapp (1977) were able to obtain rms crossover discrepancies of .78 m for intensive mode operation. Our comparisons indicate the need for this type of crossover analysis and error reduction.

Comparisons of the altimeter data and the Northwest Pacific gravimetric geoid are shown in Figure 6. In this the influence of the transmitter mode is evident. Tracks G0242 and G0230 are relatively smooth and were collected in the intensive mode, tracks G0235 and G0266 have high frequency noise and were made in the global mode. In general all of the figures show that the intensive mode has less high frequency noise than the global mode of acquisition.

Another aspect of our comparison study involves the question of what are the shortest wavelengths in the geoid and how well does the gravimetric geoid and altimeter data record such wavelengths. To understand the short wavelength (less than several hundred kilometers) components of the geoid, it is necessary to examine their origin. Any geoid anomaly is due to the anomalous potential caused by a mass heterogeneity. On the basis of potential theory it would be expected that short wavelength components of the geoid would be caused by the nearest mass anomalies; this would be topography of the ocean floor and moho which are large, adjacent, mass inhomogeneities. To see this mathematically consider the relationship between the Fourier transform of gravity and bathymetry, the admittance.

$$Z(k) \quad = \quad \mathcal{F}[g(k)] \, / \, \mathcal{F}[b(k)] \qquad\qquad (1)$$

55

Figure 6
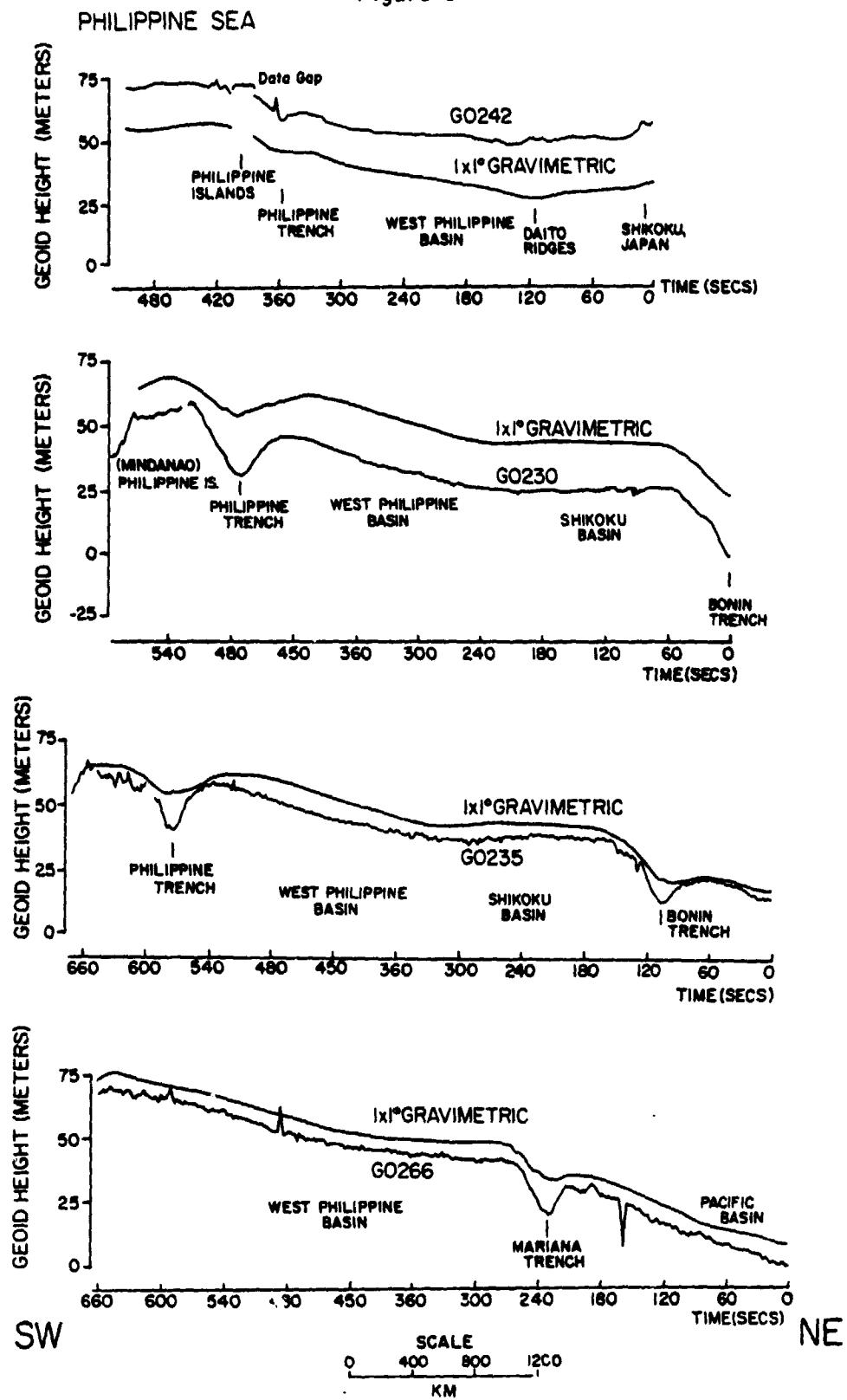
Comparison of Northwest Pacific gravimetric geoid with
GEOS-3 geoid height. GEOS-3 data are rougher line and are
labeled by the Lamont track number, gravimetric geoid
heights are the smooth line.

56

For an Airy model of two dimensional crust this function would be
(McKenzie and Bowin, 1976)

$$Z(k) = 2\pi G \ (\rho_c - \rho_w) \ e^{-kd} \ (1 - e^{-kt}) \tag{2}$$

where G is the gravitational constant

and ρ_c, ρ_w, are density of crust and water respectively

k is wavenumber in radians/km

d is depth of the water layer

t is the thickness of crustal layer

Utilizing the transfer function between the Fourier transform of gravity
and geoid (Chapman, 1979; A. Leeds, personal communication) we can
obtain the admittance between the Fourier transform of geoid and bathy-
metry for two dimensional Airy isostasy:

$$\mathscr{F}(N)/\mathscr{F}(b) = \frac{2\pi G}{\gamma |k|} \ (\rho_c - \rho_w) \ e^{-kd} \ (1 - e^{-kt}) \tag{3}$$

where $\mathscr{F}(N)$ is the Fourier transform of
geoid height

γ is normal gravity : 980 cm/sec

What this equation shows is that topography of the ocean floor will give
rise to undulations of the geoid which have identical frequencies but
amplitude decreasing with an increase in frequency at high wavenumber. Any
other model of compensation would also have identical frequencies but a
different amplitude function. This relationship is important in our
comparison study because it indicates that topographic features will
generate undulations of the geoid with similar frequencies. In the case
of the Hawaiian ridge this has been proven in a quantitative manner by
Watts (1978).

As an example of this relation between bathymetry and geoid consider the Aleutian trench (Figure 7). At the trench axis there is a topographic depression which is approximately 100 km wide, it has a gravity anomaly of similar width. Assuming two dimensionality it is possible to compute what the geoid anomaly is from the gravity anomaly (Talwani et al, 1972; A. Leeds, personal communication).

$$N(x) = (\frac{-1}{\pi\gamma}) = \int_{-\infty}^{+\infty} g(x') \log |x - x'| \, dx' \qquad (4)$$

This is a convolution integral and is the spatial equivalent of the transfer function between the Fourier transform of gravity and geoid (Chapman, 1979). Utilizing this formula and the observed gravity across the Aleutian trench, a two dimensional geoid profile has been computed and is also shown in Figure 7. Additionally a GEOS-3 profile and corresponding gravimetric geoid is shown. From this it is clear that above the trench there is a two dimensional geoid minimum with similar frequencies as the bathymetry. In both amplitude and wavelength this is identical to the observed minimum in GEOS-3 data. However, the trench low as seen in the 1° x 1° gravimetric geoid is much broader and shallower. On the basis of the relation between geoid and bathymetry having identical frequencies and our computation of the two dimensional geoid, it is clear that above the narrow Aleutian trench there is a geoid anomaly with similar frequency components. As the GEOS-3 altimeter records a signal similar in shape to the two dimensional geoid, it is reasonable to assume that the altimeter is faithfully measuring the geoid signal. In the 1° x 1° gravimetric geoid the trench low is much broader and shallower; in comparison to the GEOS-3 data and two dimensional geoid, the gravimetric geoid has less high frequencies and more energy in the

58

Figure 7
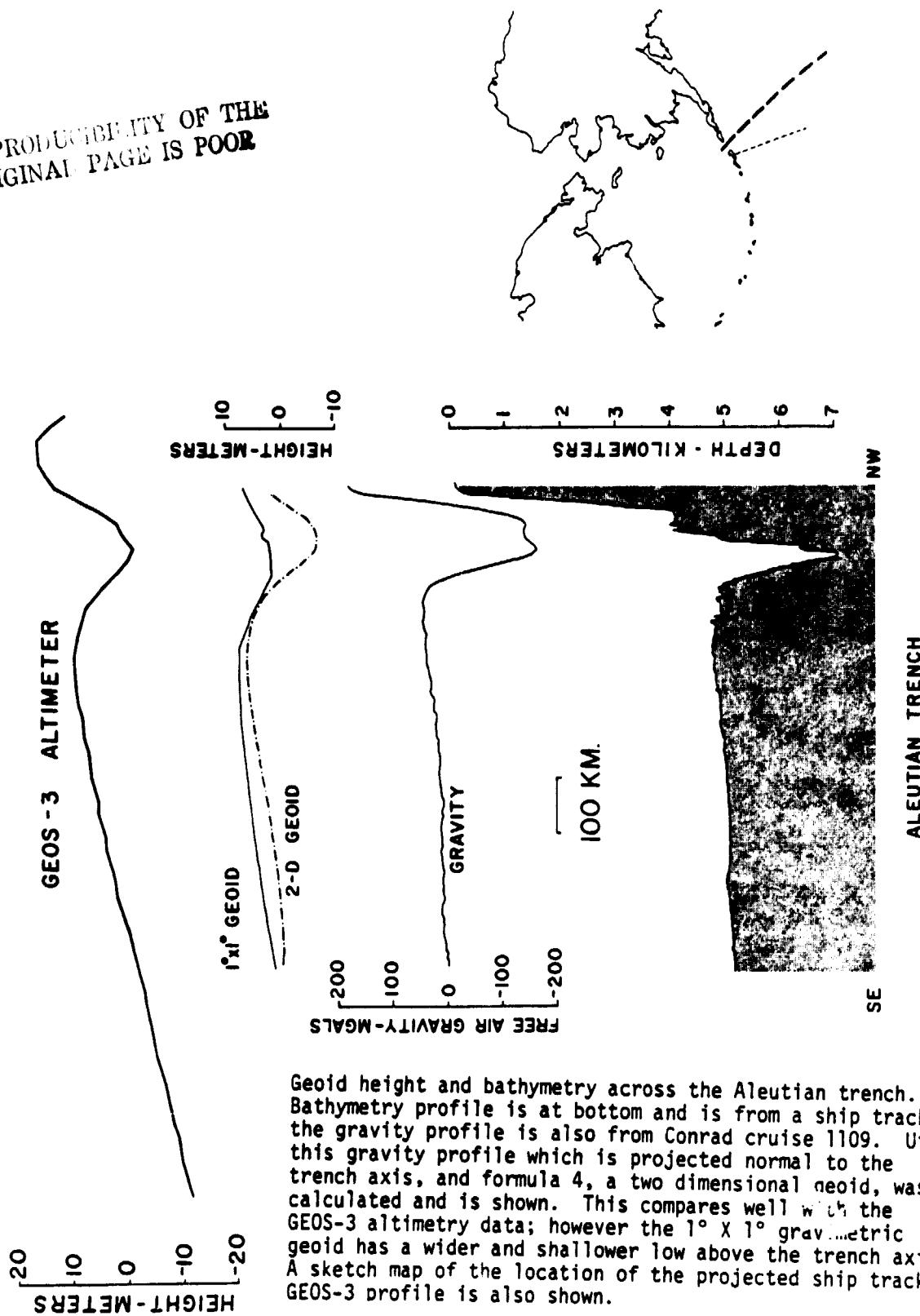
Geoid height and bathymetry across the Aleutian trench.
Bathymetry profile is at bottom and is from a ship track;
the gravity profile is also from Conrad cruise 1109. Utilizing
this gravity profile which is projected normal to the
trench axis, and formula 4, a two dimensional geoid, was
calculated and is shown. This compares well with the
GEOS-3 altimetry data; however the 1° X 1° gravimetric
geoid has a wider and shallower low above the trench axis.
A sketch map of the location of the projected ship track and
GEOS-3 profile is also shown.

59

medium frequency (wavelengths approximately 200 km) range. This is aliasing of the geoid signal and is due to our procedure in geoid construction of averaging gravity values over 1° squares.

This analysis of geoid height over the Aleutian trench indicates a limitation of 1° x 1° gravimetric geoids. In certain regions there can be energy in the geoid for wavelengths shorter than are resolved by averaging over 1° squares. In such areas it is necessary to construct gravimetric geoids by first averaging gravity values over smaller regions, perhaps 10' or 5' squares. Prior to averaging these values, it is possible to estimate how much high frequency information exists in the geoid. This can be done by multiplication of the Fourier transform of bathymetry and the admittance function. This gives an estimate of what the geoid heights would be at the shorter wavelengths. Another technique to estimate the high frequency geoid heights would be to first compute the Fourier transform of gravity values. After multiplication by the transfer function for a plane earth, this yields the Fourier transform of geoid height. This provides an estimate of the geoid height at the highest frequencies.

Data from the North Atlantic region are compared in Figure 8. Again the same features are noted as before, constant offsets and noisy altimeter data when the global mode is utilized. However, track GO096 exhibits another feature: there is a tilt of the altimeter measurements relative to the gravimetric geoid. Because this is such a long wavelength difference and does not appear in the other regions of the North Atlantic, we suspect it is due to very long wavelength errors in the computed satellite orbit. For this reason, Rummel and Rapp (1977) in correcting GEOS-3 data removed both a long wavelength orbital tilt in

60

Figure 8

61
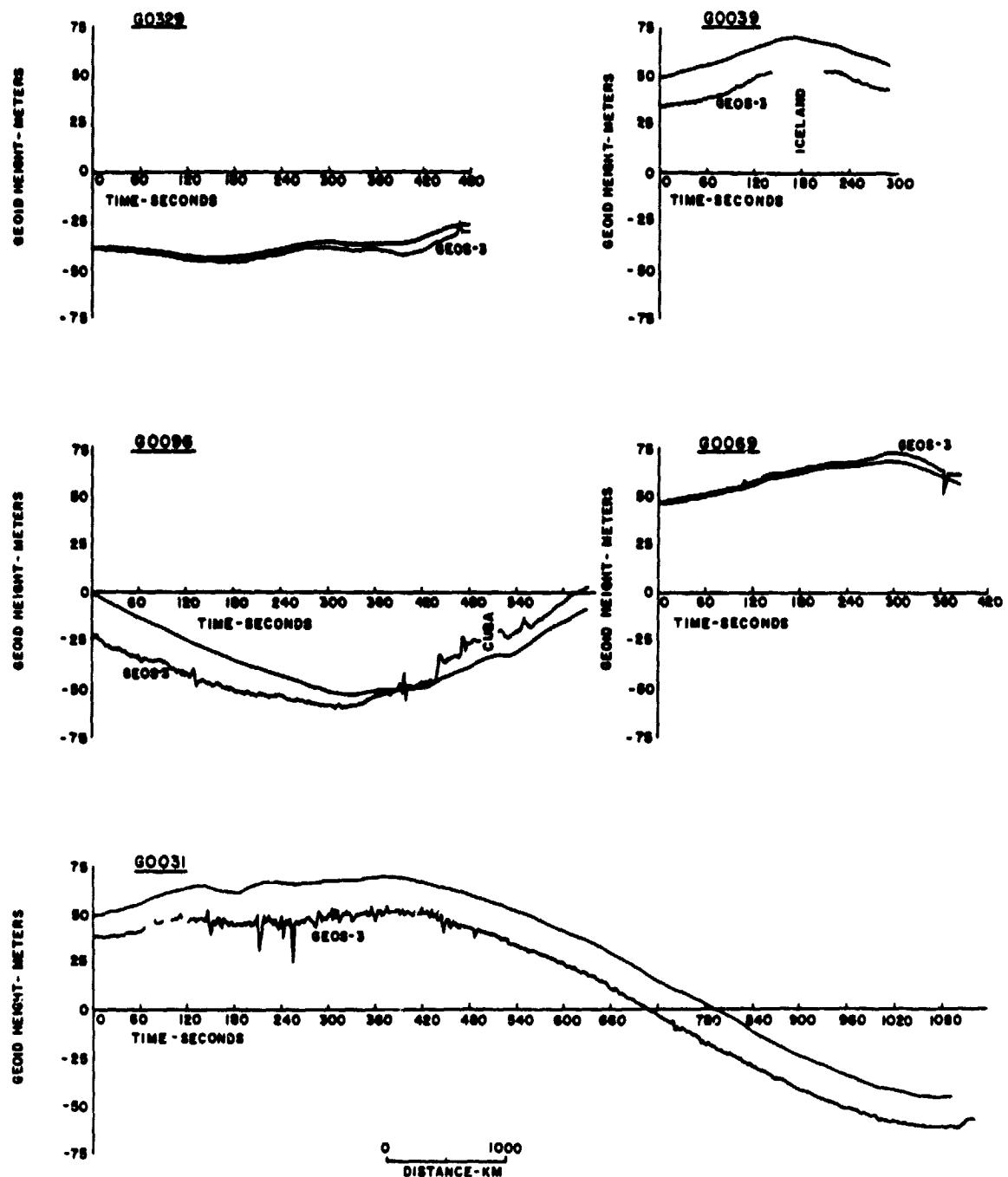
addition to constant offsets. Such a procedure is both justified and necessary in order to obtain good geoid estimates from the GEOS-3 altimeter.

In an effort to overcome such long wavelength differences, four tracks of GEOS-3 altimeter data were adjusted by requiring that they agree with each other at crossover locations and with the GEM-6 geoid. To do this adjustment the technique of Rummel and Rapp (1977) was utiliz '; this minimizes in a least square sense discrepancies due to bias and tilts. A comparison of these adjusted GEOS-3 geoid estimates with the Northwest Pacific gravimetric geoid is shown in Figure 9. For each track the GEOS-3 data and gravimetric geoid are both shown, directly above this the difference in height between the two is shown at a different scale. Thus for track G0266 agreement is quite good except at the Bonin trench; the rms discrepancy is 2.07 m (Table 3). For all of these tracks major disagreements of up to 10 m occur above the trench systems such as the Bonin, Mariana, Ryukyu, and Philippine trench. As discussed previously for the Aleutian trench, this discrepancy is due to inadequate resolution of the gravimetric geoid.

Other broad regions of difference occur; on track G0565 (Figure 9) southeast of the Mariana trench there is a broad disagreement of up to 5 meters. Because this area does not have the same quantity of gravimetric data as other regions, we suspect this is due to errors in the gravimetric geoid. When making detailed comparisons though, it becomes exceedingly difficult to ascertain whether there are slight errors in orbital computation or geoid calculation, or simply one could be seeing the effect of transient sea surface topography in the altimetry data. With gravimetric geoids what is needed are finer resolution grids and

COMPARISON OF GRAVIMETRIC GEOID WITH ADJUSTED GEOS-3 ALTIMETER MEASUREMENTS
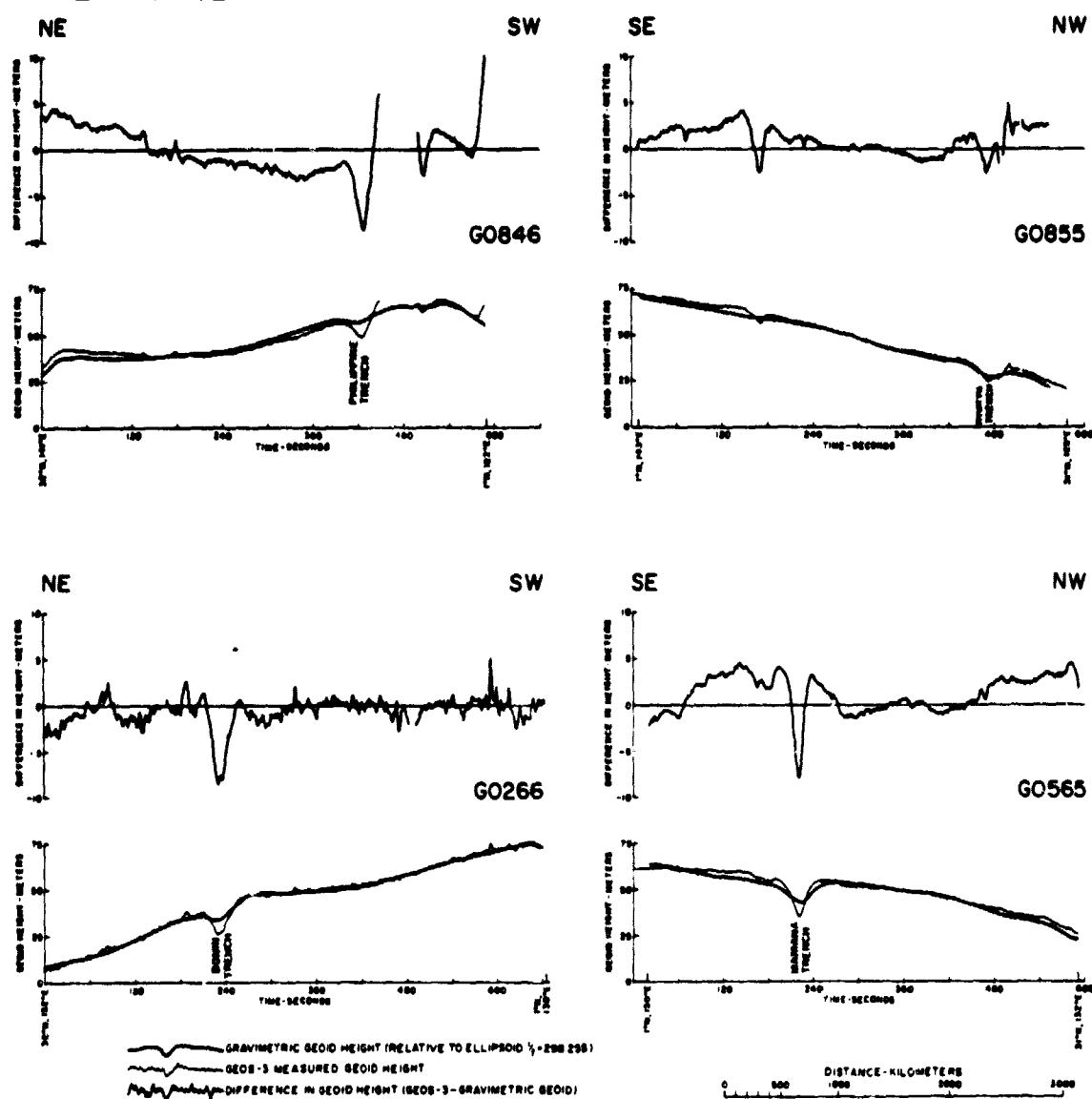

Figure 9
63

Table 3

RMS discrepancies between gravimetric geoids and adjusted GEOS-3 data
in Northwest Pacific

Track no.	RMS difference before adjustment	RMS difference after adjustment
G0846	12.34 meters	2.67 meters
G0855	4.82	1.69
G0565	4.ΓJ	2.36
G0266	10.27	2.07

detailed error analysis of their quality; in orbit determination the best calculations should be made to reduce radial errors to less than . meter.

The primary miss on of the GEOS-3 satellite was to determine information about the gravitational field of the earth; another question then arises as to what wavelength information will be best determined by satellite altimetry. For very long wavelengths, we have observed discrepancies between the altimetric geoids and gravimetric geoids. While we could not isolate the cause of this difference, it is likely to be partially due to radial orbital uncertainty as was demonstrated for SKYLAB by Marsh et al. (1976). Any such errors restrict the utility of satellite altimetry in obtaining information about the longest wavelengths of the earth's gravitational field. At the present time ground tracking of orbiting satellites has provided the best information on these longest wavelengths. In general, however, this is restricted to wavelengths with degree and order less than approximately 10. According to Khan (1976) the estimated accuracy in determination of individual spherical harmonic coefficients for degree 11 and higher is less than 60%. More recent gravitational field solutions such as GEM-9 (Lerch et al, 1977) may however be more accurate.

In order to answer the following question a hypothetical experiment can be performed. Compare an altimeter determining the geoid with a gravimeter measuring gravity. How well does each instrument perform in detecting its respective signal? The answer to this can be found by examining the relative properties of the geoid and gravity field and the comparative accuracies of altimeters and sea gravimeters.

Consider hypothetical measurements of geoid and gravity on a plane two dimensional earth. On this idealized body the geoid height is

estimated by utilizing sea surface measurements from a radar altimeter.
Due to the presence of oceanographic noise we assume uncertainties in
measurements of about 1 meter. Gravity is measured by a sea gravimeter
to an accuracy of 10 mgal limited by cross coupling and other errors.
Those are both somewhat arbitrary and conservative estimates but hope-
fully reflect the measurement situation to a certain degree. While
radar altimeters can measure sea surface height to possibly 10 cm
(SEASAT-A), due to unknown oceanographic noise the geoid can only be
determined to about 1 meter accuracy at present. Likewise, with marine
gravimeters a precision of several mgal is possible, but in analyzing
data due to two different ships at crossover, errors of 10 mgal are
common. In our hypothetical experiment these instruments detect the
geoid and gravity on a 5 km deep ocean overlying a 6 km thick crust.
There is topography compensated in an Airy manner; the amplitude spec-
trum of the topography is white with an amplitude of 3 km. The noise
spectra for each instrument is also considered to be white.

Then on the surface of the water the amplitude spectrum of gravity
is obtained from equation 2 and spectrum of geoid is obtained from
equation 3. A plot of these functions is in Figure 10. The vertical
scale has been adjusted so that 10 mgals is equivalent in height to 1
meter. Thus whenever one function is plotted higher than the other, it
indicates the higher function has a larger signal to noise ratio. From
this plot we see that for wavelengths longer than 628 km, an altimeter
will have a higher signal to noise ratio. For wavelengths shorter than
628 km a marine gravimeter will record with a better signal to noise
ratio. What we wish to indicate by this analysis is that below a
certain wavelength a marine gravimeter can determine the gravitational

66

Figure 10
Comparative accuracies of an altimeter and gravimeter in detecting the gravitational field on a plane earth. This

67
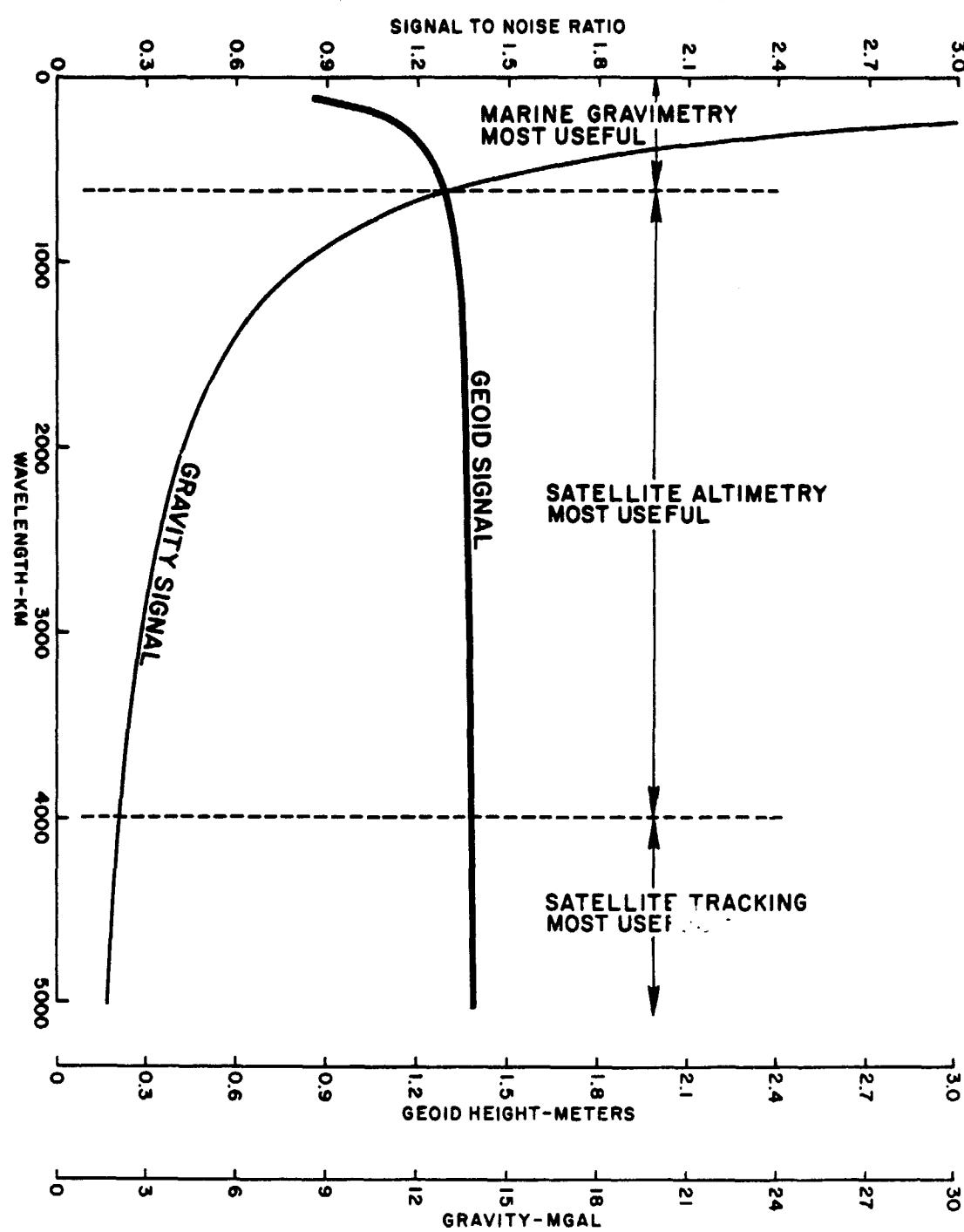
field with a better signal to noise ratio than a radar altimeter. For longer wavelengths a radar altimeter performs better. This critical wavelength depends on the noise levels of the individual instruments, in our hypothetical example it was 628 km. It should be understood though that a radar altimeter still records short wavelength information; this was demonstrated in our previous example over the Aleutian trench. As radar altimeters and marine gravimeters improve in their ability to detect the gravitational field, there will be a different critical wavelength below which a gravimeter performs better.

SUMMARY AND CONCLUSIONS

In comparing the GEOS-3 geoid estimates with the gravimetric geoids over the different oceans, several features emerge. Constant offsets and tilts cause large-scale discrepancies of up to 24 m rms (Table 1). These errors can be due to radial orbital uncertainty, scale errors in the geoid, lack of atmospheric correction in constructing the geoid, or bias errors in altitude determination by the altimeter. We did not discern the relative importance of these factors in causing the discrepancies. Over large scale topographic features such as the Aleutian Trench there can be a large geoid signal with wavelengths shorter than can be resolved by 1° X 1° gravimetric geoids.

In regions where there is good coverage of marine gravity data, and sufficient energy in the geoid at shorter wavelengths (less than 200 km) more detailed gravimetric geoids should be utilized. Examination of the topography and techniques utilizing the admittance between geoid and bathymetry should be useful in estimating the geoid signal at these short wavelengths.

After elimination of long wavelength differences, adjusted GEOS-3 data still show discrepancies with the gravimetric geoids. Over the trench systems of the western Pacific there were differences of up to 10 m. This is due to averaging gravity data over too large an area. In other regions there are discrepancies of several meters. Such differences indicate the need for estimation of the errors in geoid computations and the best possible orbital determinations for the GEOS-3 satellite.

Although some difficulties exist with constant offset a   g wavelength discrepancies, the GEOS-3 radar altimeter appear.   .ect geological features such as deep sea trenches and is an excellent instrument for acquiring measurements of the shape of the ocean surface. With the rapid mapping of the marine geoid on a global basis by GEOS-3 there will be a wealth of new information about the earth's gravitational field. It should be understood though that in detecting very short wavelength features of the field, a marine gravimeter will perform better than a radar altimeter. This is due to the long wavelengths being predominant in the geoid, while short wavelength anomalies are most obvious in gravity measurements.

CHAPTER II ACKNOWLEDGEMENTS:

Principal authors for Chapter II were Michael E. Chapman and Manik Walwani of Lamont-Doherty Geological Observatory of Columbia University, Palisades, New York 10964.

REFERENCES

Chapman, M.E., Techniques for interpretation of geoid anomalies. J. Geophys. Res., this volume, 1979.

Heiskanen, W.A., The Columbus Geoid. Trans. A.G.U., 38, 841-848, 1957.

Hendershott, M.C., Tide model ocean tides. Trans. A.G.U., 54, 76-86 1973.

Kahle, H.G., M. Chapman, and M. Talwani, Detailed 1° X 1° gravimetric Indian Ocean geoid and comparison with GEOS-3 radar altimeter geoid profiles. Geophys. J. Roy. astr. Soc., in press, 1978.

Kahle, H.G., and M. Talwani, Gravimetric Indian Ocean geoid. Z. für Geophysik, 39, 167-187, 1973.

Khan, M.A., Comparative evaluation of recent global representations of Earth's gravity field, Geophys. J. Roy. astr. Soc., 46, 535-553, 1976.

Lerch, F.J., J.E. Brownd, and S.M. Klosko, Gravity model improvement using GEOS-3 (GEM-9 and 10) - Abstract only. Trans. A.G.U., 58, 371, 1977.

Marsh, J.G., B.C. Douglas, S. Vincent, and D.M. Walls, Tests and comparisons of satellite-derived geoids with SKYLAB altimeter data. J. Geophys. Res., 81, 3594-3598, 1976.

Marsh, J.G. and S. Vincent, Global detailed geoid computation and model analysis. Geophys. Surv., 1, 481-511, 1974.

Martin, C.F. and M.L. Butler, Calibration results for the GEOS-3 altimeter. NASA Contractor Report, NASA CR-141430, 86pp., 1977.

McKenzie, D. and C. Bowin, The relationship between bathymetry and gravity in the Atlantic Ocean. J. Geophys. Res., 81, 1903-1915, 1976.

Moritz, H., Precise gravimetric geodesy. Report No. 219, Dept. of Geodetic Science, Ohio State University, 1974.

Rapp, R.H. and R. Rummel, Methods for the computation of detailed geoids and their accuracy. Report No. 233, Dept. of Geodetic Science, Ohio State University, 1975.

Rummel, R. and R. Rapp, Undulation and anomaly estimation using GEOS-3 altimeter data without precise satellite orbits. Bull. Geod., 51, 73-88, 1977.

Smith, D.E., F.J. Lerch, J.G. Marsh, C. A. Wagner, R. Kolenkiewicz, and M.A. Khan, Contributions to the national geodetic satellite program by Goddard Space Flight Center. J. Geophys. Res., 81, 1006-1026, 1976.

Strange, W.E., S.F. Vincent, and R.H. Berry, Detailed gravimetric geoid for the United States. In: The Use of Artificial Satellites for Geodesy, S. Henriksen, A. Mancini, B. Chovitz (eds)., Geophys. Monogr. 15, American Geophys. Union, Washington, D.C., 169-176, 1972.

Talwani, M., H. Poppe, and P. Rabinowitz, Gravimetrically determined geoid in the western North Atlantic. In: Sea surface topography from space, NOAA Tech. Rept. ERL-228- AOML 7-2, 2, 1-34, 1972.

Von Arx, W.S., Level-surface profiles across the Puerto Rico trench. Science, 154, 1615-1654, 1966.

Wagner, C.A., F.J. Lerch, J.E. Brownd, and J.A. Richardson, Improvement in the geopotential derived from satellite and surface data (GEM-7 and 8). NASA/GSFC Doc. X-921-76-20, Greenbelt, Md., 1976.

Watts, A.B., A preliminary analysis of geoid heights derived from GEOS-3 altimeter data along the Hawaiian-Emperor seamount chain. J. Geophys. Res., this volume, 1978.

Watts, A.B. and A. Leeds, Gravimetric geoid in the Northwest Pacific Ocean. Geophys. J. Roy. astr. Soc., 50, 249-278, 1977.

Chapter III

Techniques for Interpretation of Geoid Anomalies

Introduction

When a new scientific instrument is developed and utilized for the study of the earth, there are always new and exciting discoveries. Such an instrument is the GEOS-3 radar altimeter, which has been used to make measurements of the shape of the sea surface over most of the worlds oceans. After corrections for errors and oceanographic effects this data is a determination of the marine geoid.

Given the shape of this gravitational equipotential surface inferences can be made about the density inhomogeneities within the earth which cause geoid undulations. Prior to satellite altimetry determination of the geoid was the primary goal. Now with geoid measurements via satellite altimetry new questions can be asked. Why does the geoid have its particular shape and what are the structures within the earth which cause geoid anomalies? In order to utilize altimetry data in studying the earth's interior mathematical techniques are necessary. For this reason we have developed several new analytic techniques for interpretation of geoid anomalies.

Our procedure is to initially compute formulas for the geoid anomaly over idealized bodies. These serve to demonstrate various properties of geoid anomalies. Then formulas are developed for computing the geoid anomaly over an arbitrary two dimensional body. Most general procedures require the calculation of geoid anomalies over three dimensional bodies. In order to understand the relationship between the gravity anomaly and the geoid, techniques in the frequency domain are developed. Finally, as practical examples, calculations of the geoid anomaly across continental margins and over seamounts are compared with actual geoid measurements.

Basic Formulas and Ideal Bodies

In dealing with geoid anomalies we are concerned with the computation of the shape of an equipotential surface, this surface being primarily ellipsoidal with small undulations due to an anomalous potential. Anomalous potential is the difference between total potential and the normal potential due to the reference ellipsoid. If we know the anomalous potential, then the geoid anomaly is given by Brun's formula (Heiskanen & Moritz, 1967).

$$N = \frac{T}{\gamma} \tag{1}$$

Where N is geoid height, T is the anomalous potential, and γ is normal gravity - 980 cm/sec^2. A point mass will have an anomalous potential of

$$T = \frac{G M}{R} \tag{2}$$

where G is the Newtonian constant 6.67×10^{-8} cm^3/gm sec^2, M is the mass, and R is the distance between the point mass and the observation point. This expression has two conventions: potential is zero at infinity and positive everywhere else. Thus an excess mass corresponds to positive potential and positive geoid height. Our basic problem then is how to compute the geoid anomaly due to an assemblage of point masses.

$$N(x',y',z') = \frac{G}{\gamma} \iiint \frac{\rho \; dx \, dy \, dz}{\left[(x-x')^2 + (y-y')^2 + (z-z')^2\right]^{1/2}} \tag{3}$$

Primed coordinates indicate the observation point, unprimed coordinates are the integration variable, and ρ is density. Initially we compute the geoid over ideal bodies; lines, sheets, and rectangles in both two and three dimensions.

A finite horizontal line located at y_0, z_0 with linear density λ (gm/cm) has a corresponding geoid anomaly of (Figure 1a)

$$N = \frac{G}{\gamma} \int_{x_1}^{x_2} \frac{\lambda \; dx}{\left[(x-x')^2 + (y_0-y')^2 + (z_0-z')^2\right]^{1/2}} \tag{4}$$

This, when integrated, becomes

75

$$N = \frac{G\lambda}{\gamma} \log_e \left\{ \frac{(x_2-x') + \left[(x_2-x')^2 + (y_0-y')^2 + (z_0-z')^2\right]^{1/2}}{(x_1-x') + \left[(x_1-x')^2 + (y_0-y')^2 + (z_0-z')^2\right]^{1/2}} \right\} \qquad (5)$$

Figure 1B shows a plot of this function, the geoid height is always positive and decays to 0 in the limit as $|y|$ goes to infinity.

If the finite horizontal line is integrated along the z axis, one obtains the geoid anomaly over a finite vertical sheet (Figure 2a). This integral is (see appendix for details)

$$N = \frac{G\sigma}{\gamma} \{ G_1(x_2,z_2) - G_1(x_2,z_1) - G_1(x_1,z_2) + G_1(x_1,z_1) \} \qquad (6)$$

where σ is the surface density (gm/cm^2) and

$$G_1(x,z) = (z-z') \log_e \left\{ (x-x') + \left[(x-x')^2 + (y_0-y')^2 + (z-z')^2\right]^{1/2} \right\}$$

$$- (z-z') + (x-x') \log_e \left\{ (z-z') + \left[(x-x')^2 + (y_0-y')^2 + (z-z')^2\right]^{1/2} \right\} \qquad (7)$$

$$+ \left| y_0-y' \right| \sin^{-1} \left[\frac{- (x-x')^2 - (y_0-y')^2 - (x-x') \left[(x-x')^2 + (y_0-y')^2 + (z-z')^2\right]^{1/2}}{\left| (x-x') + \left[(x-x')^2 + (y_0-y')^2 + (z-z')^2\right]^{1/2} \right| \left[(x-x')^2 + (y_0-y')^2\right]^{1/2}} \right]$$

and restricting $(z-z') > 0$

A plot of this function is in Figure 2B. While always positive, the geoid height decays at a slower rate than the finite horizontal line.

Our next ideal body is an infinite horizontal line. While the actual integration is quite simple we utilize a slightly longer derivation in order to show the relationship between gravity, deflection of the vertical, and the geoid. This is also the basis for a later derivation in the frequency domain. In the two dimensional geoid calculations a complication arises, involving the zero reference level. Calculation of the geoid anomaly over the infinite horizontal line will illustrate this complexity.

Ⓐ

FINITE HORIZONTAL LINE

Ⓑ
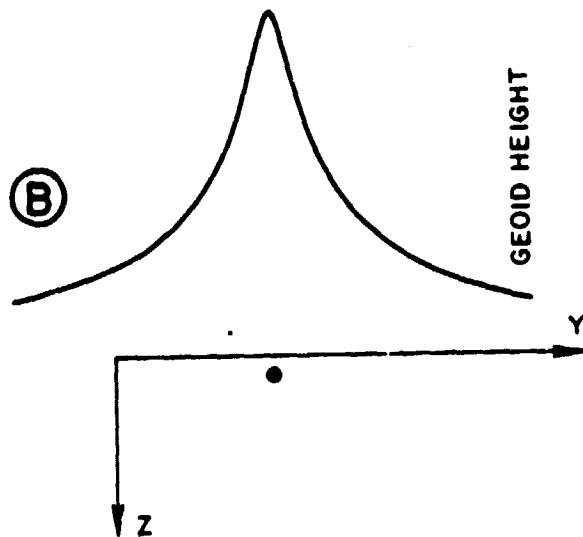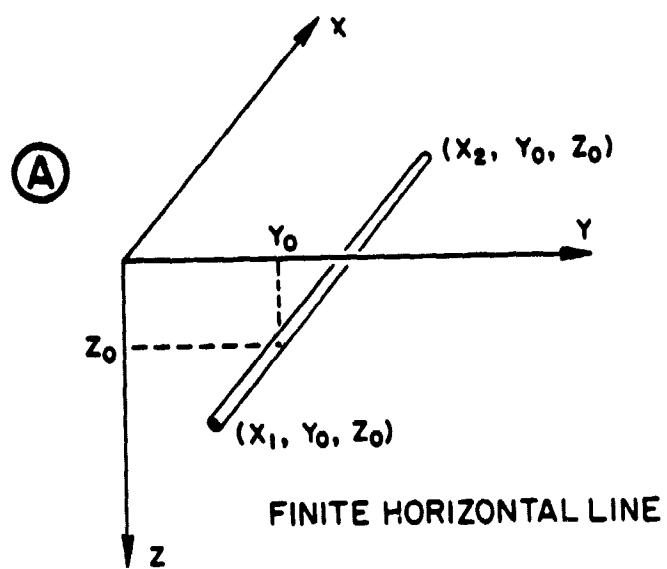
GEOID HEIGHT

Calculation of geoid anomaly over a finite horizontal line and its resultant geoid height.

Figure 1
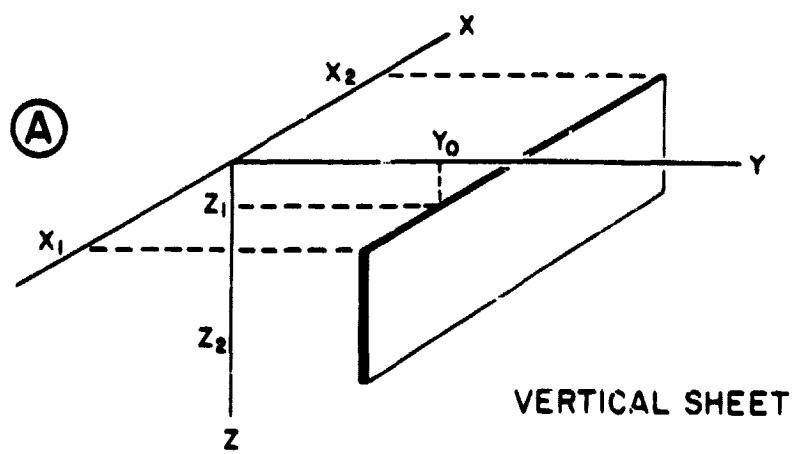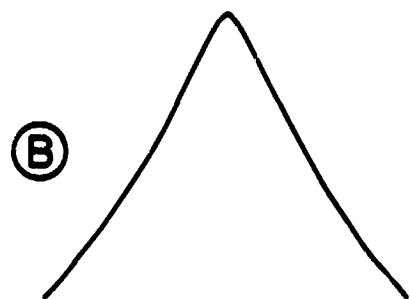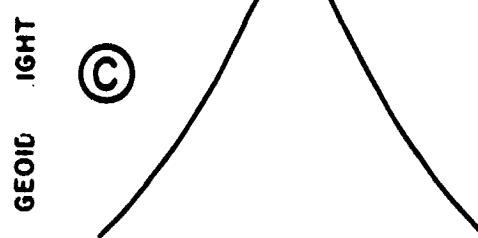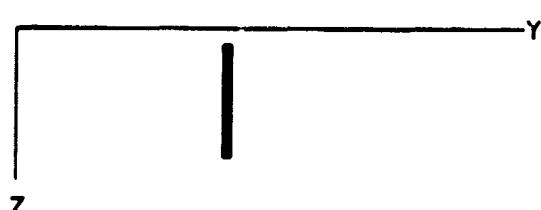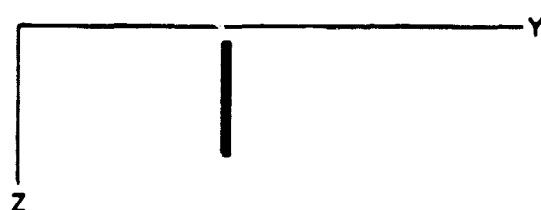
Calculation of geoid anomaly over a vertical sheet. Resultant geoid heights for the three dimensional (finite) and two dimensional (infinite) vertical sheet are plotted.

Figure 2

78

Due to an infinite horizontal line located at $y=0$, $z=z_0$, the horizontal component of gravity on the $z=0$ plane is

$$F_{g}^{h} = -2 G \lambda \frac{y \hat{y}}{(y^2 + z_0^2)}$$
(8)

Deflection of the vertical is defined to be the angle between a vertical line along the z-axis and the local direction of gravity (Figure 3). On a plane earth the gravitational attraction has a vertical component of $\gamma + Fg^v$, where γ is normal gravity and Fg^v is the vertical component of the gravitational attraction due to anomalous mass. The horizontal component is simply Fg^h, thus

$$\tan \delta = \frac{Fg^h}{\gamma + Fg^v}$$
(9)

where δ is deflection of vertical. Because $Fg^v \ll \gamma$, and $\delta \approx 0$

$$\delta = \frac{Fg^h}{\gamma} = \frac{-2G\lambda}{\gamma} \frac{y}{(y^2 + z_0^2)}$$
(10)

Deflection of the vertical in the y direction is just the slope of the geoid.

$$\delta = + \frac{\partial N}{\partial y} = \frac{-2G\lambda}{\gamma} \frac{y}{(y^2 + z_0^2)}$$
(11)

Solving for geoid height N we obtain:

$$N = - \frac{G\lambda}{\gamma} \log_e (y^2 + z_0^2) \Big|_{y_0}^{y}$$
(12)

where y_0 is an arbitrary constant of integration. With the two dimensional potential the usual procedure is to let the potential be zero at unit distance, or when $(y_0^2 + z_0^2) = 1$; it must be zero at some finite distance. This has two effects; it causes the absolute amplitude of N to depend upon the units used, and it introduces both positive and negative geoid heights for a positive mass. In dealing with two dimensional bodies it is necessary to ignore this arbitrary constant level. Thus in two dimensional models only

79

TWO DIMENSIONAL LINE
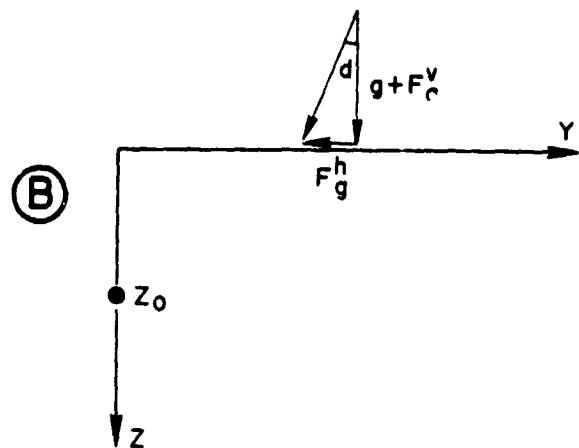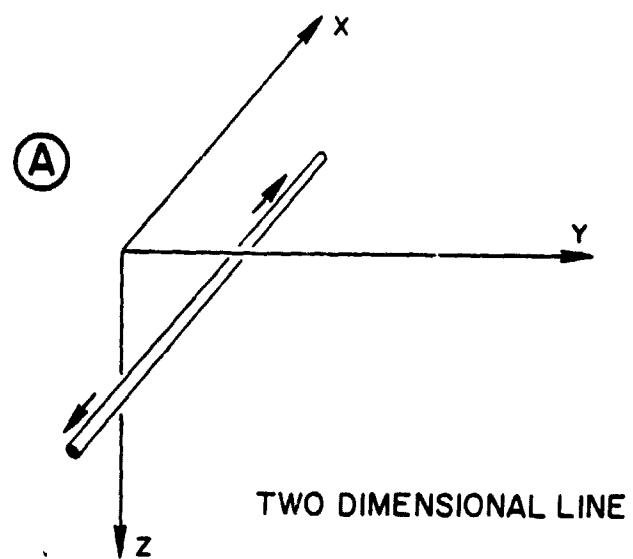
Calculation of geoid anomaly over an infinite horizontal line. In B the horizontal attraction of gravity in F_g^h, the vertical attraction due to the line is F_g^v. Acceleration due to the earth is g, and deflection of the vertical is d.

Figure 3

deviations from a constant level are important.

After setting the potential at zero for unit distance we obtain for the geoid:

$$N = - \frac{G \lambda}{\gamma} \log_e (y^2 + z_0^2) \tag{13}$$

When the infinite horizontal line is integrated along the z axis, one obtains the geoid anomaly over a two dimensional vertical sheet.

$$N = - \frac{\dot{G} \sigma}{\gamma} \int_{z_1}^{z_2} \log_e [(y_0-y')^2 + (z-z')^2] \, dz \tag{14}$$

and after integration

$$N = - \frac{G \sigma}{\gamma} \left\{ (z-z') \log_e [(y_0-y')^2 + (z-z')^2] \right.$$
$$\left. - 2z + 2 \left| y_0-y' \right| \, \text{Tan}^{-1} \frac{(z-z')}{\left| y_0-y' \right|} \right\} \Bigg|_{z_1}^{z_2} \tag{15}$$

This anomaly is shown in figure 2c, for comparison purposes in figure 2b there is a geoid anomaly over a finite vertical sheet. Obviously they are quite similar in shape. This shows that two dimensional methods might approximate three dimensional ones in spite of the arbitrary height difference.

A two dimensional rectangle is obtained by an integration of the mass line over both the y and z axis (Figure 4a).

$$N = - \frac{G \sigma}{\gamma} \int_{z_1}^{z_2} \int_{y_1}^{y_2} \log_e [(y-y')^2 + (z-z')^2] \, dy \, dz \tag{16}$$

after integration (see appendix for details)

$$N = - \frac{G \sigma}{\gamma} [G_2 (y_2, z_2) - G_2 (y_1, z_2) - G_2 (y_2, z_1) \tag{17}$$
$$+ G_2 (y_1, z_1)]$$
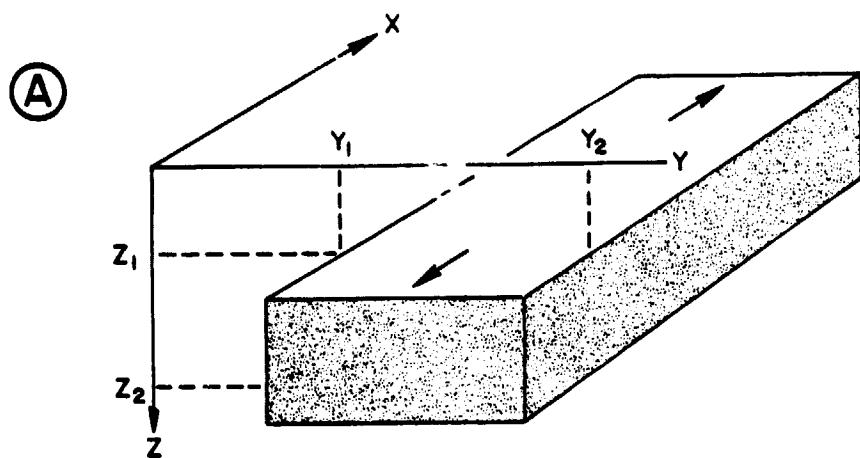
Ⓐ

TWO DIMENSIONAL RECTANGLE

Ⓑ

GEOID HEIGHT
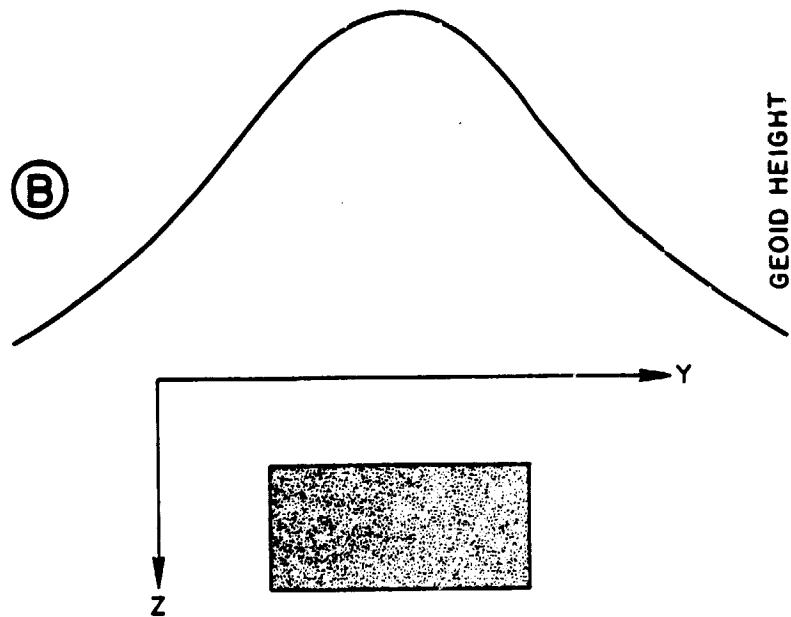
Calculation of geoid anomaly over a two dimensional rectangle.
Note that the geoid anomaly is never-flat, rather it is always
curving.

Figure 4

where

$$G_2 (y, z) = (y-y') \{(z-z') \log_e [(y-y')^2 + (z-z')^2] - 2 z + 2 \left| y-y' \right| \cdot$$ (18)

$$Tan^{-1} \frac{(z-z')}{\left| y-y' \right|} \} -2 y z + [(z-z')^2 + (y-y')^2] Tan^{-1} \frac{(y-y')}{(z-z')} + (z-z') (y-y')$$

assuming $(z-z') > 0$

In Figure 4b there is a plot of this anomaly. Over the rectangle the geoid is not flat, it is always concave downwards until a point of inflection above the edge of the body. The implication of this curvature is that in constructing geoid models the anomalous mass must integrate to zero, otherwise there will be a long wavelength curvature of the geoid anomaly. To make the anomalous mass sum to zero, both negative and positive densities are utilized.

Integral Formulas For Two Dimensional Bodies

While analytic solutions for ideal bodies have an initial utility in under-standing properties of geoid anomalies and verifying other formulas they are of limited utility in learning about the earth. Better models of the earth involve specifying densities of bodies of arbitrary shape and computing the resultant geoid anomaly. In order to achieve this result we have developed several techniques for the computation of geoid anomalies over bodies which are polygons in either two or three dimensions. These enable the models of virtually any shape to be calculated, the desired accuracy in shape only limited by the number of specified sides.

A simple numerical solution to computing geoid anomalies was originally developed by Talwani, Poppe and Rabinowitz (1972) in order to compute the geoid across a two dimensional structure from the gravity. For a given polygon in two dimensions the horizontal component of gravity is computed with the line integral method of Talwani et al. (1959), then after division by normal gravity the deflection of vertical is obtained.

83

$$\delta = \frac{Fg^h}{\gamma} \qquad (19)$$

As in our previous derivation for the infinite line, this is the slope of the geoid

$$\delta = \frac{dn}{dy} \qquad (20)$$

so finally

$$N = \int_{y_0}^{y} \delta \, (y) \, dy \qquad (21)$$

This final integration is done with the trapezoidal rule or else Simpson's formula. Although it is a numerical solution it produces very accurate results in excellent agreement with exact analytic solutions.

For geophysical interpretation of two dimensional bodies of arbitrary shape a method has been developed to directly compute the geoid anomaly over a polygon in two dimensions. In this technique the body is specified by the location of each vertex and the density of the body, as in Figure 5a. For any arbitrary two dimensional body the geoid anomaly is

$$N = -\frac{G\rho}{\gamma} \iint_S \log_e [(y-y')^2 + (z-z')^2] \, dy \, dz \qquad (22)$$

To obtain a direct analytic solution for a two dimensional polygon we utilize Stokes' theorem to convert this surface integral to the following line integral:

$$N = -\frac{G\rho}{\gamma} \oint \{(y-y') \log_e [(y-y')^2 + (z-z')^2] - 2 (y-y^1) + 2 (z-z')$$
$$\mathrm{Tan}^{-1} \frac{(y-y')}{(z-z')} \} \, d \, z \qquad (23)$$

and restricting $(z-z') > 0$

Calculation of geoid anomaly over a two dimensional polygon.
Integration proceeds in a clockwise fashion when looking in the
positive $\hat{x}$ direction. Integral is computed by evaluating formula
24 for the i'th line segment and summation over all segments with
formula 25. Note the rapid decrease in gravity compared to the
slow decay in the geoid anomaly.

Ⓐ

Ⓑ

GEOID

GRAVITY

Y_{i-1} Y_i

i'th line segment

Y

z

Y

X

z

1

2 3

4

5

TWO DIMENSIONAL POLYGON
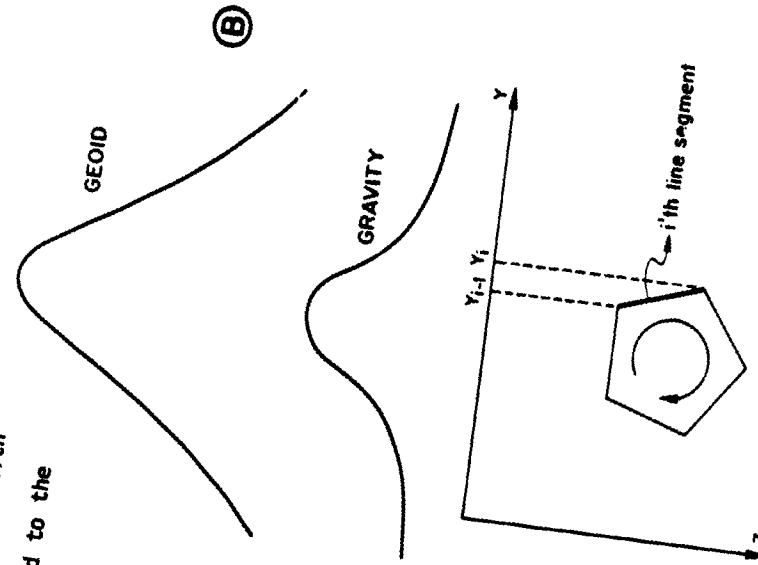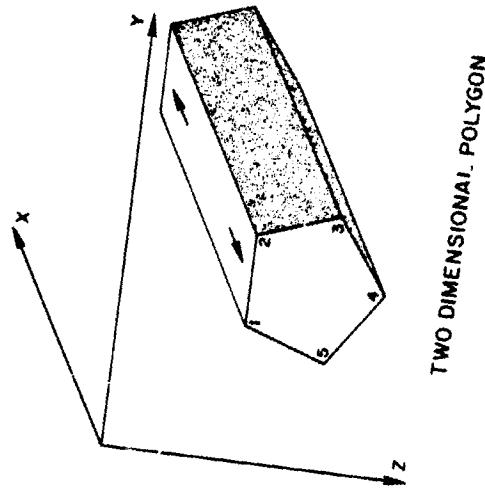
Figure 5

85

With a polygonal approximation each side is defined by the formula:

$$z = m_i \, y + b_i$$

then the contribution to the geoid anomaly due to the ith line segment is: (see appendix for details)

$$
\begin{aligned}
h_i = \Bigg[& m_i \frac{(y-y')^2}{2} \log_e [(y-y')^2 + (z-z')^2] - m_i \frac{(y-y')^2}{2} \\
& + \frac{m_i^2 A_2 \, (y-y')}{(1+m_i^2)} - \frac{m_i \, (m_i^2 - 1) \, A_2^2}{2(1+m_i^2)^2} \log_e [(y-y')^2 + (z-z')^2] \\
& -2 \frac{m_i^2 A_2^2}{(1+m_i^2)^2} \mathrm{Tan}^{-1} \left[\frac{(1+m_i^2) \, (y-y') + m_i A_2}{A_2} \right] \qquad (24) \\
& -m_i(y-y')^2 + z^2 \, \mathrm{Tan}^{-1} \frac{(y-y')}{z} \\
& -\frac{c_i D_i^2}{(1+c_i^2)^2} \log_e \left[\frac{(1 + c_i^2) \, z^2 + 2 \, c_i \, D_i \, z + D_i^2}{D_i^2} \right] \\
& + \\
& + \frac{D_i \, z}{(1+c_i^2)} + \frac{(1-c_i^2) \, D_i^2}{(1+c_i^2)^2} \mathrm{Tan}^{-1} \left(\frac{y-y'}{z} \right) \Bigg] \Bigg|_{y_{i-1}}^{y_i}
\end{aligned}
$$

with $A_2 = m_i \, y' + B_i - z'$

$c_i = 1 / m_i$

$D_i = -B_i/m_i - y'$

$m_i =$ slope of line segment

$B_i =$ intercept of line segment

$Z = m_i \, y + b_i$

86

thus the total geoid anomaly is

$$N = \frac{-G \rho}{\gamma} \sum_{i=1}^{L} n_i \qquad \text{L = number of segments}$$

Due to singularities in the integral formula the following special cases need also be considered:

    a) $m_i = 0$ then $n_i = 0$ (slope of line segment is zero)

    b) $c_i = 0$ then   (slope of line segment is infinite)

$$n_i = \{(y_i-y')[(z-z')\log_e[(y_i-y')^2 + (z-z')^2] - 2(z-z')$$

$$+ 2|y_i-y'| \; \text{Tan}^{-1}\frac{(z-z')}{|(y_i-y')|}] - 2(y_i-y')z \qquad (26)$$

$$+ [(y_i-y')^2 + (z-z')^2] \; \text{Tan}^{-1}\frac{(y_i-y')}{(z-z')}$$

$$+ (y_i-y')(z-z')\} \Big|_{z_i-1}^{z_i}$$

    c) $B_i/m_i + y' = 0$ then   (the extension of line segment passes through observation point)

$$n_i = \{\frac{z^2}{2m_i}\log_e[(1+\frac{1}{m_i^2})z^2] - \frac{3z^2}{2m_i} + z^2\;\text{Tan}^{-1}(\frac{1}{m_i})\}\Big|_{z_i-1}^{z_i} \qquad (27)$$

assuming $z' = 0$, $z > 0$

For a given geophysical model a number of individual bodies are specified by their respective densities and shape as defined by a number of vertices of a polygon. For each body the geoid effect is calculated using either the numerical technique in formula (21) or the analytic technique of formula (24). After summation over all bodies the total geoid height due to the model is obtained. In practice both of these mathematical techniques yield identical results. In Figure 5b there is a sample computation of geoid height and vertical component of gravitational attraction over a pentagonal body. The geoid has a shape similar to the gravity anomaly but is much wider; the geoid height decays with distance at a slower rate.

In modeling two precautions are necessary. First the constant level of the geoid height must be ignored. This is because of the arbitrary location of zero potential for a two dimensional body. A second precaution concerns the specification of densities. In geoid calculations the anomalous density must be utilized rather than the total density. This is because Brun's formula (formula (1)) requires anomalous potential rather than total potential. If a given model is in isostatic equilibrium this second precaution requires that the sum of the anomalous masses in a given column be zero. This requirement is different than in standard gravity models If the total mass did not sum to zero then a constant gravity value could always be subtracted from calculated gravity to obtain the gravity anomaly. In geoid computations this procedure does not work, the reason being that a two dimensional rectangle (as discussed previously) does not have a flat geoid anomaly above it, whereas in gravity calculations a two dimensional rectangle, except for edge effects, has a flat gravity anomaly.

As a practical example of the utility of these methods we consider the study of an Atlantic type continental margin. In the transition between the deep sea and the continental marjin of Nova Scotia in Eastern Canada, the ocean bottom changes in depth by five kilometers. Likewise the ocean surface changes in height by six meters (Figure 6). This change in geoid height has been determined from the GEOS-3 satellite. A natural question arises then, what is the cause of this change in geoid height? To help answer this question, a two dimensional density model of the Nova Scotia margin has been constructed (Figure 6). This is a simple three component model with water, crust, and mantle material. It is fully compensated in an Airy manner. Utilizing the two dimensional technique described in this section, we have calculated the geoid anomaly over this model. As Figure 6 indicates, the calculated
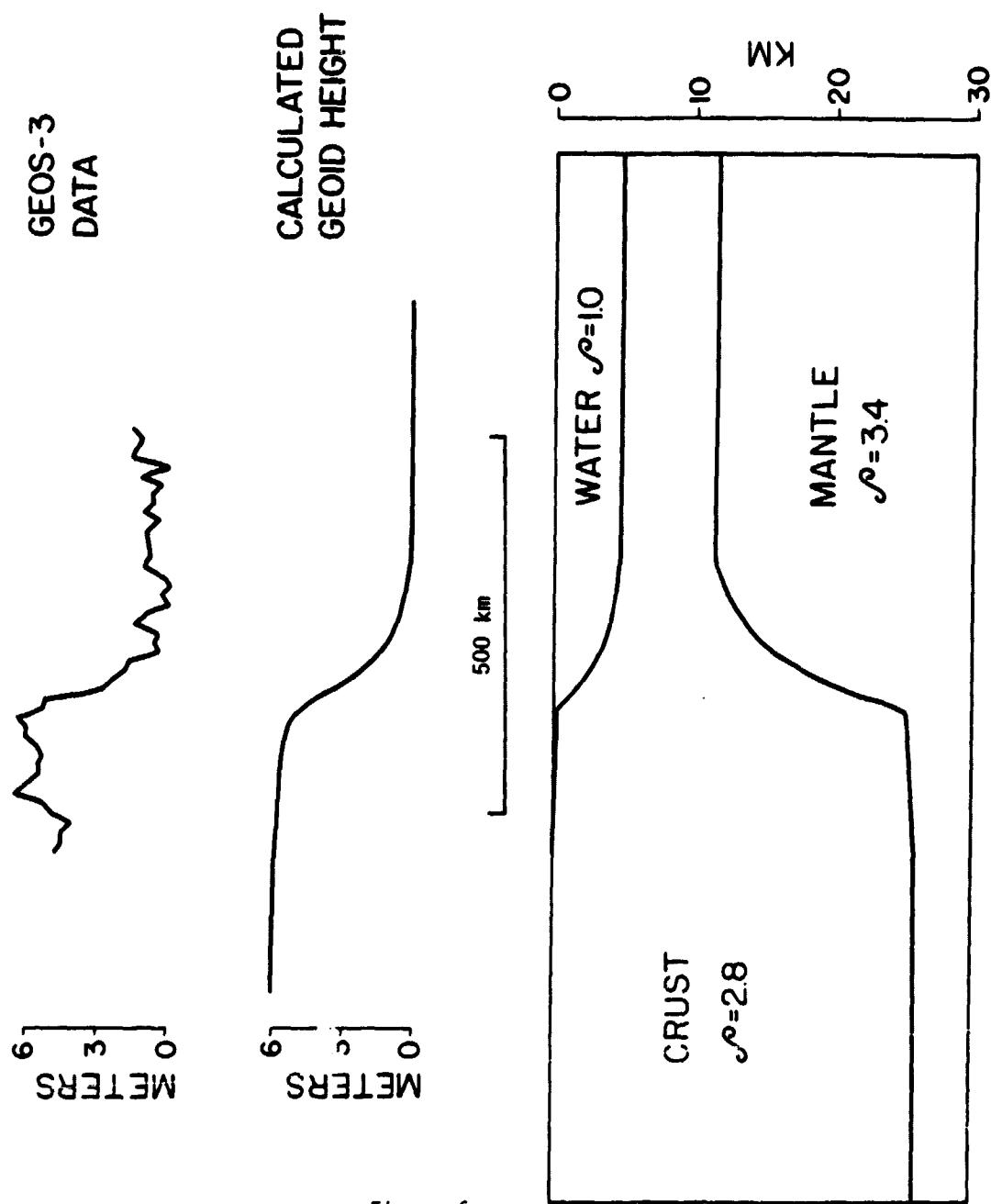
Figure 6

Geoid anomaly across Nova Scotia margin, left end of GEOS-3 profile is at 44.5°N, 63.25°W and right end is at 40°N, 58.7°W.

89

geoid height is in good agreement with the observed GEOS-3 data. It can be
concluded that a simple density model of the Nova Scotia margin which is in
isostatic equilibrium is capable of successfully modeling the observed GEOS-3
data. Due to the noise level of the data a more elaborate model was believed
unjustified.

Geoid Calculations For Three Dimensional Bodies

While the two dimensional approximation has a certain utility, more realistic geophysical modeling requires the computation of the geoid anomaly due to bodies of arbitrary shape and density in three dimensions. In the method now developed the shape of the body is prescribed to be a polyhedron. Any shape can be approximated by this method by simply including sufficient detail with many facets. This same technique was developed in gravity modeling by Coggon (1976), Paul (1974), and Barnett (1976).

In Figure 7a we illustrate a polyhedron which is assumed to have constant density. To calculate the geoid height for this body the fundamental integral formula 3 has to be solved. Conceptually our method of solution is quite simple. This volume integral is converted to a surface integral by the divergence theorem. For each facet of the polyhedron this surface integral can be solved by conversion to a line integral via Stokes' theorem. Thus the total volume integral is calculated by a summation of surface integrals, one for each polygonal facet. Each surface integral is calculated by a summation of line integrals, one for each line segment on a given facet. This is an exact analytic technique and is accurate for any shape which can be approximated as a polyhedron.

Rewriting equation 3 in the form

$$N = \frac{G\rho}{\gamma} \iiint_V \nabla \cdot (\tfrac{1}{2}\hat{r}) \ dv$$

where $\hat{r}$ is the unit vector in the radial direction

(A)

X

Y

2

$\hat{U}_4$

1

$\hat{U}_4$ perpendicular to facet

Z

THREE DIMENSIONAL POLYHEDRON

(B)

η

θ

1

$\hat{U}_1$

$\hat{U}_4$

3

2

$\hat{U}_2$

ζ
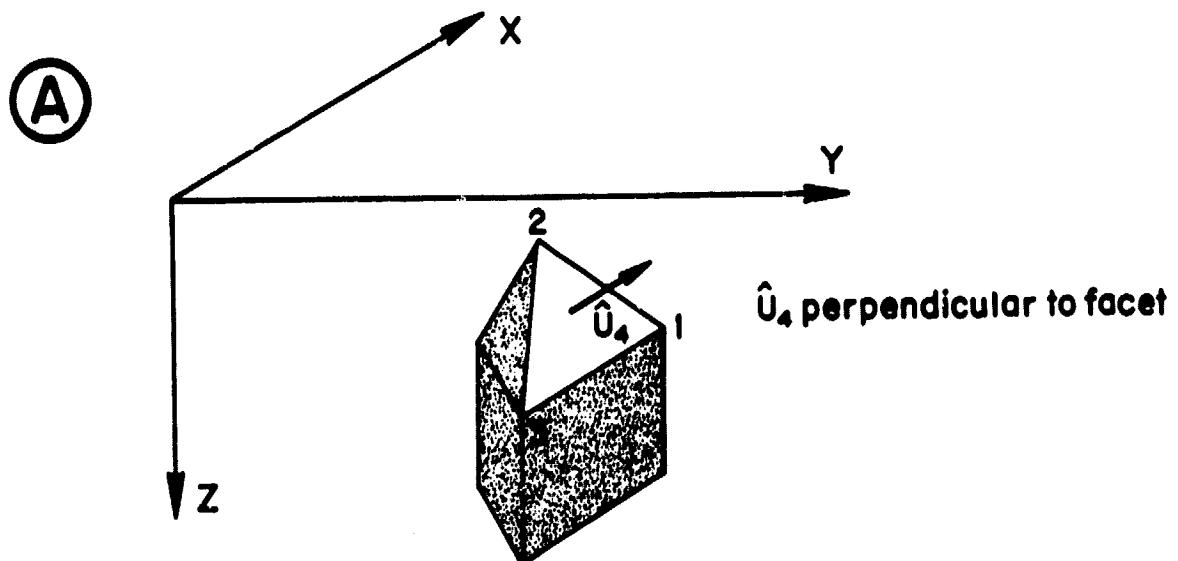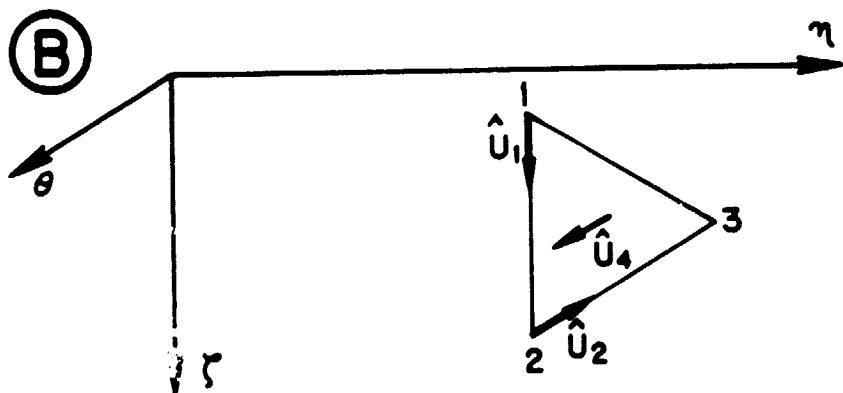
Calculation of geoid anomaly over a three dimensional polyhedron.

Figure 7

92

$$\hat{r} = \frac{(x - x') \, \hat{x} + (y - y') \, \hat{y} + (z - z') \, \hat{z}}{[(x - x')^2 + (y - y')^2 + (z - z')^2]^{\frac{1}{2}}}$$

and ∇ is the vector del operator

We see that it can be changed to a surface integral with the divergence theorem. Thus:

$$N = \frac{G \, \rho}{\gamma} \iint_{s} \frac{1}{2} \, \hat{r} \cdot \hat{u}_4 \, ds \qquad (29)$$

$$\text{or} = \frac{G \, \rho}{\gamma} \iint_{s} \frac{1}{2} \frac{[(x - x') \, u_{41} + (y - y') \, u_{42} + (z - z') \, u_{43}] \, ds}{[(x - x')^2 + (y - y')^2 + (z - z')^2]^{\frac{1}{2}}}$$

where $\hat{u}_4$ is a unit vector normal to the element of surface area ds, and has components (u_{41}, u_{42}, u_{43}).

This equation now is a surface integral and mus: be solved for each individual facet upon which the unit normal vector $\hat{u}_4$ is constant. After this integral is computed for each face, the results are summed for all facets thereby calculating the geoid anomaly due to the entire body. Thus

$$N = \sum_{i} I_i \qquad \text{where } I_i \text{ is equation 29 evaluated for}$$

the ith facet of the polyhedron. (30)

Solution of this integral for each face of the polyhedron requires a coordinate transformation, rotating the facet until it is normal to cne of the new axes. This technique was originally used for solving integrals in gravity and magnetic computations by Barnett (1976) and also Paul ('974).

This coordinate transformation involves a rotation and translation. To construct the necessary rotation matrix, three unit vectors must be first calculated. For a given facet (Figure 7b) these three vectors are determined in the following way. Each vertex in the facet is numbered in counter clockwise order when looking into the body. Unit vector $\hat{u}_1$ extends from point 1 to point

93

2, and unit vector $\hat{u}_2$ extends from point 2 to point 3. Given this numbering

scheme $\hat{u}_1 \times \hat{u}_2$ (vector cross product) is the outward facing normal for the

facet. With these vectors, two additional unit vectors can be calculated

$$\hat{u}_4 = \hat{u}_1 \times \hat{u}_2 \qquad \text{where } \hat{u}_4 \text{ is the}$$

$$\hat{u}_3 = \hat{u}_4 \times \hat{u}_1 \qquad \text{outward unit normal}$$

An orthogonal rotation matrix is constructed from these unit vectors.

$$|u| = \begin{vmatrix} u_{11} & u_{12} & u_{13} \\ u_{31} & u_{32} & u_{33} \\ u_{41} & u_{42} & u_{43} \end{vmatrix}$$

where u_{ij} is the jth component

of the unit vector $\hat{u}_i$.

A coordinate translation is also applied so that the observation point (x', y', z')

becomes located at the new zero origin. The complete coordinate transformation

changes the (x, y, z) coordinates to a new (ζ, η, θ) system, in which

(x', y', z') becomes $(0, 0, 0,)$.

Thus

$$\begin{vmatrix} \zeta \\ \eta \\ \theta \end{vmatrix} = \begin{vmatrix} u_{11} & u_{12} & u_{13} \\ u_{31} & u_{32} & u_{33} \\ u_{41} & u_{42} & u_{43} \end{vmatrix} \begin{vmatrix} x \\ y \\ z \end{vmatrix} - \begin{vmatrix} \zeta' \\ \eta' \\ \theta' \end{vmatrix} \tag{31}$$

where

$$\zeta' = u_{11} x' + u_{12} y' + u_{13} z'$$

$$\eta' = u_{31} x' + u_{32} y' + u_{33} z'$$

$$\theta' = u_{41} x' + u_{42} y' + u_{43} z'$$

After coordinate transformation the integral 29 for the i'th facet changes

to the simpler form:

$$I_i = \frac{G \rho}{\gamma} \iint_s \frac{1}{2} \frac{\theta_i \, d\zeta \, d\eta}{[\zeta^2 + \eta^2 + \theta^2_i]^{\frac{1}{2}}} \tag{32}$$

In order to solve this surface integral for the i'th face, we change it to a line integral over the sides of the polygonal facet via Stokes' theorem.

$$I_i = \frac{G\rho}{\gamma} \oint \frac{\theta_i}{2} \log_e \left\{ \zeta + \left[\zeta^2 + \eta^2 + \theta_i^2 \right]^{\frac{1}{2}} \right\} d\eta \qquad (33)$$

where the integration is counter clockwise (when looking into the body) around the line segments bounding the i'th face of the polyhedron. It must be a closed contour.

Each side of the facet is a line segment with an equation

$$\zeta = m_j \eta + \zeta_j^0 \qquad (34)$$

where m_j is the slope of the j'th line segment

$$m_j = \frac{\zeta_{j+i} - \zeta_j}{\eta_{j+i} - \eta_j}$$

and also $\zeta_j^0 = \zeta_j - m_j \eta_j$

Thus the total integral for the i'th facet is a sum of line integrals over all of the bounding line segments.

$$I_i = \sum_j L^i_{\ j} \qquad (35)$$

and

$$L^i_{\ j} = \frac{G\rho}{\gamma} \int_{\eta_j}^{\eta_{j+1}} \frac{\theta_i}{2} \log_e \left\{ (m_j \eta + \zeta_j^0) + \right. \qquad (36)$$

$$\left. \left[(m_j \eta + \zeta_j^0)^2 + \eta^2 + \theta_i^2 \right]^{\frac{1}{2}} \right\} d\eta$$

and $L^i_{\ j}$ is the line integral for the j'th line segment of the i'th facet of the polyhedron.

This assumes that m_j is finite. If it is not then $d\eta$ is zero and consequently s. s $L^i_{\ j}$. Also if θ_i is zero, then I_i is zero. After integration of equation

95

36 and summation over all line segments of all facets, the final result is obtained. (See appendix).

$$N = \frac{G\rho}{\gamma} \sum_i \frac{\theta_i}{2} \sum_j \left\{ n \log_e \left\{ (m_j n + \zeta_j^0) + \right. \right.$$

(37)

$$\left[(m_j n + \zeta_j^0)^2 + n^2 + \theta_i^2 \right]^{\frac{1}{2}} \right\} + \frac{\zeta_j^0}{[1+m_j^2]^{\frac{1}{2}}} \log_e \left\{ \left[(m_j n + \zeta_j^0)^2 + n^2 + \theta_i^2 \right]^{\frac{1}{2}} \right.$$

$$\left. + n \left[1 + m_j^2 \right]^{\frac{1}{2}} + m_j \zeta_j^0 \right\} + \theta_i \ \mathrm{Tan}^{-1} \left[\frac{(m_j \theta_i^2 - \zeta_j^0 n)}{\theta_i \left[(m_j n + \zeta_j^0)^2 + n^2 + \theta_i^2 \right]} \right] \left. \left. \right\} \right| \begin{smallmatrix} n_{j+1} \\ \\ n_j \end{smallmatrix}$$

This expression then, in conjunction with the coordinate transformation of equation 31, when evaluated, gives the geoid anomaly over an arbitrary polyhedron. As a practical matter, it is difficult to specify the coordinates of the body in the orderly manner required. To simplify matters all faces could be triangles and the body would be assembled in the manner described by Barnett (1976). Also it should be noted that both the two dimensional and three dimensional solutions to geoid anomaly modeling are exact analytic expressions. This is in contrast to the asymptotic expansion technique for geoid anomaly modeling developed by Ockendon and Turcotte (1977), which although easier to evaluate requires the body to be very thin. Another modeling technique was utilized in a study of a seamount region by Fisher (1976). In many studies of geoid anomalies it will be necessary to compute the resultant anomaly on a spherical earth. The three dimensional method developed here can be utilized for that purpose, as long as it is realized that the connecting segments between points on the polygon are linear. An alternative approach would be to utilize the method developed by Johnson and Litehiser (1972), who give an expression for the potential due to a body on a spherical earth.

96

Their method in combination with Brun's formula would be a good numerical solution to geoid modeling on a spherical earth. Another numerical technique for computing geoid anomalies on a spherical earth was developed and applied in a study by Bowin et. al. (1975).

As a geophysical example, this three dimensional modeling technique is utilized to study a geoid anomaly which has been observed above the Truk Islands (part of the Caroline Islands in the western Pacific). This geoid anomaly is 5 meters in amplitude and is above a seamount which is 4 km high. Quite simply this geoid high can be explained as due to the excess mass of the seamount itself, and the deficit mass of its compensating body. To model this anomaly the topography was digitized and a polyhedral body was constructed. In addition a polyhedral compensating mass was calculated. An Airy type crust with a compensation depth of 30 km was utilized. In Figure 8 a cross section of this model is depicted, along with both the calculated and observed geoid height. From the good agreement of the two, it can be said that this geoid anomaly is explained by an isostatic model of this seamount.
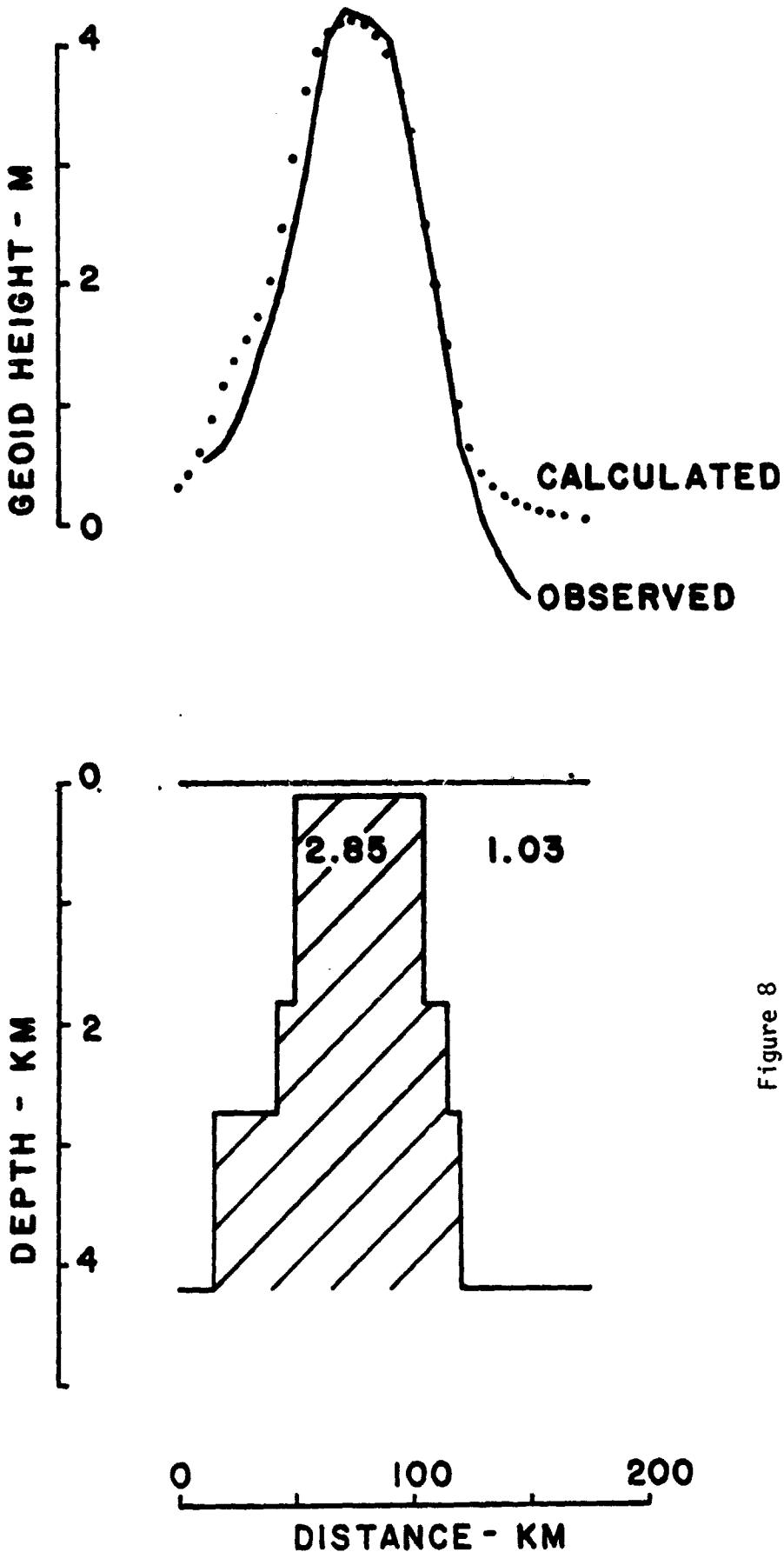
Figure 8

Geoid anomaly over the Turk Islands in the Western Pacific. Left end of GEOS-3 profile is at 151.3°E, 6.85°N, right end is at 152.0°E, 8°N. Geoid height is referred to an ellipsoid with flattening 1/298.255 and arbitrary semi-major axis. A simple three component model was used with a density of 1.03 gm/cm3 for water, 2.85 gm/cm3 for crust, and 3.3 gm/cm3 for mantle. The body was a ployhedron, a cross section of this body is shown. This model was in Airy isostatic equilibrium with a crustal thickness of 4 km sediment and 6 km basement.

Techniques in the Frequency Domain

A different understanding of the geoid is possible in the wavenumber domain. This is done by examining the relationship between the Fourier transform of gravity and the Fourier transform of the geoid. In other words, what is the transfer function between gravity and the geoid? Our derivation is analagous to the derivation of formula 21, but is done in the frequency domain.

Given the vertical component of gravity due to a two dimensional body we go to the wavenumber domain via the Fourier transform.

$$\mathcal{F}(F_g^V) = \int_{-\infty}^{+\infty} F_g^V (y) \, e^{-iky} \, dy \qquad (38)$$

To obtain the Fourier transform of the horizontal component of gravity we Hilbert transform $\mathcal{F}(F_g^V)$

$$\mathcal{F}(F_g^H) = \mathcal{F}(F_g^V) \cdot i \cdot \text{sgn}(k) \qquad (39)$$

where multiplication by $i\,\text{sgn}(k)$ is the Hilbert transformation (Papoulis, 1962)

also $\text{sgn}(k) = +1 \quad k > 0 \qquad$ and $\; i = [-1]^{\frac{1}{2}}$
$$-1 \quad k < 0$$

This procedure can be verified by comparing the Fourier transforms of the vertical and horizontal components of gravity due to an infinite mass line. After division by normal gravity we get the Fourier transform of the deflection of the vertical.

$$\mathcal{F}(\delta) = \frac{\mathcal{F}(F_g^H)}{\gamma} = \frac{\mathcal{F}(F_g^V) \cdot i \, \text{sgn}(k)}{\gamma} \qquad (40)$$

Utilizing the integration theorem in the frequency domain the Fourier transform of the geoid is obtained. This is because the geoid is the integral of deflection

of the vertical.

$$\mathcal{F}(N) = \mathcal{F}(F_g^v) \cdot \frac{i \ sgn \ (k)}{i \ \gamma \ k} \tag{41}$$

or

$$\mathcal{F}[N(y)] = \frac{1}{\gamma \ |k|} \ \mathcal{F}[F_g^v \ (y)]$$

Thus given the Fourier transform of gravity we multiply by a transfer function S(k) to obtain the Fourier transform of the geoid. For the two dimensional case:

$$S(k) = \frac{1}{\gamma \ |k|} \tag{42}$$

This transfer function shows that a geoid anomaly over a body will have the same phase spectra as the gravity anomaly. In simpler words this is our previous observation. A geoid anomaly over a body has the same general shape. Any maximum in the geoid occurs exactly where a gravity maximum does. However the geoid anomaly for a given wavelength is changed in amplitude by the factor ($1/|k|$). Thus for long wavelengths (k<<1) the geoid anomaly will be magnified, while at short wavelengths (k>>1) diminished. This is our observation that geoid anomalies are "wider".

Conclusions

In this paper we have been concerned with developing the techniques necessary for the interpretation of geoid anomalies. These are mathematical formulas which for a given geological model can be utilized to compute the resultant geoid anomaly. If the model is considered two dimensional then densities for a polygon in two dimensions are specified and using formulas 24 and 25 the geoid heights are calculated. In this method only the relative heights are important. Any geologic body can be modeled with a polyhedral shape in three dimensions. If density is variable within the body several polyhedra may be utilized. After specifying densities for this, formula 37 is utilized to calculate the resultant geoid anomaly. To understand geoid anomalies, it is seen that they basically have the same shape as gravity anomalies, but with the long wavelength components amplified. Techniques such as these are only tools. Their real importance is in enabling the interpretation of observed geoid anomalies, such as are detected by GEOS-3.

CHAPTER III ACKNOWLEDGMENTS:

References

Barnett, C.T., 1976. Theoretical modeling of the magnetic and gravitational fields of an arbitrary shaped three-dimensional body, Geophysics, 41, 1353-1364.

Bowin, C., B. Simon, and W.R. Wollenhaupt, 1975. Mascons: A Two-Body Solution, J. Geophys. Res., 80, 4947-4955.

Coggon, J.H., 1976. Magnetic and gravity anomalies of polyhedron, Geoexploration, 14, 93-105.

Fischer, I., 1976. Deflections and Geoidal Heights Across a Seamount, Int. Hydro. Rev., LIII, 117-128.

Heiskanen, W.A. and H. Moritz, 1967. Physical Geodesy, W.H. Freeman & Co., San Francisco.

Johnson, L.R. and J.J. Litehiser, 1972. A method for computing the gravitational attraction of three-dimensional bodies in a spherical or ellipsoidal earth, J. Geophys. Res., 77, 6999-7009.

Ockendon, J.R. and D.L. Turcotte, 1977. On the gravitational potential and field anomalies due to thin mass layers, Geophys. J. R. astr. Soc., 48, 479-492.

Papoulis, A., 1962. The Fourier integral and its applications, McGraw-Hill Book Co., New York.

Paul, M.K., 1974. The gravity effect of a homogeneous polyhedron for three-dimensional interpretation, Pure and Appl. Geophys., 112, 553-561.

Talwani, M., J. Worzel and M. Landisman, 1959. Rapid gravity computations for two-dimensional bodies with application to the Mendocino submarine fracture zone, J. Geophys. Res., 64, 49-59.

Talwani, M., H. Poppe and P.D. Rabinowitz, 1972. Gravimetrically determined geoid in the western North Atlantic, in "Sea surface topography from space", NOAA technical report, ERL-228-AOML. 7-2, 2, 1-34.

Chapter IV

Geoid Anomalies Over Oceanic Features

Geoid Anomalies over Oceanic Features

In using satellite altimeter measurements to study the Earth's interior a simple question can be asked. What is the shape of the ocean surface over bathymetric features? Physically such features would be expected to have related geoid anomalies because there is a large density contrast between oceanic crust and the surrounding water. At the bottom of the ocean floor there are certain types of large structures; seamounts, continental margins, fracture zones, mid-ocean ridges, and deep sea trenches. Over each one of these features there are characteristic undulations of the ocean surface. Being directly related to the density structure, these measured shapes can be utilized to infer the internal lateral density variations within the Earth. Using the GEOS-3 radar altimeter geoid anomalies have been identified over these structures.

Bordering the continents in the Atlantic ocean are passive continental margins. Detailed geophysical studies of these regions usually involve the study of several important questions; location of the ocean-continent boundary, nature of the mechanism of isostasy, and history of subsidence along the margin. Of these questions, geoid measurements may be of assistance with the first two. As an example of a passive margin consider the East Coast United States. Across this margin the geoid has a 6 meter step similar in sense to bottom topography (Figure 1). In places this anomaly is quite distinct, as off Nova Scotia; further south the increase is quite gradual. An important area of research would be to ascertain why this shape varies along the coast. This study would probably be concerned with isostatic geoid anomalies.
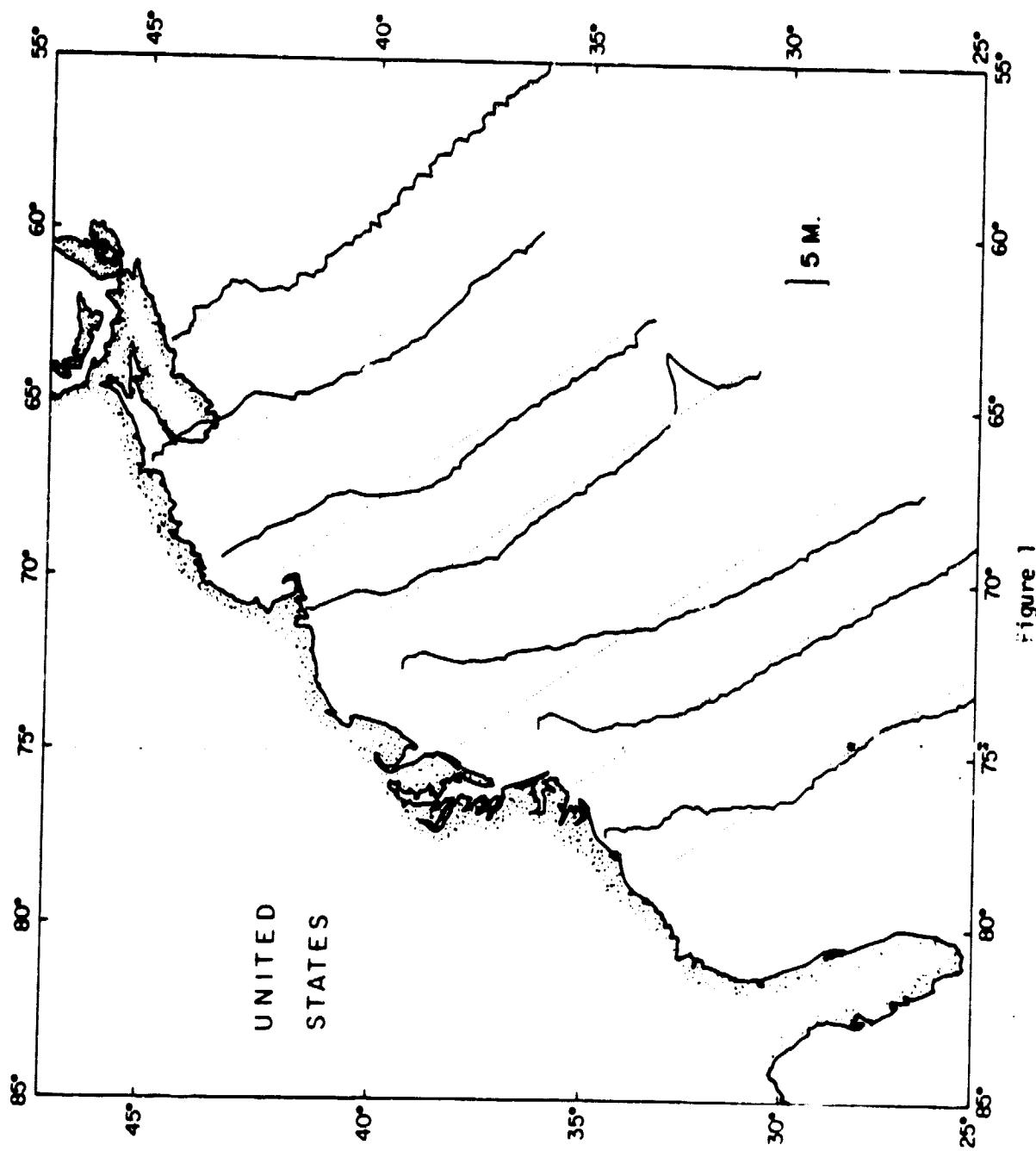
Geoid measurements at the Eastern United States margin are plotted
perpendicular to the track, the tracks are dotted lines and the
data solid lines.

106

At many of the continental margins in the Pacific Ocean active subduction of the lithosphere occurs at deep sea trenches. These are active continental margins. At these margins there is a characteristic geoid anomaly. With GEOS-3 data we see that above the trench axis the ocean surface forms deep valleys up to -20 m in amplitude. Over the Aleutian Trench the sea surface has a depression of -13 m, while at the Mariana trench the geoid dips by almost -20 m (Figure 2). Seaward of the Aleutian Trench there is a long wavelength increase in the geoid towards the Aleutians. This anomaly is concave downward and continues to increase landward of the trench where the depths are shallower. Because it is the nature of the geoid to show long wavelength anomalies it is expected to be most sensitive to deep density inhomogeneities rather than crustal structures. As the downgoing slab is a large and deep inhomogeneity, any anomaly caused by it would be more evident in the geoid rather than in gravity.

Another primary type of geoid anomaly is above mid-ocean ridges where accretion of the lithosphere occurs. One example of this type anomaly is across the Southwest Indian Ridge in Figure 3. Gravity and topography profiles are from a nearby ship track; the geoid data are from the GEOS-3 satellite. Although gravity data show little of a long wavelength anomaly, the geoid has a distinct anomaly centered over the ridge axis. This is about 7 meters in amplitude and at least 1000 km wide. A track chart of altimeter data acquired over both the Southwest Indian and Southeast Indian Ridge is illustrated in Figure 4. Other geoid profiles across the Southwest Indian Ridge are shown in Figure 5. Each of these six profiles shows a higher region to the southeast of the ridge axis followed by a sudden change in slope directly at the axis. As there appears to be a broad regional slope to the data a linear trend has been removed from each profile.

ALEUTIAN TRENCH MARIANA TRENCH
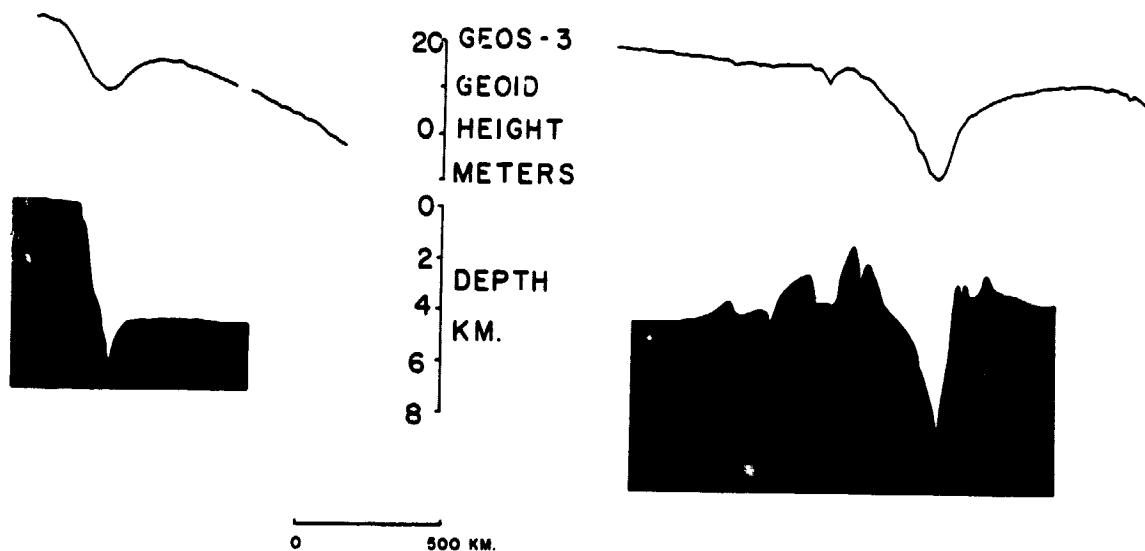
BISMARCK SEA
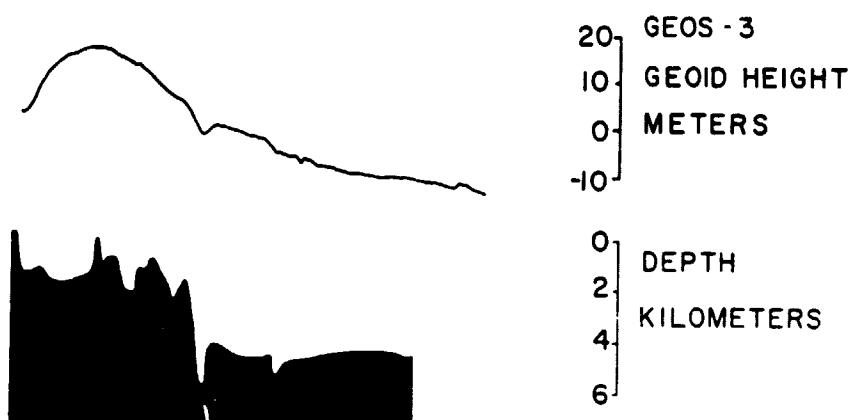
Figure 2
Geoid profiles over trenches and a marginal sea.

108
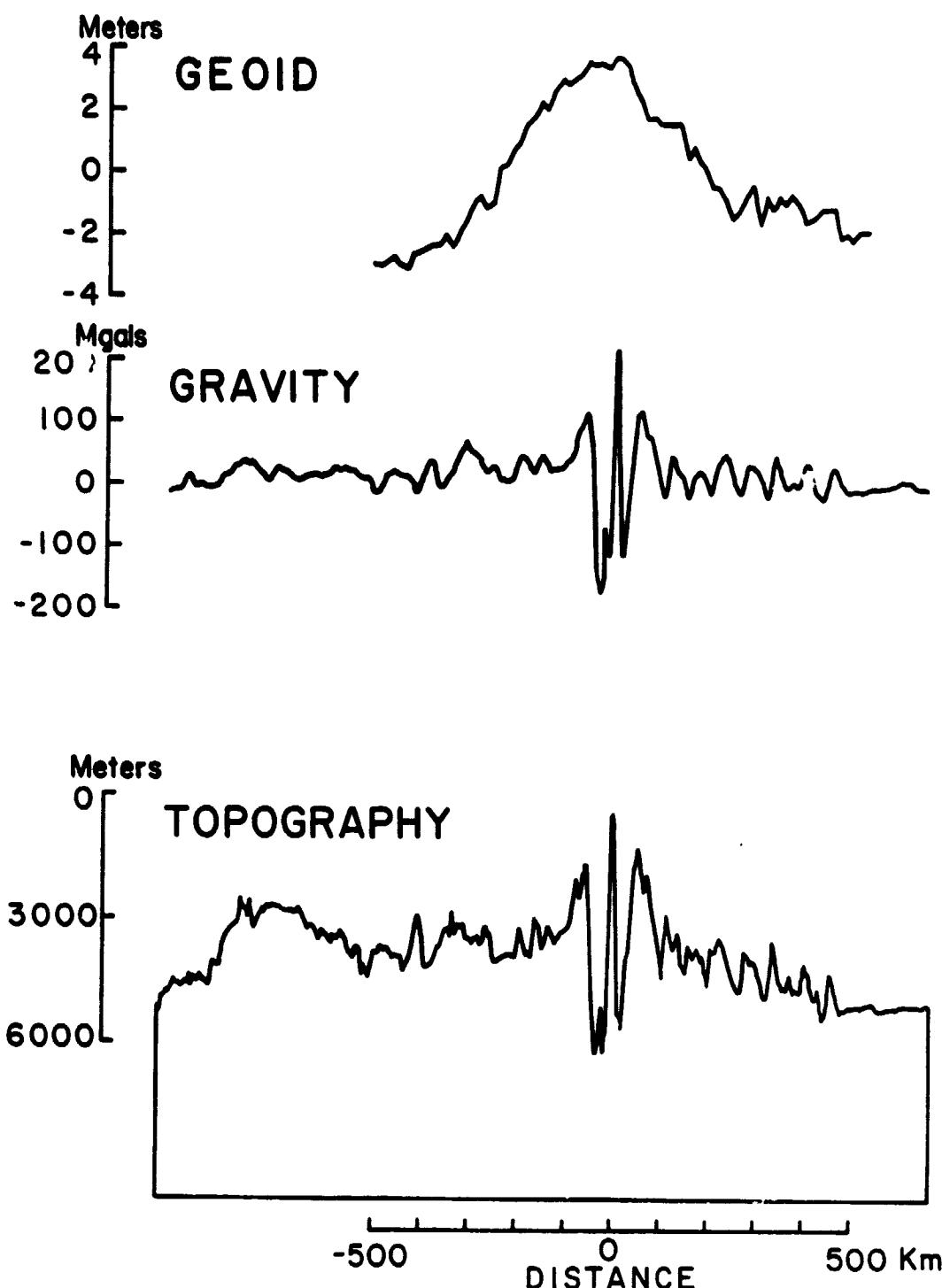
Figure 3

Profiles over the Southwest Indian Ridge.
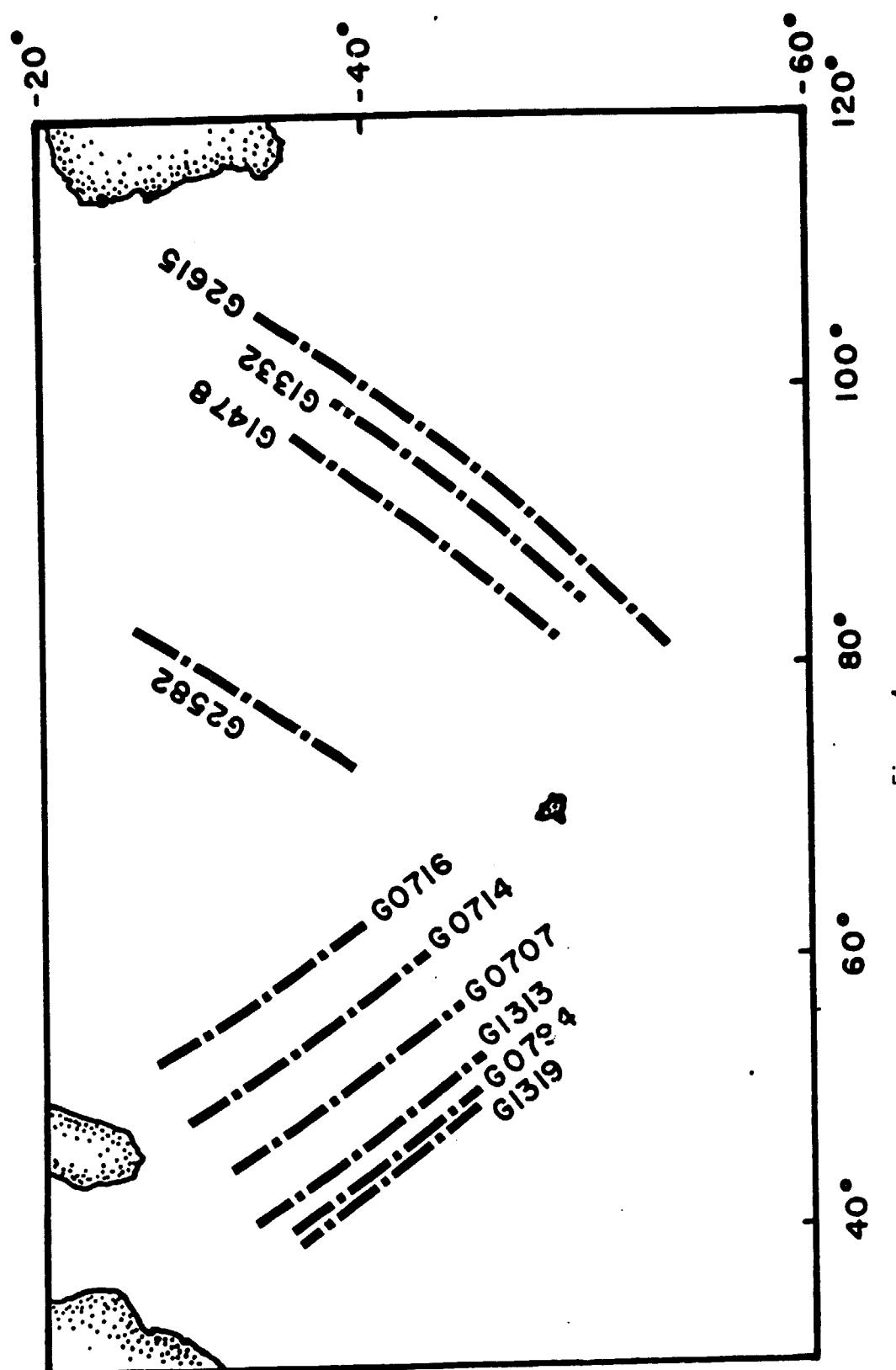
Location of GEOS-3 data across the Southwest and Southeast Indian Ridge.

Figure 4

110
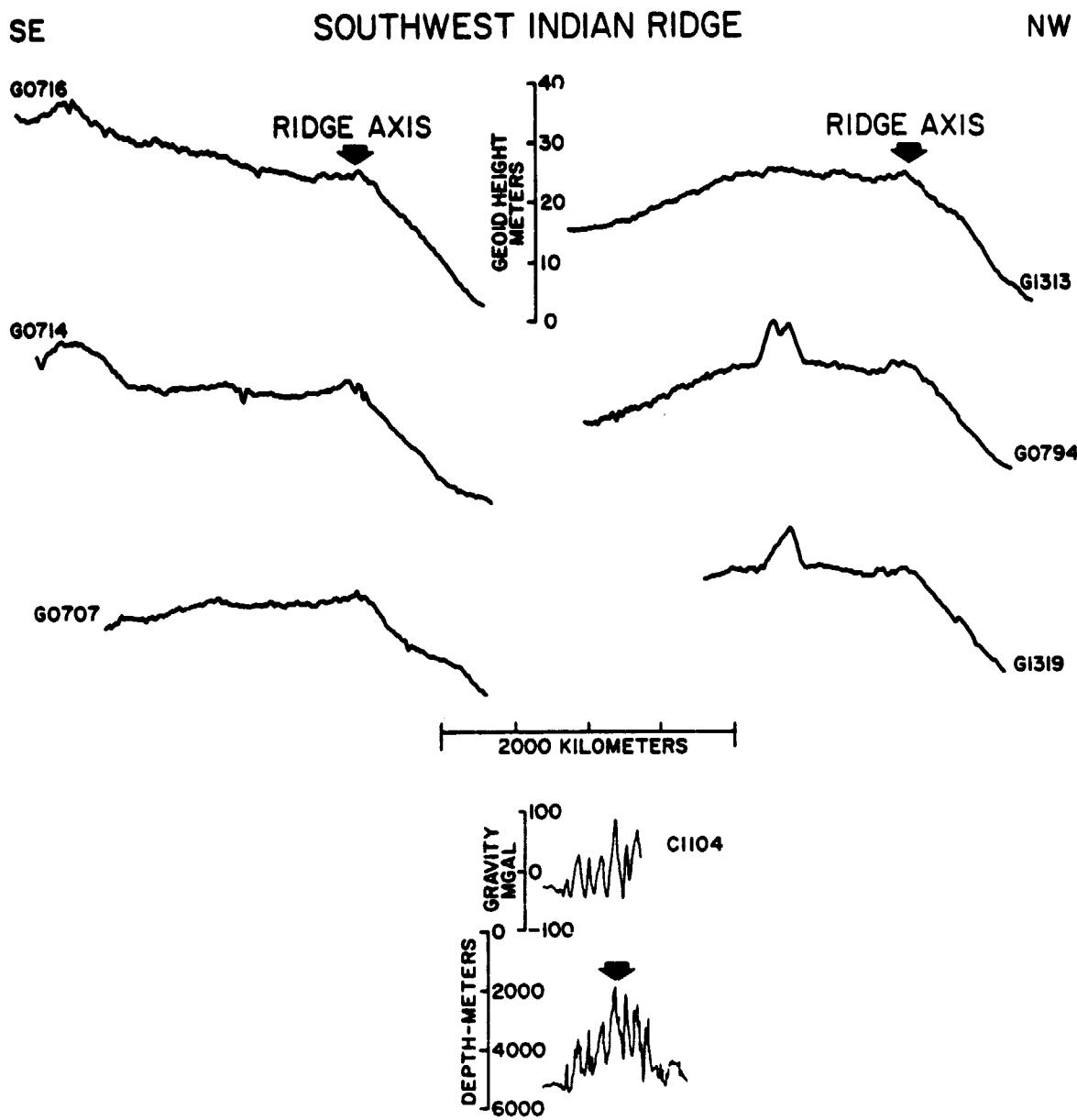
Figure 5

Geoid profiles across the Southwest Indian Ridge. Bathymetry

and gravity profiles from Conrad cruise 11-04 are also shown.

These profiles are in Figure 6. Each profile over the Southwest Indian Ridge after removal of a linear trend shows a characteristic geoid anomaly similar to the one in Figure 4. This anomaly is maximum at the ridge axis and almost 10 m in amplitude. It is 1800 km wide. Profiles across the Southeast Indian Ridge show a much larger regional background as shown in Figure 7. After removal of a linear trend the characteristic ridge anomaly is evident in Figure 8. This anomaly has a 6 meter amplitude and 2000 km width. Presumably this ridge anomaly is the result of density anomalies due to creation and evolution of the lithosphere. A detailed study of this and other ridge anomalies should be undertaken to ascertain any dependence upon spreading rate and any possible asymmetry. Using a thermal model of the lithosphere, Haxby and Turcotte (1978) have modeled the ridge anomaly in the North Atlantic.

Other smaller oceanic structures have shorter wavelength geoid anomalies. Above islands there is a geoid anomaly several meters high. For example 6 meters over Bermuda (Figure 1) and 4 meters over the Caroline Islands (Figure 9). At fracture zones where the crust has a significant age difference on either side there will be a difference in depth which causes a geoid anomaly. Over the Romanche Fracture Zone the geoid has a step of 4 or 5 meters (Figure 10). With similar large fracture zones it will be possible to use geoid height measurements to trace fracture zones where ship measurements are scarce. Another type geoid anomaly occurs over the Bismarck Sea. This is a small marginal basin several kilometers shallower than adjacent ocean. Above this region the ocean surface forms a broad high, 450 km wide and 7 m high (Figure 2).
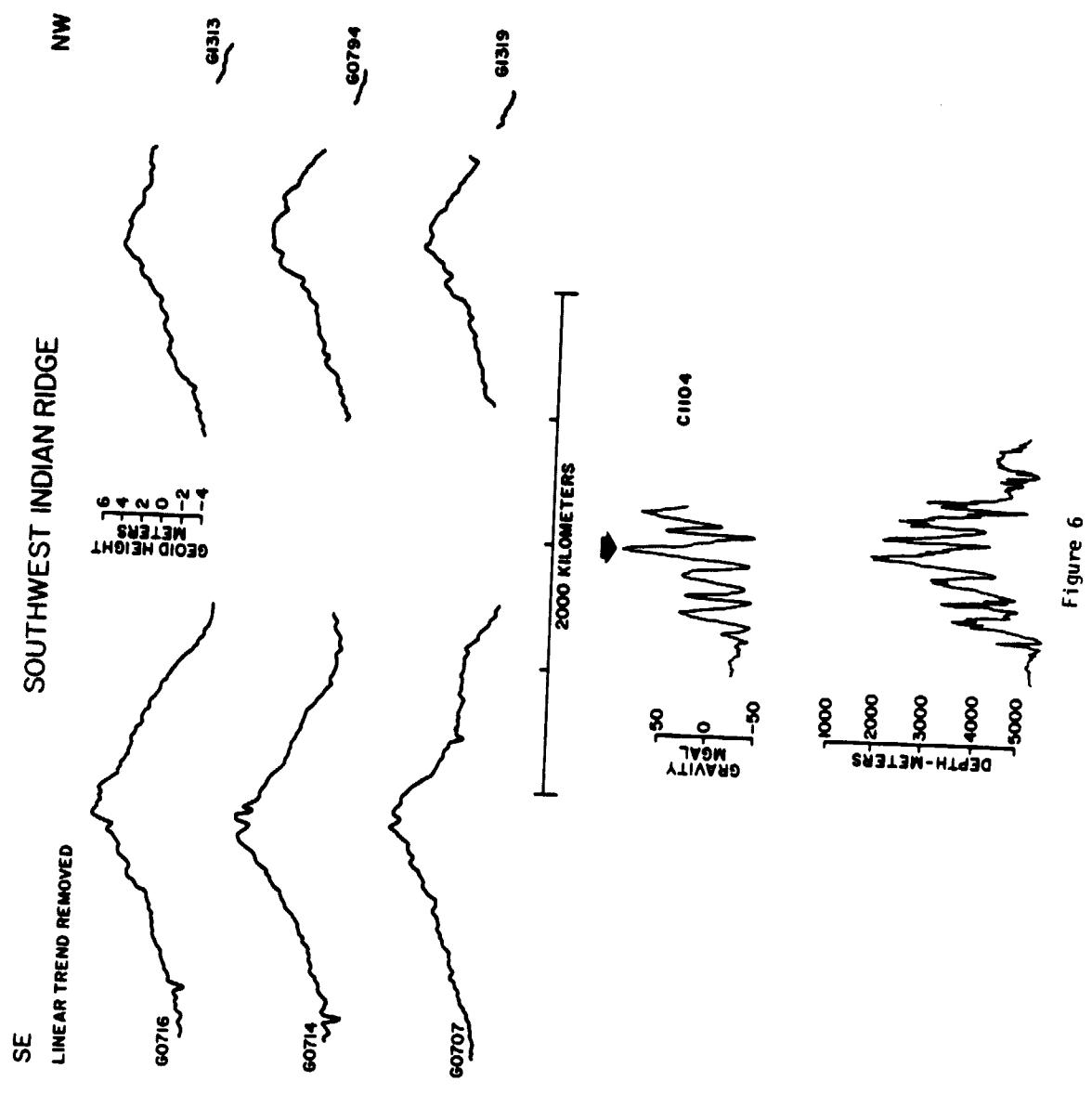
Geoid profiles across the Southwest Indian Ridge with a linear trend removed.

113
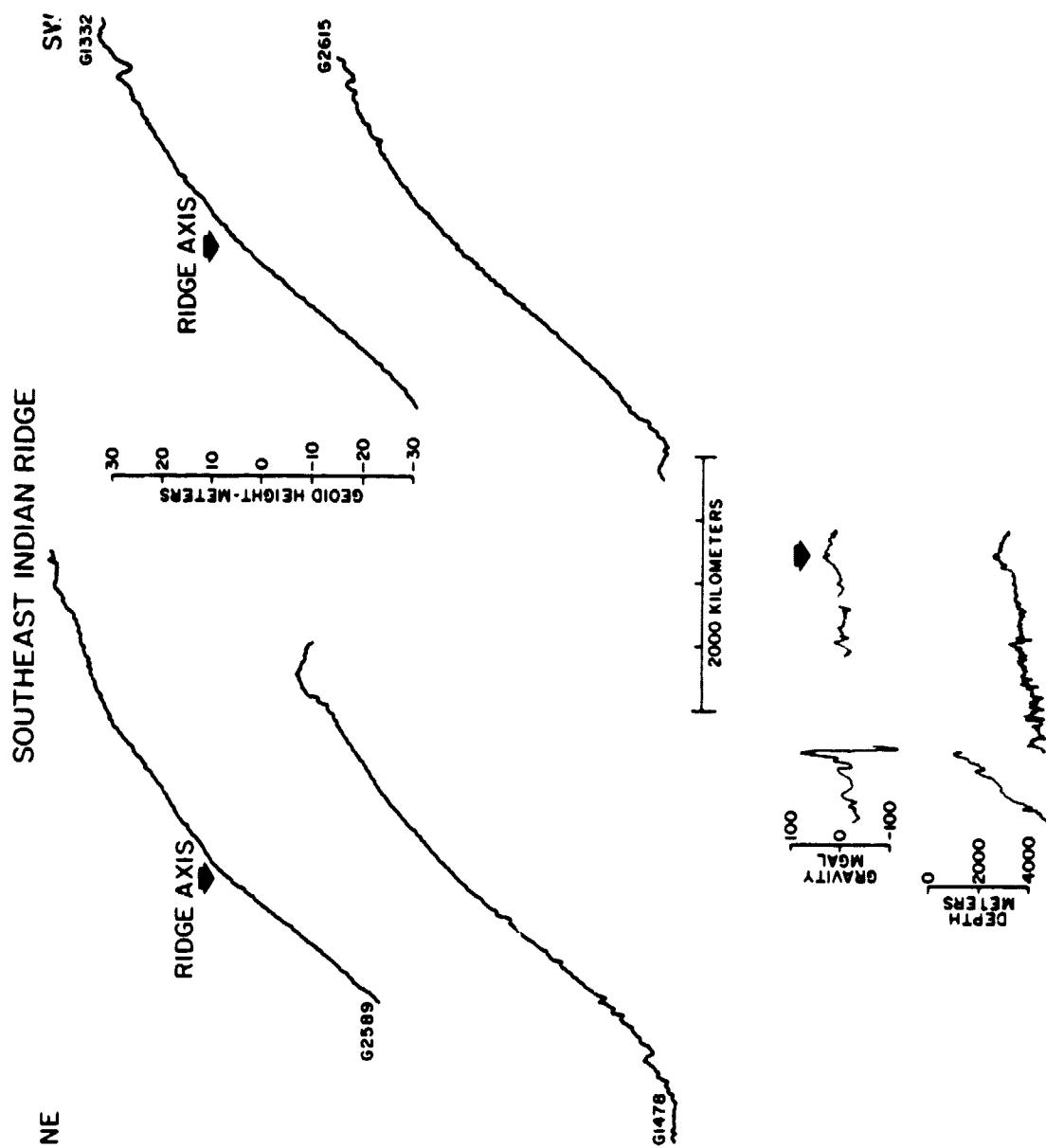
Geoid profiles across the Southeast Indian Ridge. Bathymetry
and gravity profiles from Conrad cruise 11-05 are also shown.

114

SOUTHEAST INDIAN RIDGE

NE · SW

LINEAR TREND REMOVED

GEOID HEIGHT METERS

4
2
0
-2
-4

G2589

G1478

G1332

G2615

|← 2000 KILOMETERS →|

GRAVITY MGAL

50
0
-50

C1105

DEPTH-METERS

0
1000
2000
3000
4000
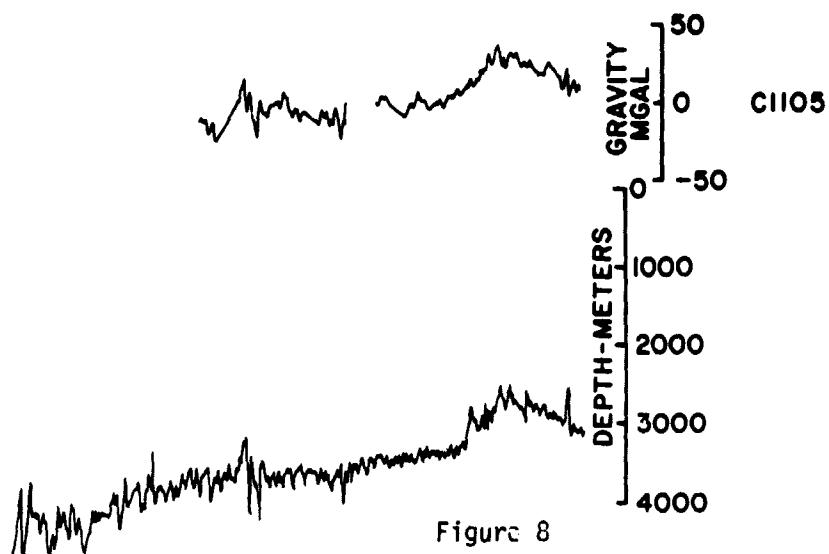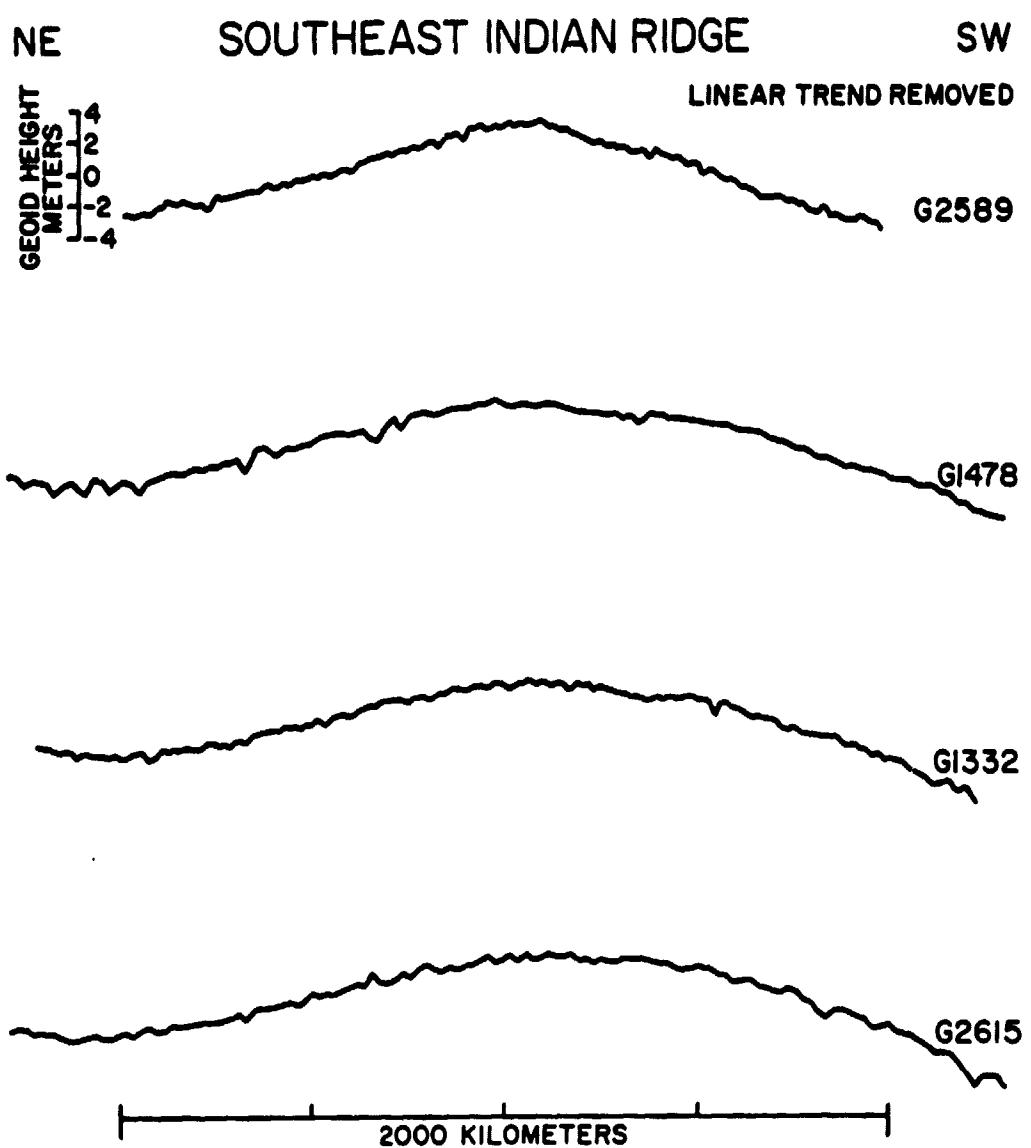
Figure 8

Geoid profiles across the Southeast Indian Ridge with a linear trend removed.

CAROLINE ISLANDS

Caroline Islands geoid anomaly. This anomaly over the islands is 3 or 4 m in amplitude, also there is a step in geoid height of 7 m across the islands.

GEOS-3 HEIGHT METERS

DEPTH KM

0   500 KM.
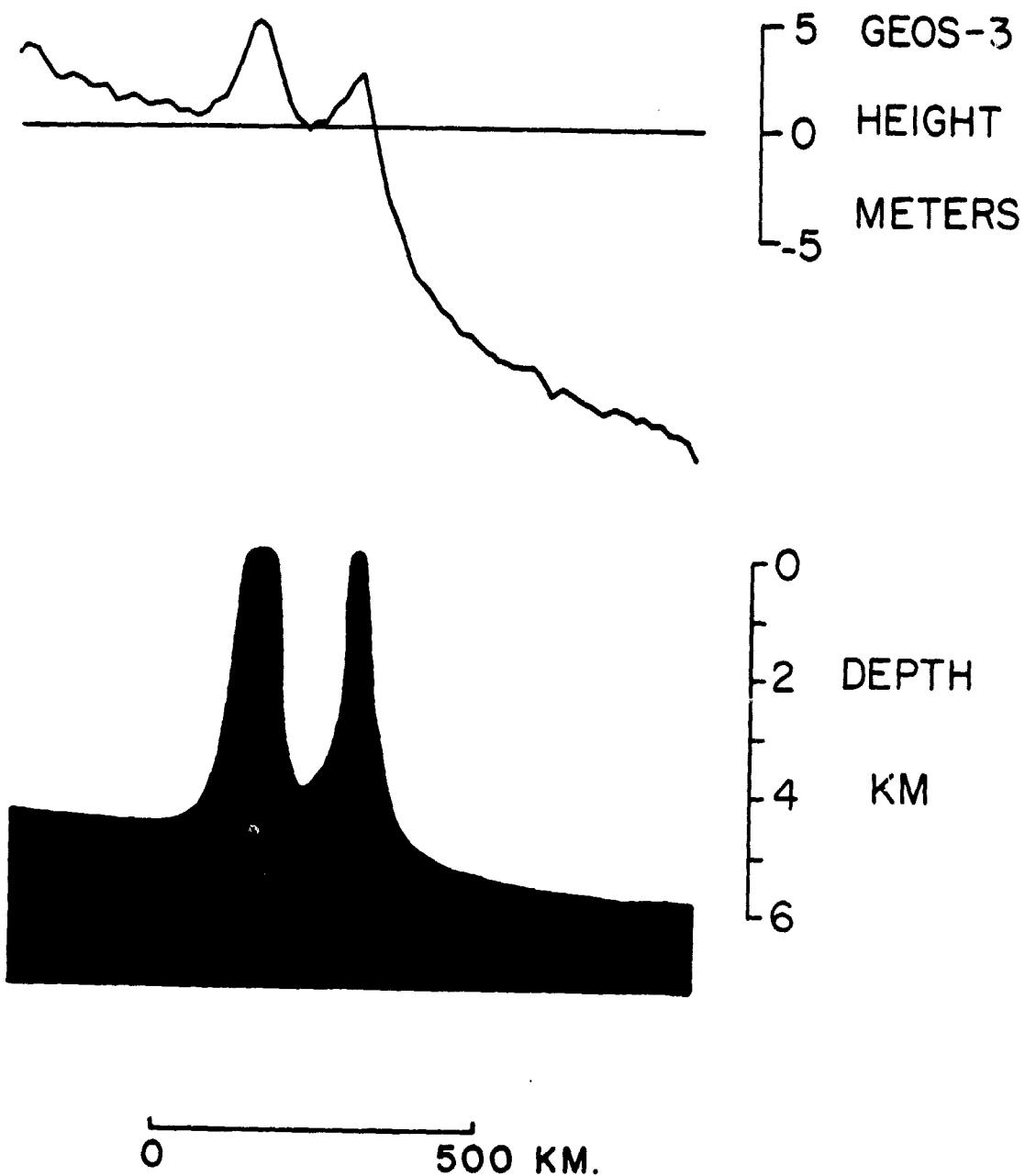
Figure 9
116

ROMANCHE FRACTURE ZONE

GEOS-3
GEOID HEIGHT
METERS

DEPTH
KM.
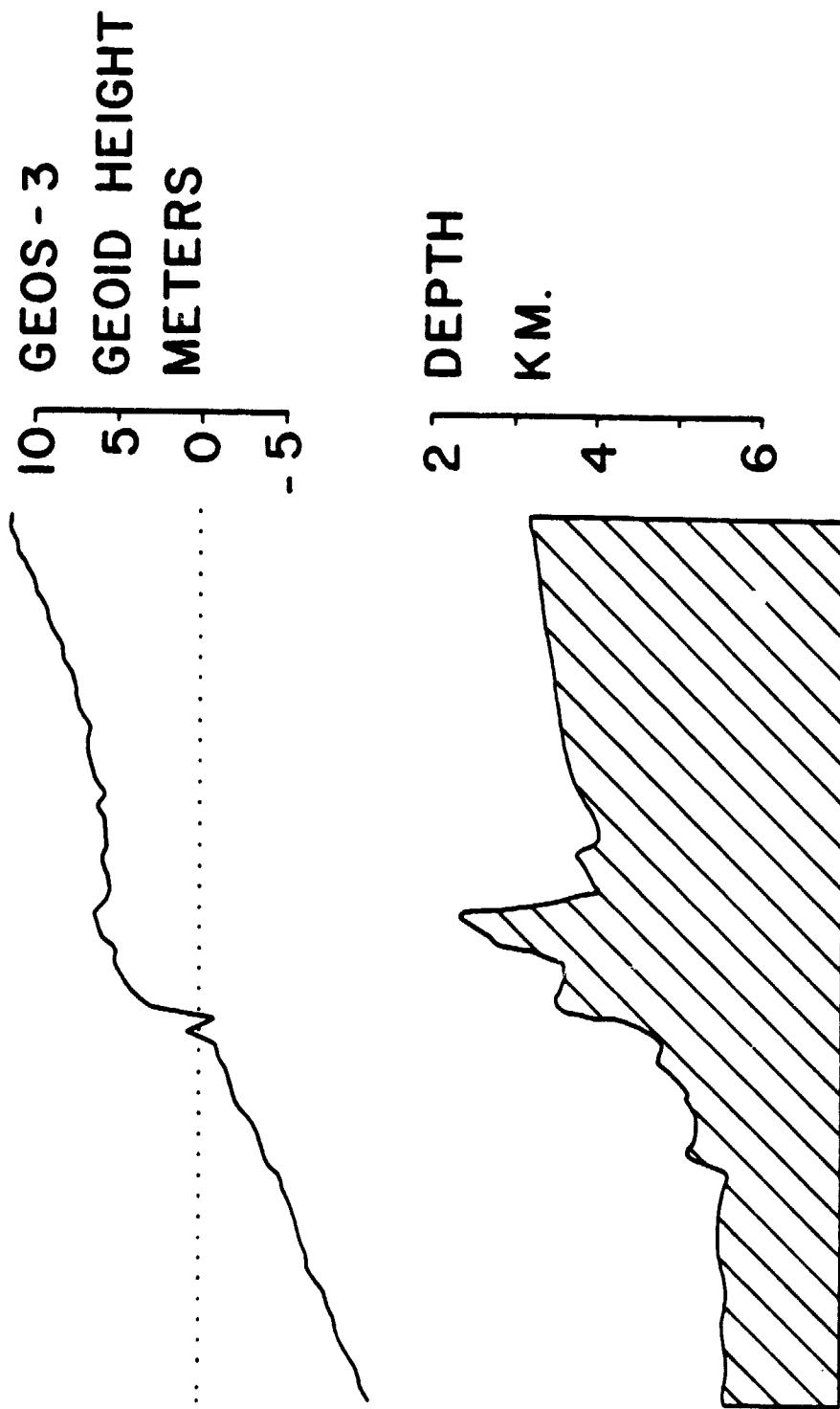
Figure 10

Romanche Fracture Zone. There is an increase in geoid height
of 4 or 5 m from southwest to northeast.

CHAPTER IV ACKNOWLEDGMENTS:

References

Haxby, W.F. and D.L. Turcotte, On isostatic geoid anomalies, J. Geophys. Res., 83, 5473-5478, 1978.

Chapter V

Geoid Corrections in Marine Gravimetry

Introduction

Due to undulations of the geoid free-air gravity anomalies measured at sea are caused both by lateral changes in mass distribution and also by changes in height above or below the reference ellipsoid. In those gravity modeling studies which do not consider the latter effect of height changes, there may sometimes be serious misinterpretation. The required correction term to eliminate this effect is at most ±27 mgal and most significant when studying the geophysical implications of the long wavelength gravitational field.

To understand the need for this correction, consider the standard procedure in gravity modeling; a density model of the anomalous mass is used to calculate the vertical component of gravitational attraction which is then compared with the free-air gravity anomaly. This procedure implicitly assumes the equivalence between free-air gravity anomalies and the gravitational attraction (in the vertical direction) of the anomalous mass. This assumption is only an approximation; due to geoid undulations there can be substantial errors in this procedure. This approximation is well known to geodesists (Bomford, 1962) but is not commonly acknowledged in geophysical studies.

For models of localized mass anomalies or short wavelength features this approximation is probably valid. For regional studies, however, with the objective of interpreting longer wavelength components of the gravity field the importance of correcting the free-air gravity anomaly for geoidal undulations is greatly increased.

For example, in a study of the North Atlantic regional gravity field the effect of this approximation was not discussed by Cochran and Talwani (1978). In this work there would have been a correction term of up to

approximately 20 mgal added to their observed free-air gravity prior to interpretation. Other studies in the Japan sea and Izu-Bonin region (Segawa and Tomoda, 1976) and the Aleutian arc (Grow, 1973) have similarly not considered this additional correction. A modeling study of mid-ocean ridges (Lambeck, 1972) was one of very few to include this indirect effect in the theoretical calculations. Due to the extensive neglect of this effect in geophysical studies we briefly discuss its origin and then indicate the types of physical situations in which it is most significant.

Origin of Error

When measurements of gravity are made aboard ship at sea they are of course actually being made on the surface of the geoid. In some cases, in order to properly utilize this data for geophysical interpretation, it is necessary to correct for the undulations of the geoid surface. Consider the standard method for obtaining the gravity anomaly. After measurement of gravity on the geoid, the normal gravity on the ellipsoid is subtracted thus yielding the gravity anomaly.

$$\Delta g = g_{obs} - \gamma_n$$
where Δg is free-air gravity anomaly

g_{obs} is measured gravity on the geoid

γ_n is gravitational attraction of the ellipsoid, on the surface of that ellipsoid

It is important to note that for determining the free-air gravity anomaly, these two gravitational attractions are measured with respect to <u>different</u> <u>references</u>. The geoid is the reference for the observed gravity and the ellipsoid the reference for theoretical gravity. The difference in height between the ellipsoid and geoid (Figure 1) contributes to the difference in gravitational attraction between what is measured (g_{obs}) and what is calculated (γ_n), and thus the resulting gravity anomaly is not solely due to an anomalous mass. To see the need for this additional correction consider the following
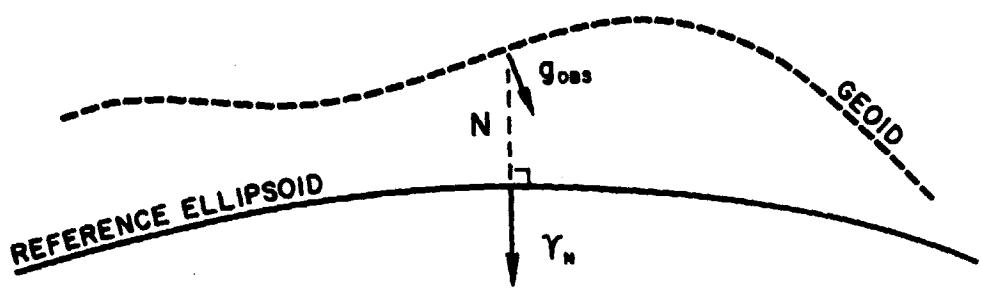
Figure 1

Measurements of gravity (g_{obs}) are made on the geoid which is at a height N above the reference ellipsoid. Attraction of the ellipsoid (γ_n) is calculated at a different height, on the surface of that ellipsoid. This height difference is the reason for the geoid correction term.

123

expression which simply equates forces of gravitational attraction:

$$\Delta g = g_{obs} - \gamma_n = \frac{\partial \gamma_n}{\partial r}.N + \text{gravitational effect of mass between geoid}$$

and ellipsoid + gravitational effect of anomalous mass

where $\frac{\partial \gamma_n}{\partial r}$ is radial gradient of normal gravity

N   is height of the geoid above the

reference ellipsoid - in meters.

On the right side of this equation the first term is a free-air correction, and the second term a Bouguer correction. The free-air term is -.3086 mgal/ meter and using a planar approximation the Bouguer correction is +.043 mgal/meter assuming a water density of 1.03 gm/cm^3. Correction for the Bouguer term subtracts the effect of excess water mass for positive geoid height and adds in a gravitational effect of the missing water mass for negative geoid height. Thus to obtain the gravitational effect of the anomalous mass:

gravitational effect of anomalous mass (in mgal) = Δg + .2656*N

This equation is obtained by transferring the free-air and Bouguer terms to the other side of the previous equation. The term which is added to the gravity anomaly can be designated the geoid correction term. This term is numerically equal to .2656*N. This geoid correction term is added to the free-air anomaly (Δg) in order to obtain the gravitational attraction of anomalous mass - in mgal.

Significance of Correction

This correction will be at most ±27 mgal, corresponding to the fact that geoid height (N) is rarely above or below 100 meters. To consider the importance of this correction it is necessary to understand the properties

124

of the geoid. Undulations of this surface are very smooth, with very long wavelengths. For many regions the corresponding geoid correction will only appear as a constant offset in the data, which in gravity studies is not always important. However, when considering the long wavelength gravitational field (wavelengths longer than approximately 500 km) this correction becomes of greater significance in geophysical studies. At the present time, scientists are beginning to investigate the long wavelength components of the gravitational field, and it is in these studies that the geoid correction in marine gravity must be considered.

To give an example of how this correction might be applied, we consider a profile of gravity across the Tonga-Kermadec trench (Figure 2). Above the bathymetry profile, the gravity anomaly (Δg) referred to the geoid is shown. Utilizing es. nates of geoid height from the GEOS-3 satellite we have also illustrated the geoid height along track.

As the geoic _orrection term is .2656*N it is directly proportional to geoid height (N). Thus the scale on the top left of Figure 2 is for geoid height (N) while the scale on the top right is for the geoid correction term which is a value in mgal to be added to the free-air anomaly (Δg). After addition of this correction to the gravity anomaly, the gravity referred to the ellipsoid is obtained and illustrated in the same figure. In this case the correction is at most 18 mgals. For this region we must affirm the existence of a regional gravity high behind the island arc. This is an important conclusion and directly shows the application of the geoid correction term.

For the purposes of relatively short wavelength gravity modeling this correction may not be very significant while, for more regional studies, failure to take the geoid effect into account may lead to considerable

125

GEOS-3

EL 29

Ship profile across the Tonga-Kermadec trench, from Eltanin 29. Left end of profile is located at 28°S, 172°E; right portion of profile ends at 28°S, 140°W. Profile was projected at an azimuth of 116°.

Figure 2

126
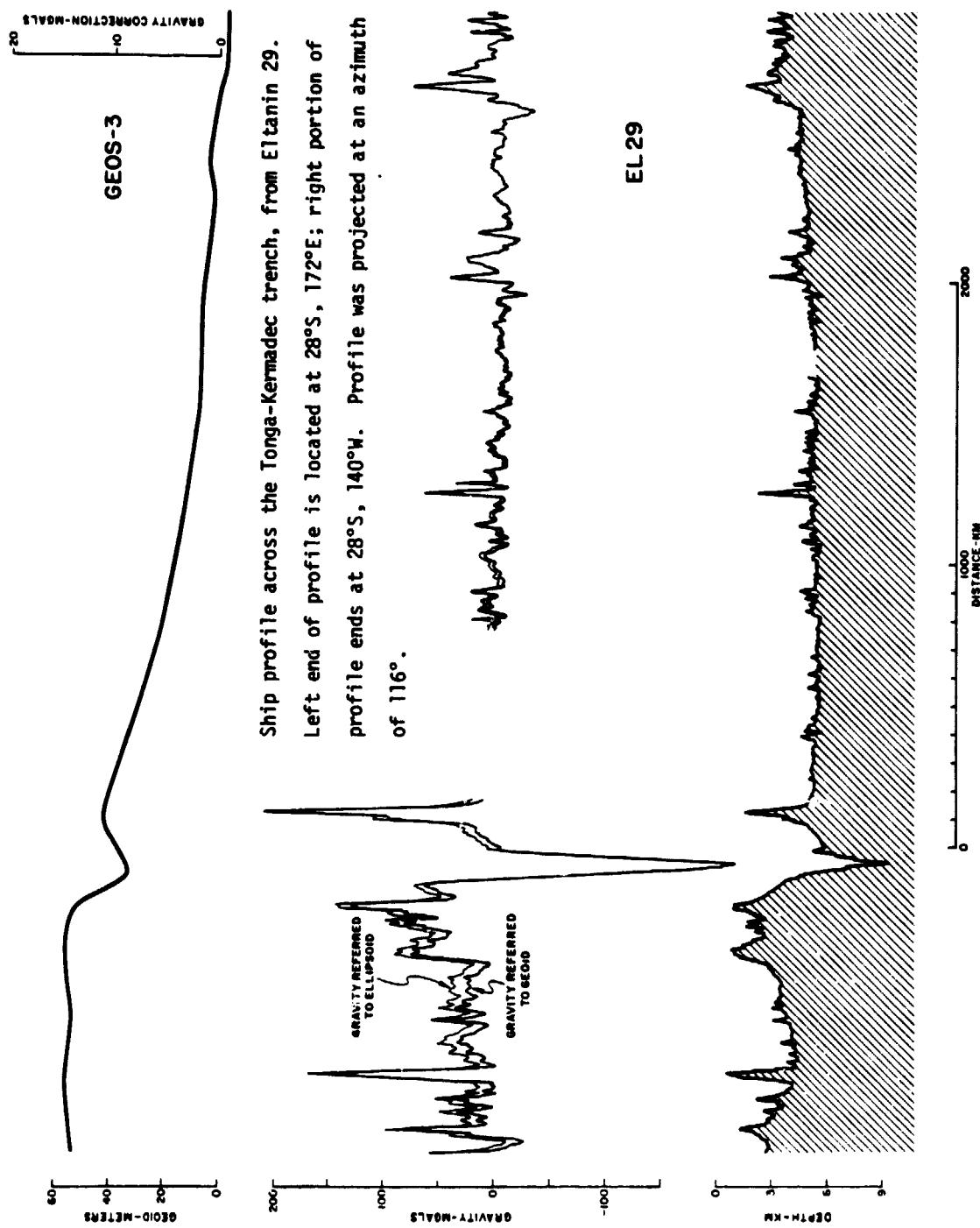
misinterpretation. The importance of considering the geoid height correction for measured gravity is further emphasized as a better definition of the structure of the earth's crustal layers leads to efforts to determine the nature of deeper structures. Lateral density heterogeneities in the mantle, for example, produce gravity variations similar in wavelength to those of the undulations of the geoid. As an example of the effect of the geoid correction term on regional gravity and the consequences for interpretation, one can examine the regional high associated with marginal basins behind western Pacific island arcs. The regional free-air gravity anomaly field landward of the Mariana and Izu Bonin arcs averages approximately +25 mgal while the Pacific ocean basin has a regional field of approximately zero. The geoid height above the reference ellipsoid varies from as high as 60 meters behind these arcs to zero in the Pacific basin thus producing a geoid correction term of up to 16 mgal. After addition of this term to the free-air anomaly the gravitational attraction of anomalous mass in the marginal basin is 40 mgal, over the Pacific ocean basin it is still zero. This would result in a different interpretation about the extent and density of deep lateral mass heterogeneities.

Summary

The need for this geoid correction term was stated previously by Bomford (1962, p 443), and is thus not a new idea. This is only a timely reminder, since with the determinations of the geoid by the GEOS-3 radar altimeter the correction is now feasible. Of course it was possible to implement this correction prior to radar altimetry by using global gravitational field models, however, with GEOS-3 geoid data it can be done with a higher degree of accuracy. In geophysical studies of the long wavelength

gravitational field this correction is mandatory, although due to the long wavelength nature of the geoid it may not be significant in studies of the shorter wavelength gravitational field.

CHAPTER V ACKNOWLEDGMENTS:

References

Bomford, B., GEODESY, Oxford University Press, Oxford, England, 1962.

Cochran, J. R. and M. Talwani, Gravity anomalies, regional elevation and the deep structure of the North Atlantic, J. Geophys. Res., in press, 1978.

Grow, J. A., Crustal and upper mantle structure of the central Aleutian arc, Geol. Soc. Amer. Bull., 84, 2169-2192, 1973.

Lambeck, K., Gravity anomalies over ocean ridges, Geophys. J. R. astr. Soc., 30, 37-53, 1973.

Segawa, J. and Y. Tomoda, Gravity measurements near Japan and study of the upper mantle beneath the oceanic trench-marginal sea transition zones, in The Geophysics of the Pacific Ocean Basin and Its Margin, (ed.): G.H. Sutton, M. Manghnani, R. Moberle, Geophysical monograph 19, A.G.U., Washington, D.C., 35-52, 1976.

Chapter VI

Geoid Anomalies Over Deep Sea Trenches

Introduction

Measurement of the gravitational field in the world's oceans has resulted in an increased understanding of the physical processes which occur in the vicinity of deep sea trenches. It has long been recognized that island arcs and adjacent trenches are the site of some of the largest free-air gravity anomalies over the surface of the Earth. Ever since the development of pendulum measurements of gravity in submarines, a basic understanding of the primary features of gravity at island arcs has been possible. With only a few data points in a given transect it was possible to recognize the existence of a significant low in the free-air gravity anomaly directly above the trench axis and an adjacent high over the island arc. Utilizing the Vening Meinesz pendulum apparatus on the submarine H.M.S. Telemachus, four crossings of the Tonga Trench indicated this characteristic pattern of gravity anomalies (Talwani, et al., 1961). On one of the profiles a value of -224 mgal was observed over the Tonga Trench and a positive free-air anomaly of +153 mgal over the island arc. On the basis of earlier studies in the Indonesian archipelago Vening Meinesz (1954) observed that significant isostatic gravity anomalies existed in the region and suggested that the trench system existed as a result of horizontally compressive and shear stress.

When it became possible to make continuous gravity measurements on board a moving surface ship, a wealth of new information about the Earth's gravitational field became available. With this new data it became evident that many trenches had a distinct gravity anomaly seaward of the trench axis. This has been termed the Outer Gravity High (Watts and Talwani, 1974). One plausible explanation of this anomaly is that

132

at a trench the lithosphere undergoes elastic deformation producing a
bathymetric rise and consequent gravity high.

With plate tectonic theory it became evident that as the litho-
sphere descended into the relatively hot asthenosphere, the slow rate of
heat conduction permitted differences in temperature to be maintained.
These thermal conditions result in a density contrast between the cooler
slab and the surrounding hotter mantle and a consequent gravity anomaly.
It is uncertain what the actual differences in density are, but the
configuration of the descending slab is known from seismic studies.
Thus models of the density structure including the downgoing lithosphere
have been possible and were actually constructed for the Chile Trench
(Grow and Bowin, 1975), Aleutians (Grow, 1973), and Japan Trench (Segawa
and Tomoda, 1976). In all of these studies each new development in
instrumentation or theory resulted in a better determination and explanation
of the gravity field in the vicinity of deep sea trenches.

Measurement of the gravitational field in a marine environment has
heretofore been concerned with the radial component of the gravity
vector. However, as the gravitational field is a conservative force
field, it can equally be described in terms of the scalar gravitational
potential. On the Earth the equipotential surface of the gravity field
which coincides with mean sea level is termed the geoid. In the absence
of noise, determination of the shape of the geoid over the Earth's
surface would give information on the gravitational field equivalent to
that obtained by gravity vector measurements. In the presence of noise
geoid height measurements give more useful information for wavelengths
between several hundred and several thousand kilometers (Chapman and
Talwani, 1979). Determination of the shape of the geoid in marine areas
can contribute new and valuable information about the gravitational

133

field and the interior densities within the Earth. In this study measurements of geoid height in the vicinity of deep sea trenches enable identification of a characteristic geoid anomaly. For the Tonga-Kermadec Trench, geoid and gravity values are used to determine a new model of the density structure. These new measurements give better constraints on variations in mantle density than were previously available with only gravity measurements.

Data Acquisition

Geoid measurements are made by using a radar altimeter mounted on a spacecraft which orbits the Earth. In utilizing the GEOS-3 satellite to obtain estimates of geoid height, a certain procedure is used to collect and process the data. Mounted on board this orbiting spacecraft is a radar altimeter which is always oriented toward the center of mass of the Earth. During data acquisition the altimeter emits radar pulses which are reflected from the ocean surface and received by spacecraft antennas. In this manner measurements of the satellite altitude are obtained 100 times per second. When combined with accurate orbital tracking of the satellite, the height of the instantaneous sea surface relative to the reference ellipsoid is determined. Due to the existence of forces other than from the Earth's gravitational field, the sea surface at any given time may depart from the actual geoid. Such differences are caused by tides, currents, and other oceanographic phenomena. In general though, for the deep ocean these discrepancies can be considered noise which in amplitude is less than approximately 1 meter. After acquisition of the data, it is time averaged over .1024 second intervals; a second smoothing procedure averages the data over 2.2 or 3.3 second intervals. The data which we utilize is an average value of geoid height over a 14.4 km or 21.6 km distance; the ground speed of the sub-satellite track is approximately 6.55 km/sec. For all of the data which we use in this study, a listing of the instrument type, transmission mode, and date of acquisition is available in Table 1.

TABLE I - DATA CHARACTERISTICS

TRACK	ORBIT	UNIQUE NUMBER	INSTRUMENT MODE	TRANSMISSION MODE	ORBITAL ACCURACY†	TIME OF MEASUREMENT DAY	TIME OF MEASUREMENT YEAR	CENTER OF PROJECTION LATITUDE	CENTER OF PROJECTION LONGITUDE	CENTER OF PROJECTION AZIMUTH
ALEUTIAN AND KURIL TRENCH										
G4263	348	203	Intensive	High	A	124	1975	53.1°	-163.38°	165°
G3681	1642	2	Intensive	Low	J	216	1975	51.7°	-169.43°	165°
G3138	4983	215	Intensive	Low	J	87	1976	51.05°	-173.08°	165°
G4806	1965	288	Intensive	Low	D	238	1975	50.83°	177.45°	165°
G3509	2383	56	Intensive	Low	D	268	1975	45.87°	153.99°	135°
MARIANA AND BONIN ISLAND ARC-TRENCH SYSTEM										
G4824	2065	360	Intensive	Low	D	245	1975	26.68°	143.25°	75°
G4061	2264	503	Intensive	Low	J	260	1975	27.50°	143.80°	75°
G5323	1354	241	Intensive	Low	D	195	1975	23.22°	144.44°	65°
G4841	2150	421	Intensive	Low	D	251	1975	21.89°	146.28°	65°
G4799	1923	256	Intensive	Low	J	235	1975	31.80°	142.10°	90°
PHILIPPINE TRENCH										
G1684	2165	437	Intensive	Low	J	253	1975	15.65°	122.67°	75°
G1344	1980	300	Intensive	Low	J	239	1975	12.78°	125.82°	75°
G1255	2051	349	Intensive	Low	D	244	1975	10.58°	126.63°	75°
G1383	1795	156	Intensive	Low	J	226	1975	6.37°	127.05°	75°
G1694	1866	210	Intensive	Low	D	231	1975	4.72°	128.20°	75°
TONGA-KERMADEC TRENCH										
G2445	2155	424	Intensive	Low	J	252	1975	-21.07°	-173.51°	106°
G1989	2212	467	Intensive	Low	J	256	1975	-24.11°	-175.0°	106°
G1477	3321	770	Intensive	Low	J	334	1975	-28.03°	-175.82°	106°
G2018	2326	557	Intensive	Low	J	264	1975	-31.19°	-176.97°	106°
G1590	2511	189	Intensive	Low	J	277	1975	-35.25°	-178.61°	106°
PERU-CHILE TRENCH										
G3322	3594	904	Intensive	Low	J	354	1975	-11.58°	-79.21°	45°
G2668	3679	53	Intensive	Low	J	360	1975	-16.67°	-74.60°	45°
G2818	3167	669	Intensive	Low	J	323	1975	-20.20°	-71.27°	105°
G3630	3238	717	Intensive	Low	J	328	1975	-23.53°	-71.30°	105°
G3421	3309	764	Intensive	Low	J	333	1975	-27.47°	-71.86°	105°
G3469	4759	57	Intensive	Low	J	71	1976	-30.43°	-72.46°	105°
JAVA TRENCH										
G2029	4866	66	Intensive	Low	J	78	1976	-10.43°	110.46°	25°
G1874	1653	15	Intensive	Low	D	216	1975	-10.98°	113.48°	25°
G1870	1667	28	Intensive	Low	D	217	1975	-11.13°	116.87°	25°
G4754	1724	88	Intensive	Low	J	221	1975	-11.19°	115.41°	25°

† Orbital Accuracy
A = 10m rms based on 1 day arc by Wallops Flight Center - GEM-8 gravity model.
D = 3-10m rms based on 1-8 revolution arc by Wallops Flight Center - GEM-8 gravity model.
J = 3m rms based on 3 revolution arc by Naval Surface Weapons Center - NWL gravity model.

GEOID ANOMALIES OVER DEEP SEA TRENCHES

With the use of this GEOS-3 altimeter data, an extensive study of
geoid heights over island arc regions has been undertaken. As the data
was examined, it became possible to identify a characteristic geoid anom-
aly which exists over all major deep-sea trenches in the world's oceans.
This geoid anomaly is caused by the lateral density differences within
the Earth beneath the island arc region. With aqequate additional
constraints and proper interpretation, it can provide useful information
about the density and structure of the upper mantle and the physical
processes which occur at deep sea trenches.

To discern the characteristic geoid anomaly over deep sea trenches,
we examine the various trench systems in the Pacific and Indian Oceans.
These are in turn the Aleutian and Kuril Island arc system, the Mariana
and Bonin Island arc-trench region, the Philippine Trench, the Tonga-
Kermadec region, Peru-Chile Trench, and lastly the Java Trench. Over
each of these deep-sea trenches a set of representative geoid profiles
is displayed. Track locations of all the data are illustrated in Figure
1, while instrument and data characteristics are listed in Table 1. For
each of the geoid tracks the data has been projected to a line per-
pendicular to the strike of the trench axis; as the original tracks are
fairly linear, this only represents a scale change. Profiles from each
trench region are displayed in Figures 2 through 7. Bathymetry and
gravity data from a nearby ship track is shown along with geoid profiles
from the GEOS-3 satellite.

Geoid profiles from the Aleutian and Kuril Trench are illustrated
in Figure 2. These data clearly indicate the type of profile which will
be seen as characteristic of all deep sea trenches. Beginning about
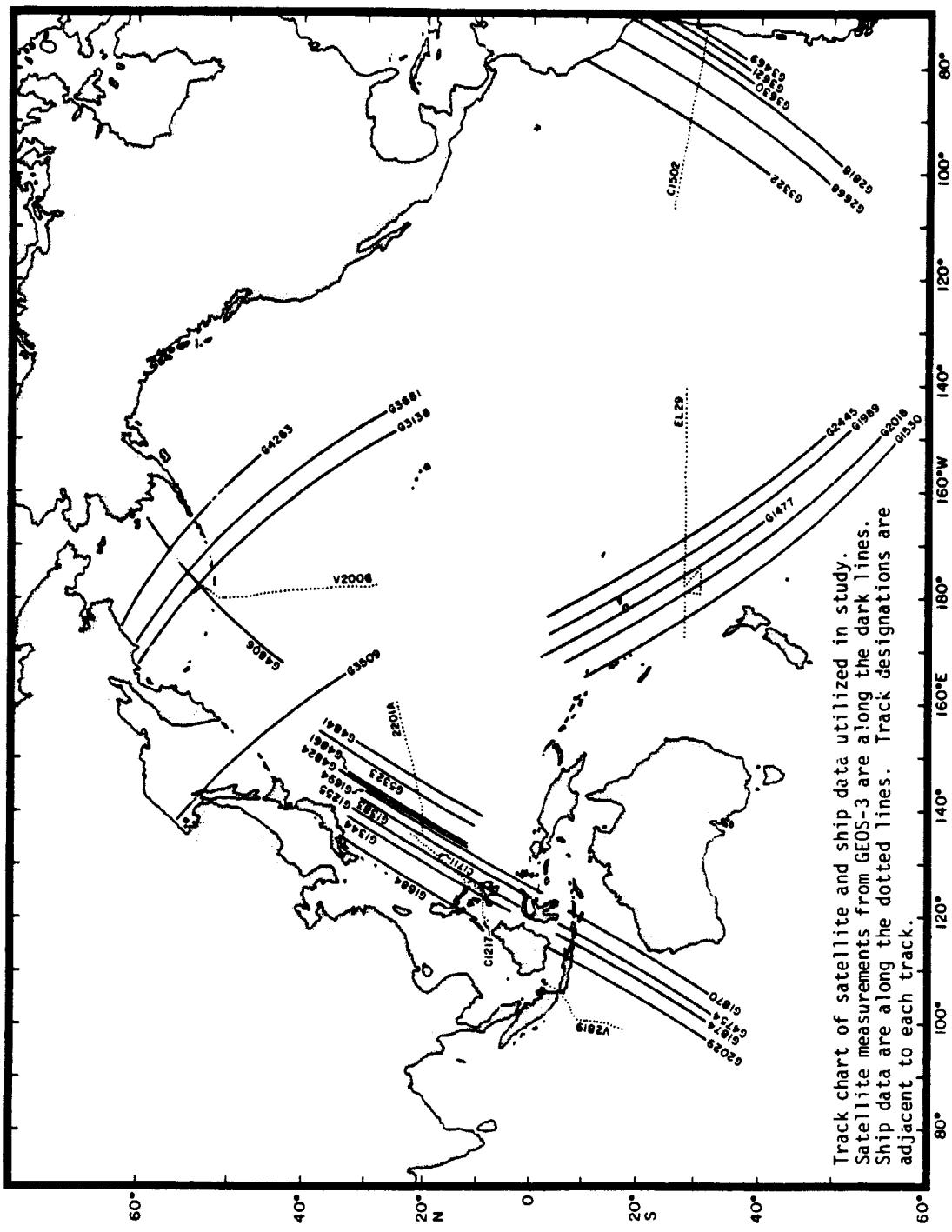
137

Figure 1

Track chart of satellite and ship data utilized in study.
Satellite measurements from GEOS-3 are along the dark lines.
Ship data are along the dotted lines. Track designations are
adjacent to each track.

138

ALEUTIAN TRENCH

Figure 2

139
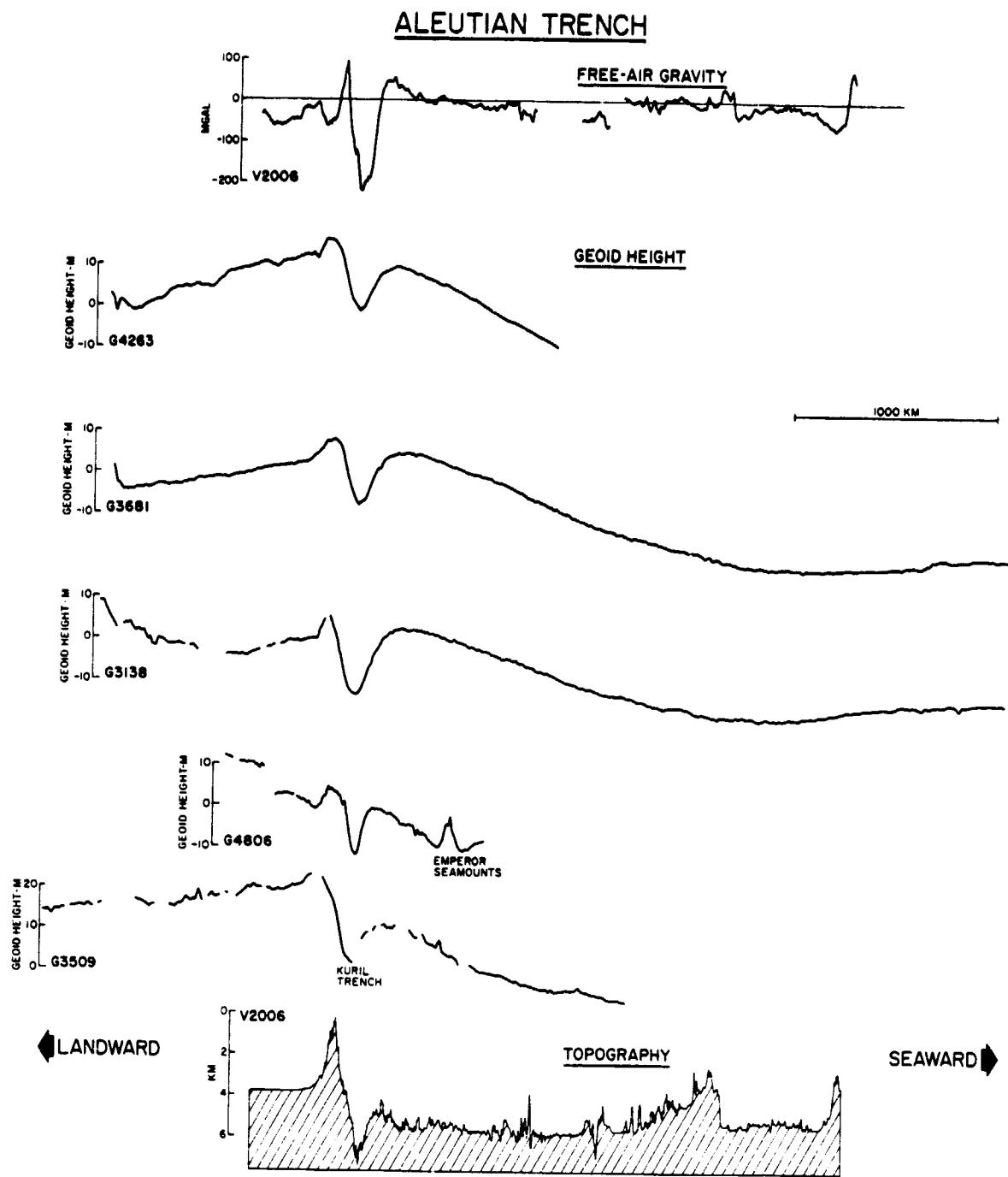
MARIANA AND BONIN ISLAND ARC-TRENCH SYSTEM

Figure 3
140

PHILIPPINE TRENCH
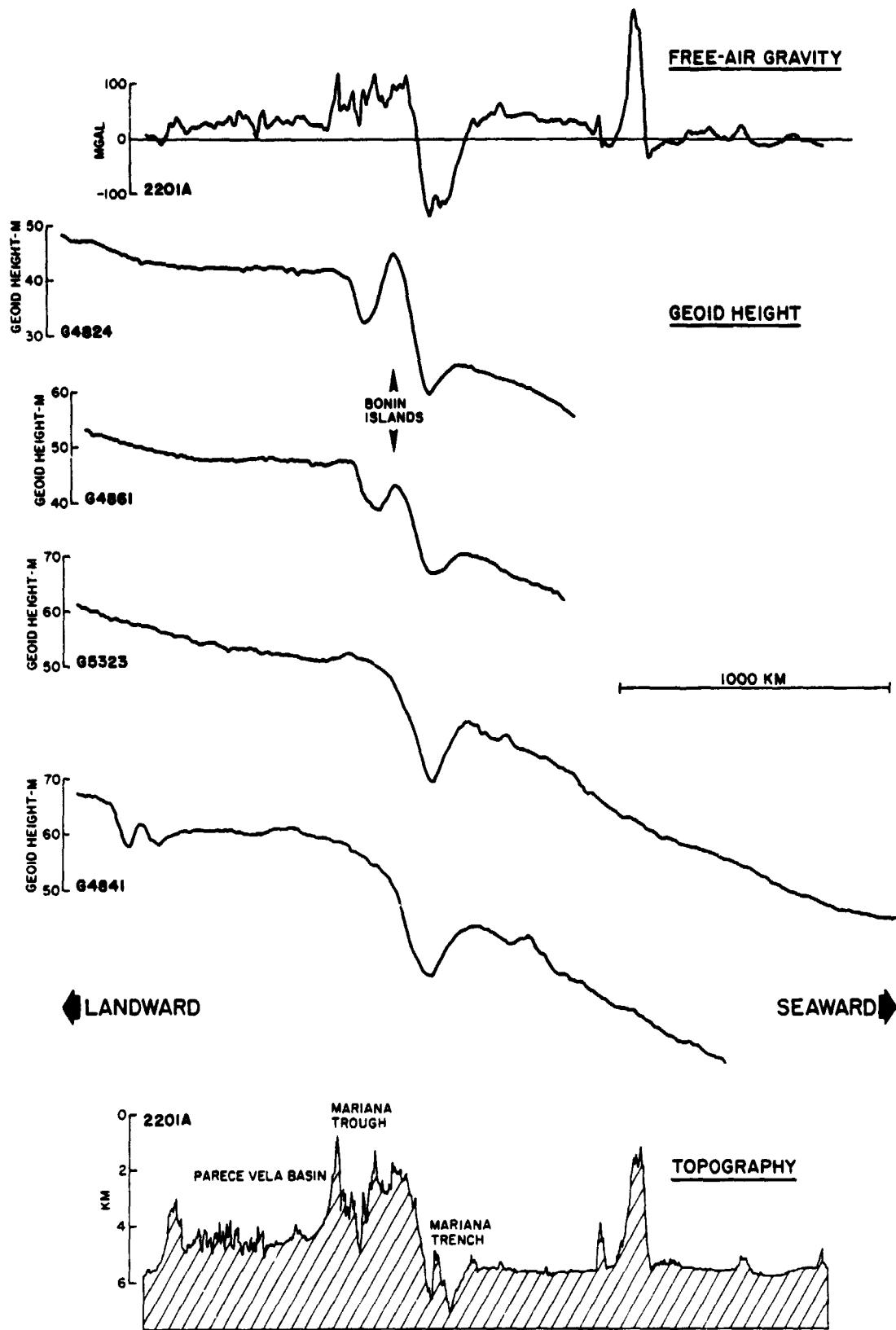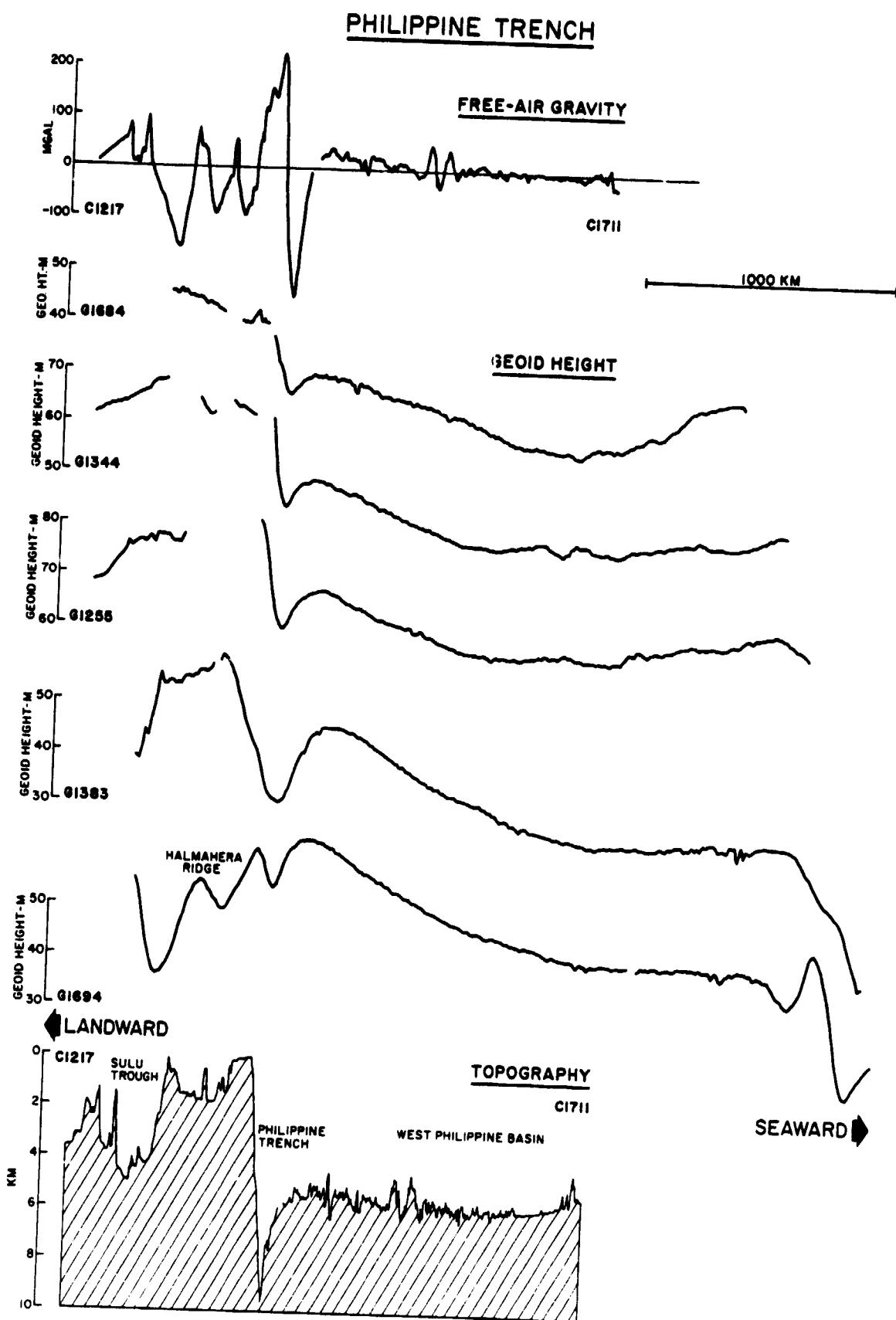
Figure 4
141

Figure 5

PERU-CHILE TRENCH
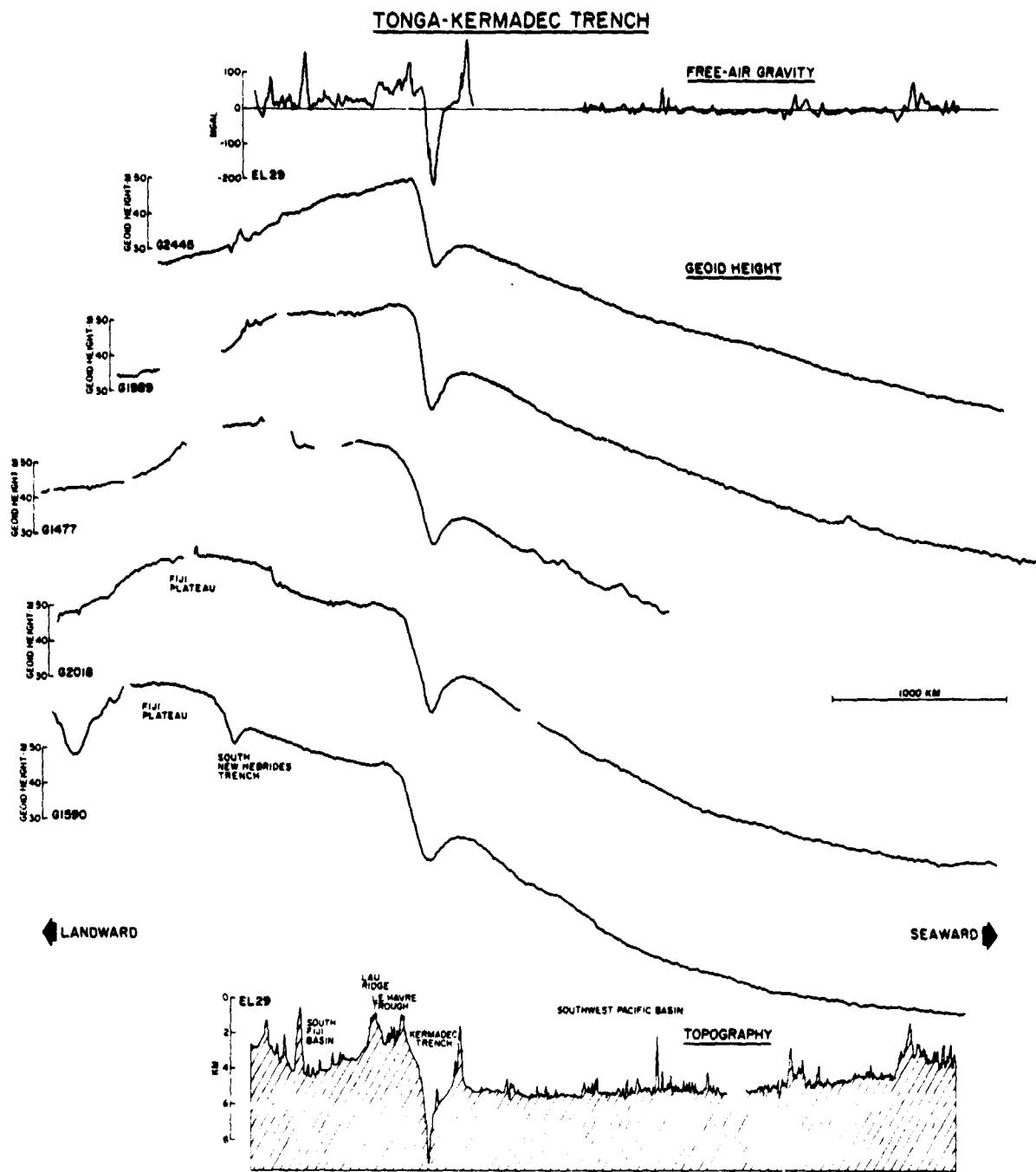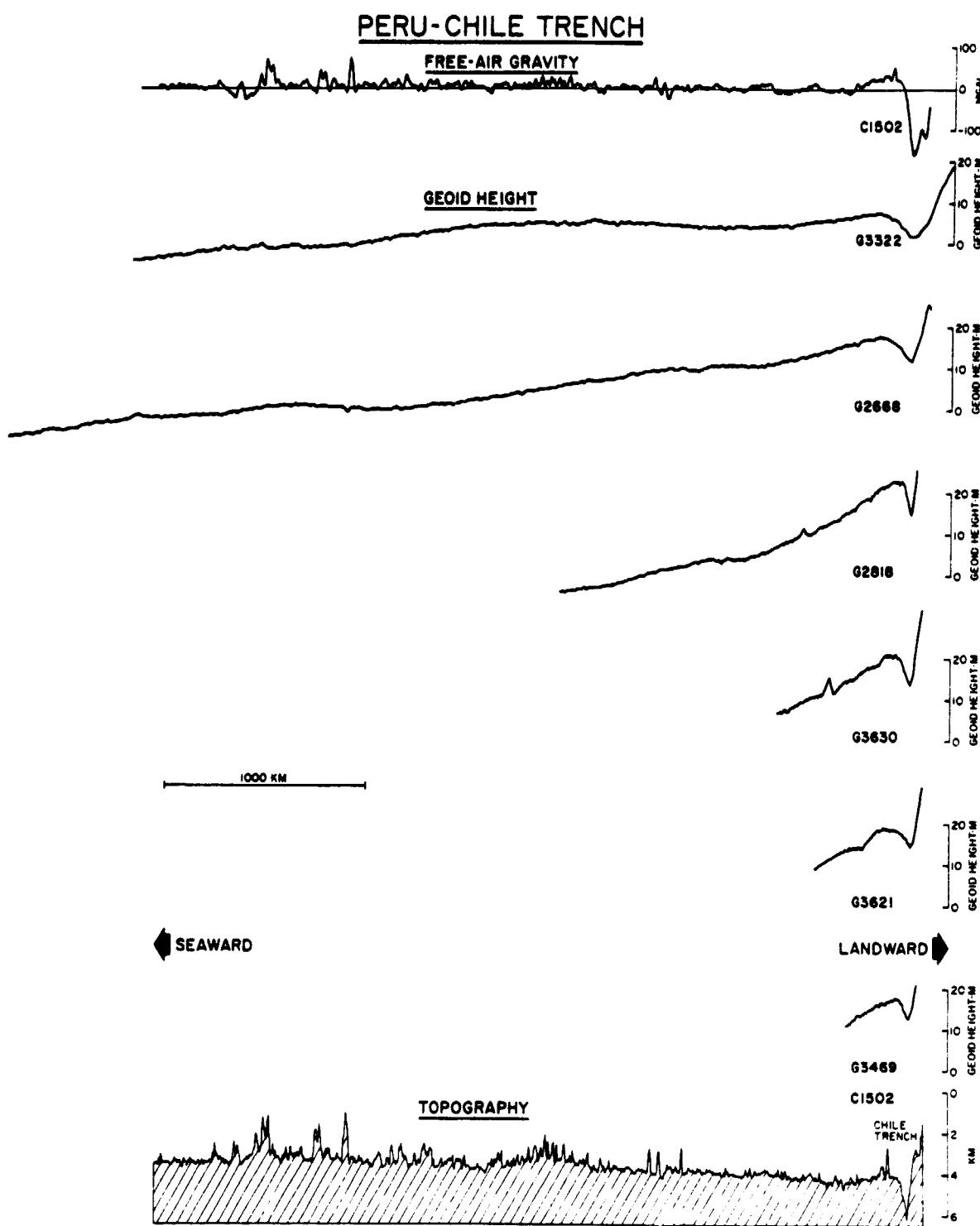
Figure 6
143

Figure 7

144

2000 kilometers seaward of the trench axis, the geoid has a constant increase in height as the axis is approached. This slope is about 20 meters over a distance of 1800 kilometers. Directly above the deep-sea trench there is an approximate 13 meter decrease to form a low 150 kilometers in width. Immediately landward of the minimum there is an approximate 18 meter increase until a maximum is reached directly above the island arc. Behind the arc there is a gradual decrease in geoid height of about 10 meters over a 1000 kilometer interval. All of these tracks show both the deep low over the trench axis and the adjacent high above the island arc. Tracks G4263, G3681, and G3138 all have the gradual decrease behind the arc. Track G4806, however, has a slight increase and then a step to a higher level. This step in geoid height occurs at the continental margin southwest of Alaska. This same track also passes over the Emperor Seamounts and shows the characteristic high and flanking lows (Watts, 1979). Over the Kuril Trench track G3509 has the same features as the Aleutian Trench.

An appropriate area to study deep-sea trench anomalies is in the region of the Philippine Sea. This is the location for the Mariana and Izu-Bonin, Philippine, Japan, and Ryukyu Trench systems. At the eastern boundary of the Philippine Plate the Mariana and Bonin Island arc-trench system has an interesting sequence of geoid undulations. Above the Izu-Bonin Trench tracks G4824 and G4861 in Figure 3 have an increasing geoid height as the trench axis is approached from the seaward side. Directly over the axis of the trench there is a minimum of approximately 5 meter amplitude. This is followed by an 18 to 25 meter increase to the high over the Bonin Islands. Adjacent to this Bonin high there is another minimum which is about 6 to 8 m in amplitude. Landward of the arc the

geoid height remains fairly constant with a gradual increase. Further
south above the Mariana Trench the increase in geoid height seaward
of the trench is more evident due to lengthier tracks of data with G5323
and G4841. With these two profiles the increase in geoid height is
35 meters over 1500 km distance. Over the Mariana Trench axis there is
a 10 meter minimum followed by a steep 20 meter increase landward of the
axis. Above the Parece Vela Basin the geoid is fairly constant or has a
gradual increase.

In the western Philippine Sea the plate boundary is marked by the
location of the Philippine Trench. GEOS-3 geoid profiles over this
region are illustrated in Figure 4. In these tracks, as they approach
the trench axis from the West Philippine Basin, the geoid gradually
increases in height by up to 20 m over 1800 km. Over the Philippine
Trench itself there is a 5 to 15 m low, followed by a steep 15 to 25 m
increase to a geoid high landward of the trench. Track G1694 passes
over the Halmahera Ridge which has a 5 m high and two flanking lows. In
the gravity field over this ridge there is a +36 mgal anomaly and an
adjacent -187 mgal low (Watts, 1976).

Some of the clearest examples of the geoid anomaly at deep sea
trenches occur in the region of the Tonga and Kermadec Trench system.
These are illustrated in Figure 5. Beginning in the Southwest Pacific
Basin the geoid increases in height as the trench is approached. This
is an increase of almost 40 meters over a 2800 km distance. Similar to
the other trench axes discussed previously, there is a 10 m low over the
axis of the Tonga-Kermadec Trench. This low is followed by a steep
increase of up to 30 m to the high region over the South Fiji Basin.
For GEOS-3 track G2445 the geoid immediately begins to decrease landward

146

of the trench axis; from Figure 1 it is seen that the track almost immediately is back over the Pacific Basin. For tracks G1989 and G1477 the geoid decreases when the Pacific Basin is similarly reached. Both tracks G2018 and G1590 cross over the South Fiji Basin and then have a local high above the Fiji Plateau. Track G1590 has a slight minimum above the South New Hebrides Trench.

On the eastern side of the Pacific Ocean the Peru-Chile Trench is the location for subduction of the Nasca Plate. This trench also has a gradually increasing geoid height as the trench axis is approached from the seaward side. At this trench, however, the increase is very slight-- only about 10 to 20 m over 1500 km (Figure 6). Again, as seen in the other regions, there is a 5 to 7 m low over the trench axis followed by a 10 to 15 m step at the continental margin. Due to the presence of land, no altimeter measurements were made landward of the trench.

Outside of the Pacific Ocean the only major trench system is in the Indian Ocean, the Java Trench. This region has the steepest geoid anomalies seaward of the trench. At this location there is a slope of about 55 m over a 1500 km distance (Figure 7). Above the trench itself the low is not as pronounced as in other regions. Here it is only about 2 to 5 m deep. Following the trench low there is a dramatic 30 m increase to the high region over the Java Sea. This increase in geoid height continues behind the arc at about the same rate as seaward of the trench.

After observation of GEOS-3 altimeter data over these active subduction zones, an important conclusion is possible. Over all major deep-sea trenches there is a distinct pattern in the geoid. Beginning anywhere from 1000 to 3000 km seaward of the trench, the geoid increases

147

in height until just prior to the trench axis. This very long increase
has a slope of 7 meters per 1000 km (1.4 seconds of arc) at minimum to
37 meters per 1000 km (7.6 seconds of arc) at maximum. In shape this
increase seaward of the trench is in some cases concave downwards
(Aleutian Trench); concave upwards (Java Trench); or fairly linear
(Tonga Trench). Directly over the trench axis there is a narrow minimum
in the geoid. This low is from 100 to 200 km in width and in depth
anywhere between 3 m and 15 m (measured from the maximum on the seaward
boundary). From the base of the trench axis low there is a steep
increase of up to 30 m to a high region landward of the trench axis. In
some cases there is a distinct geoid high above the island arc. This is
most obvious with the Bonin Islands and also the Aleutian Arc. Landward
of the island arc the geoid is somewhat variable; behind the Aleutians
there is a gradual lowering of geoid height. However, over the Java
Sea the geoid continues to rise. In other regions the geoid remains
fairly level landward of the trench. These features then are character-
istic of the geoid in the vicinity of deep-sea trenches; a gradual long
increase as the trench is approached from the ocean basin, a narrow low
over the trench axis, and a relative high but with variable slope
landward of the trench.

148

Gravitational Field in Vicinity of Deep Sea Trenches

From the GEOS-3 altimeter measurements the characteristic geoid anomaly over deep sea trenches has been ascertained. In previous work at the ocean surface marine gravimeters have always been utilized to measure the gravitational field. These former studies have defined the free-air gravity anomaly which is characteristic of deep sea trenches. An early study of the Tonga Trench mapped the major features of the free-air gravity (Talwani, et al., 1961). In this work pendulum measurements were used to detect the large negative anomalies over the trench. Above both the Tonga and Kermadec Trench the free-air gravity has a minimum 100 to 200 km in width and -200 mgal in amplitude. Landward of the trench over the Tonga Ridge positive gravity anomalies, 100 to 150 mgal in amplitude, were described by Talwani, et al. (1961). This region has a representative example of the typical free-air gravity anomaly above the trench and island arc. A gravity and bathymetry profile from Eltanin 29 is illustrated in Figure 5. For this profile there is a -220 mgal low over the Kermadec Trench and an adjacent 50 to 100 mgal high above the Lau Ridge and Le Havre Trough. Other regions have similar gravity profiles, although at the Java Trench there is a double gravity low with an intermediate high (Figure 7).

Another common feature of the gravitational field is the existence of a positive free-air gravity anomaly seaward of deep sea trenches. This has been designated the Outer Gravity High by Watts and Talwani (1974). Originally observations of a bathymetric rise seaward of the Kuril Trench led Hanks (1971) to suggest horizontally compressive stresses occur in this region. According to his hypothesis, these stresses acting normal to the trench axis cause elastic deformation

149

of the lithosphere resulting in an outer bathymetric rise. This concept
was utilized by Watts and Talwani (1974) to explain the occurrence of the
Outer Gravity High. In their model the elastic flexure of the litho-
sphere causes the crust to bend upwards thus resulting in a positive gravity
anomaly. Gravity and bathymetric profiles from _Vema_ 20-06 in Figure 2
show the outer topographic rise immediately seaward of the Aleutian trench
and the associated positive free-air gravity anomaly 50 mgal in amplitude.

A final feature of the gravitational field is the gravity anomaly
landward of the trench. Above marginal basins the free-air values are
near zero or slightly positive. As the crust in this area has a normal
oceanic thickness yet occurs at shallow depths relative to the deep
basin, it is possible to infer the existence of low density upper mantle
(Karig, 1971). Beneath the Fiji Plateau Solomon and Biehler (1969)
discovered a mass deficiency equivalent to a 1% density decrease to
100 km depth located within the mantle. Yoshii (1972) calculated that
low density mantle material occurs beneath the Sea of Japan. And behind
the Izu-Bonin Trench, Segawa and Tomoda (1976) also calculated lower
average mantle densities. What all of these studies indicate is the
presence of lower mantle densities behind deep-sea trenches, when compared
to the deep ocean basins.

Combining all of these observations together, one can describe the
characteristic free-air gravity in the vicinity of deep sea trenches.
Immediately seaward of some trenches there is often an Outer Gravity
High. This is about 50 mgal in amplitude and several hundred kilometers
in width. Directly above the trench axis there is a narrow low, usually
-150 to -250 mgal in amplitude. In the island arc region there are positive
anomalies over the topographic highs with amplitudes of more than +200 mgal
Landward of the island arc the free-air gravity anomaly is often close to

zero or slightly positive. However, after elimination of crustal effects, lower average mantle densities are present when compared to the deep ocean basin region.

Combination of Gravity and Geoid Measurements

Technically, measurement of either the gravity field or geoid gives all the information possible about density variations within the Earth. Only one type of measurement is necessary. In a practical situation, due to the presence of noise, both altimetry and gravimetry measurements are useful for studying the density heterogeneities; they provide complementary information. To see why this is true, consider the nature of the geoid and gravity field. As observed in the previous figures (2 to 7), the geoid mostly has gradual undulations. Primarily it has long wavelength information. Free-air gravity anomalies, however, contain many fine details; in the gravity field short wave-length information is most evident. Due to the long wavelength character of the geoid and the high wavenumber nature of the gravity field, for wavelengths longer than a certain number a radar altimeter will record the gravitational field with a higher signal to noise ratio; but at shorter wavelengths a marine gravimeter will perform better. This is illustrated in a quantitative manner by Chapman and Talwani (1979). When using data from both an altimeter and gravimeter the best possible information can be obtained at both shorter and longer wavelengths.

For the Earth's gravitational field quite often long wavelength anomalies are ascribed to deeper structures while shorter wavelength features are explained by the more shallow structure. For example, gravity anomalies less than several hundred kilometers wide are often modeled by crustal structure as in the study by Talwani et al. (1961). Long wavelength undulations typically are explained by phenomena within the mantle. Bott (1971) suggested the mantle transition zone was the cause of harmonics for wavelengths longer than degree and order 8.

152

This practice of relating longer wavelength anomalies is explained by two principles. If a deep body has detailed structures and consequent high frequency gravity anomalies locally, these details will be lost due to attenuation with depth - only long wavelength information will remain. A second principle is that long wavelength gravity anomalies cannot be maintained by shallow structures. They would generate stress differences in excess of the breaking strength of the shallow material. Combining these principles with the previous discussion, it is possible to see that marine gravity probably gives the best constraints on the shallow densities while radar altimetry is most useful for determining the deeper density heterogeneities. When data from these two sources are combined, there should be useful information about both the deep and shallow lateral density variations within the Earth.

In using both geoid and gravity data to constrain Earth models, a problem arises with the gravity values. Very often in the region landward of the island arc the free-air gravity anomaly is close to zero, yet the geoid is high. This would appear to make interpretation quite difficult. It must be realized though that the free-air gravity anomaly is caused by both mass inhomogeneities and changes in height of the geoid. Any effect due to geoid height differences is often termed the 'Indirect Effect'. To insure that gravity values are only caused by anomalous mass, a geoid correction term should be added to the free-air gravity. These geoid corrections in marine gravity are discussed by Bomford (1962) and by Chapman and Bodine (1979). After correction for this factor both gravity and geoid values may then be properly interpreted.

To give a concrete example of these ideas, we utilize a previously published density model. In a thorough study of the Izu-Bonin Trench, Segawa and Tomoda (1976) used the free-air gravity anomaly and seismic refraction data to infer the crust and upper mantle density structure. Their model had an excellent match with the observed free-air gravity values. A reasonable question to ask then is can this model be used to calculate geoid heights in agreement with the observed values. To answer this we utilized their model to compute the geoid anomaly. The result is illustrated in Figure 8. Above the calculated geoid height, the observed values from GEOS-3 are shown. The computed anomaly compares poorly with the observed data. This density model cannot explain the geoid anomaly over deep sea trenches. This poor agreement is due to two factors. As the calculated geoid values disagree with the measured data, there are obviously incorrect densities in their model. From our previous discussion it may be suggested that these incorrect density values are within the mantle. This is, however, not certain. Another important factor is the use by Segawa and Tomoda of the free-air anomaly. They neglected the 'Indirect Effect'. Landward of the arc, a value of at most 12 mgal should have been added to the free-air anomaly prior to interpretation. We have used this example to indicate that the use of geoid data in conjunction with gravity values provides a new and more powerful constraint on density models. The study of the Izu-Bonin Trench by Segawa and Tomoda (1976) was one of the most complete and excellent studies of a trench region; their model had very good agreement with the data they utilized. At this time, however, new data on geoid heights are available which would provide additional information to constrain their density model.

154

IZU-BONIN TRENCH
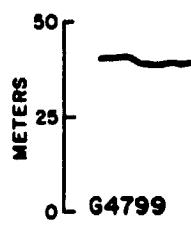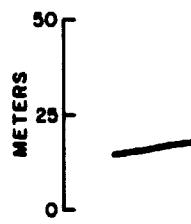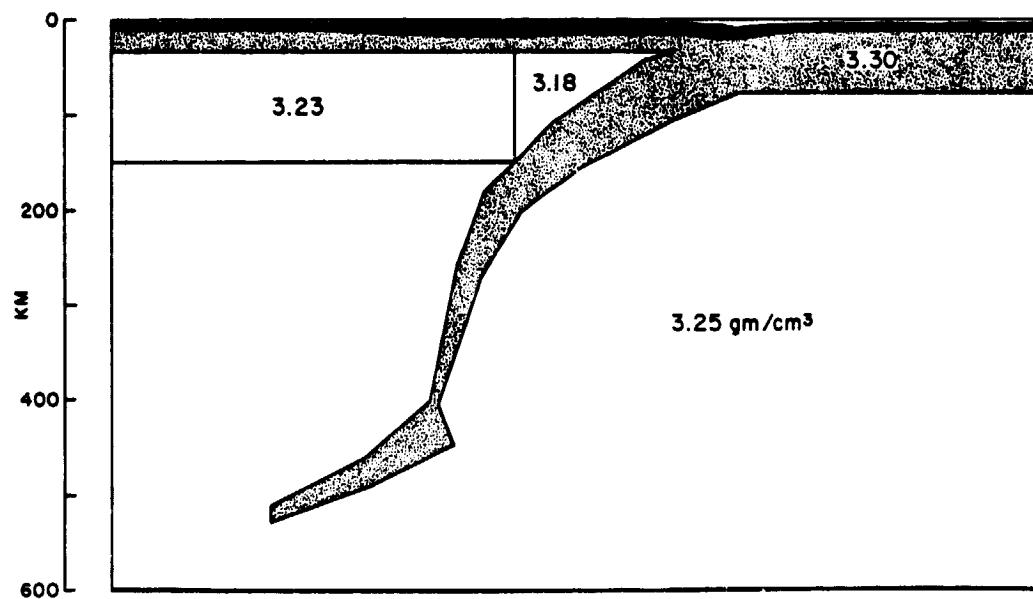
Figure 8

Possible Causes of the Geoid Undulation

Due to the inherent ambiguity in gravity interpretation, it is always necessary to first consider the relevant physical processes for a given region. An understanding of these processes enables the range of possible density models to be greatly restricted. Existence of a positive regional free-air gravity anomaly landward of active trenches has been previously known due to satellite based gravity models (Kaula, 1969). A primary suggestion as to the cause of this anomaly is an excess mass due to descending lithosphere. While the slab penetrates into the asthenosphere it gradually heats up due to thermal conduction. As the rate of heat transfer is quite slow compared to the rate of subduction, the descending slab is in many cases cooler than the surrounding asthenosphere. Due to such thermal differences, the slab is denser than the adjacent material. This is an excess mass and causes a positive gravity and geoid anomaly (Griggs, 1972; Hatherton, 1970 and 1969). In the calculations by Griggs the density contrast between the slab and surrounding asthenosphere was at some depths greater than .2 gm/cm^3. This generated a gravity anomaly of +100 to +300 mgal in amplitude, depending upon the model parameters. Griggs also specified an undefined form of regional compensation. In a study of the crust and upper mantle beneath the Chile Trench, Grow and Bowin (1975) utilized density contrasts between .024 and .05 gm/cm^3 for the descending lithosphere. For the Izu-Bonin Trench, Segawa and Tomoda (1976) used a density contrast of .05 gm/cm^3 for the slab. In a discussion on the gravity effect of downgoing slabs Watts and Talwani (1975) concluded the total gravity effect is limited in extent to the island arc-trench region and suggested that the regional positive anomaly is due to some other mass inhomogeneities.

156

In order to analyze the possible effect of a denser slab, a simple calculation has been made utilizing a two-dimensional technique (Chapman, 1979). The hypothetical slab extends from 100 to 400 km depth where there is a density contrast of +.04 gm/cm^3 with the surrounding mantle (Figure 9A). For this theoretical example there is a gravity anomaly of +55 mgal and a geoid undulation of 30 meters. The geoid anomaly is maximum over the center of the slab and decays downwards on either side. It should be noted that for all these two-dimensional calculations the absolute level of geoid height is arbitrary.

Another possible suggestion as to the cause of the trench geoid anomaly might be the outer bathymetric rise often found seaward of deep sea trenches. Such a model has been utilized to explain the free-air gravity seaward of the trench axis (Watts and Talwani, 1974). In the study of Watts and Talwani the bathymetric rise was considered to be the result of elastic flexure of the lithosphere due to regional stress fields. In Figure 9B such a possible model is illustrated. While the calculated gravity can explain the Outer Gravity High at trenches, the computed geoid anomaly is only 5 m high and a few hundred kilometers wide. As the observed geoid anomaly at deep sea trenches is much wider and larger in amplitude, the outer bathymetric rise would explain only a minute portion of the observed geoid undulation.

One plausible mechanism to generate the geoid high involves density changes within the mantle. Gravity studies in the past have indicated a need for lower mantle densities (relative to the deep ocean basin) landward of the trench. This observation was made by Karig (1971) after studying seismic and gravity results at marginal basins. He noticed

157

POSSIBLE CAUSES OF GEOID UNDULATION
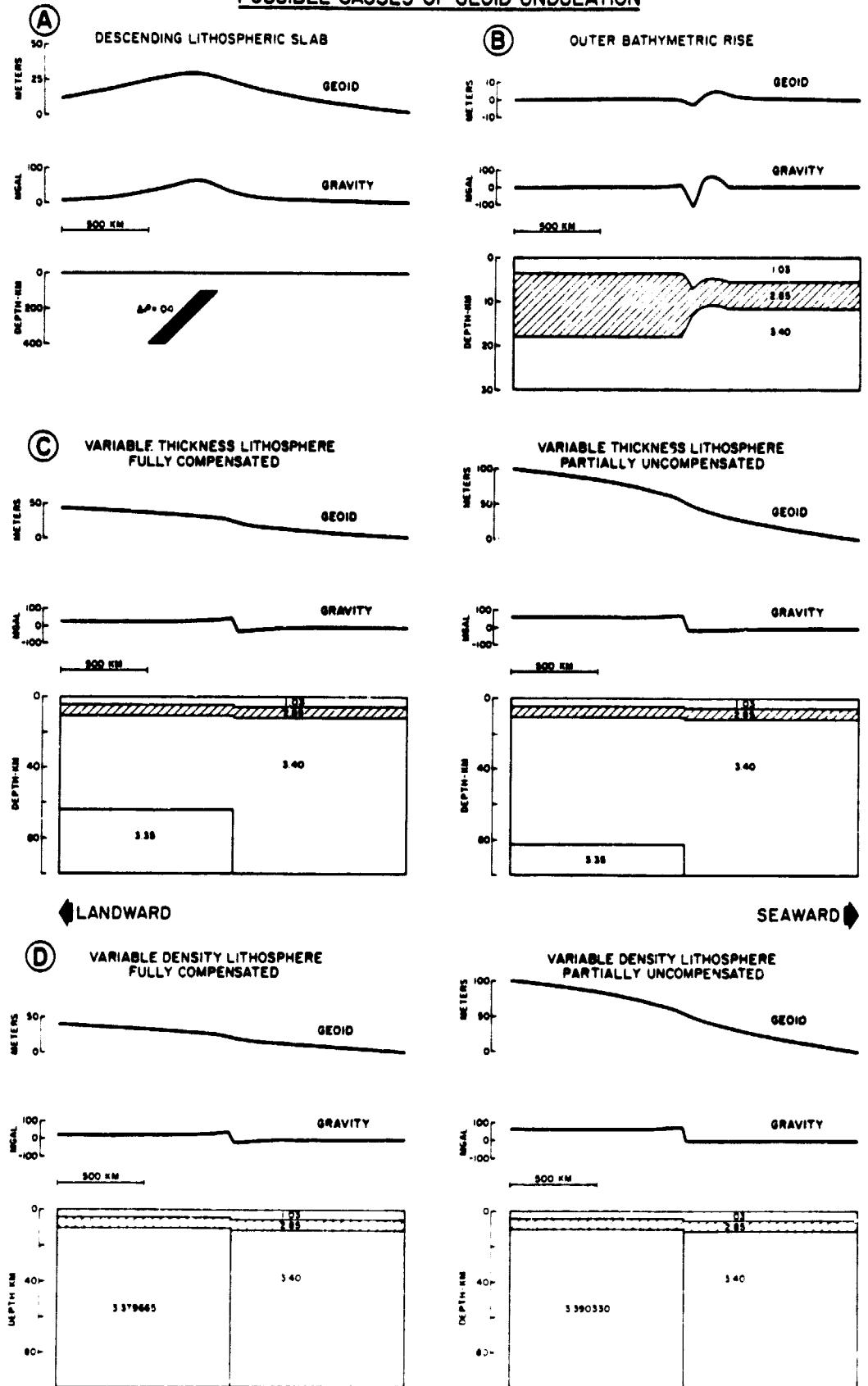
Figure 9

free-air values of gravity were near zero above these basins. Seismic
results showed the crust in these areas to be of standard oceanic
thickness, and yet to occur at shallower depths relative to the deep
ocean basin. Arbitrarily assuming deep ocean basin to be normal, behind
the trench there are higher densities at shallow depths. Relatively
lower densities occur deeper. This is a dipole type, layered mass
distribution. Using the expressions of Ockendon d Turcotte
(1977), this type mass distribution is seen to cause a positive geoid
anomaly above the marginal basin.

There are two possible ways to have lesser average mantle densities:
either lateral changes in thickness or density of a body. Figure 9 C
illustrates the first possibility. In the region landward of the arc
water depths are shallower, yet crustal thickness is everywhere constant.
At these shallow depths there are higher relative densities landward of
the arc, when compared with the deeper ocean basin. Compensation
occurs by having lower density (3.35 gm/cm^3) mantle material at depth.
If compensation is not complete then the geoid and gravity high are
accentuated. This case is also illustrated in Figure 9 C. Figure 9 D
illustrates the second possible type mass distribution. Compensation
occurs by having lower density material throughout the mantle to 100 km
depth. An important observation can be made by comparing Figures 9 C
and 9 D. Both of these models cause virtually identical geoid and
gravity values. Thus utilizing this type of data, the two types of
possibilities are indistinguishable. Additional constraints would
be necessary to differentiate between the two causes.

One final process which might affect geoid undulations is the
presence of phase transformations within the descending lithosphere.
Due to changes in pressure and temperature in the subducting slab, the

159

mantle material will undergo changes in phase at various depths (Ringwood, 1976). Due to thermal differences, the transition at 400 km would migrate upwards in the slab with a consequent .2 gm/cm^3 increase in density. If the slab is considered a separate body, then it will conserve mass and the volume of the slab will decrease due to such phase changes. Decrease in the slab volume insures that the total excess mass is constant. After phase transformation the calculated geoid and gravity anomaly is virtually identical to the values calculated prior to the change of phase. This is because the total excess mass is unchanged. Thus any occurence of phase transformations within the descending litho-sphere has no effect on the calculated geoid and gravity anomaly. There is of course no harm in including phase transitions within the descending lithosphere, as many authors have done.

After considering all of these physical processes, several obser-vations are possible. Any effect of the downgoing slab may be signi-ficant. However, the calculated anomaly is maximum over the center of the slab and decays to either side. This calculated shape is dissimilar to the observed geoid undulation over deep sea trenches. The slab effect may be a contributory cause but cannot be the only mechanism which is involved. There must be some physical process to generate a generally high geoid anomaly landward of the trench axis. A probable mechanism which will explain the geoid high behind the arc is a shallow crust either partially or totally compensated at depth by a mantle with variable thickness or density. Any presence of an outer bathy-metric rise will have only a minor effect on the calculated geoid; phase transformations within the descending slab will have no effect on the calculated geoid undulation.

160

Study of the Tonga-Kermadec Trench

Any attempt to ascertain the cause of the geoid anomaly over deep-sea trenches is best made by the explicit study of a given region. In the vicinity of the Tonga-Kermadec Trench the characteristic geoid undulation is quite evident and suitable data exists to study this area. One of the earliest studies of the Tonga Trench utilized pendulum gravity measurements aboard a submarine in combination with seismic refraction data. In this study by Talwani et al. (1961) a crustal thickness of 36 km was calculated for the Tonga-Kermadec Ridge. As part of a comprehensive study of Melanesia extensive two-ship seismic refraction results were reported by Shor et al. (1971). This latter work is very useful because the seismic results give constraints on the thickness of the crust and sediments landward of the trench axis.

In this present study gravity data were utilized which had been obtained on Eltanin cruise 29 from June to August 1967. Gravity measurements were made with a Graf Askania Sea Gravimeter Gss 2 mounted on an Anschutz stable platform with an electrically erected gyro. Cross coupling errors were corrected by the use of an analog system. During this cruise a satellite navigation system in combination with the ship's electromagnetic log was used to provide accurate locations. Navigation, bathymetry, gravity and seismic profiles from Eltanin 29 are presented in a report by Hayes et al. (1972).

Profiles of bathymetry, gravity and geoid data across the Kermadec Trench are illustrated in Figure 10. The gravity values are the gravitational attraction of anomalous mass. This is obtained by addition of a geoid correction term (Chapman and Bodine, 1979) to

161
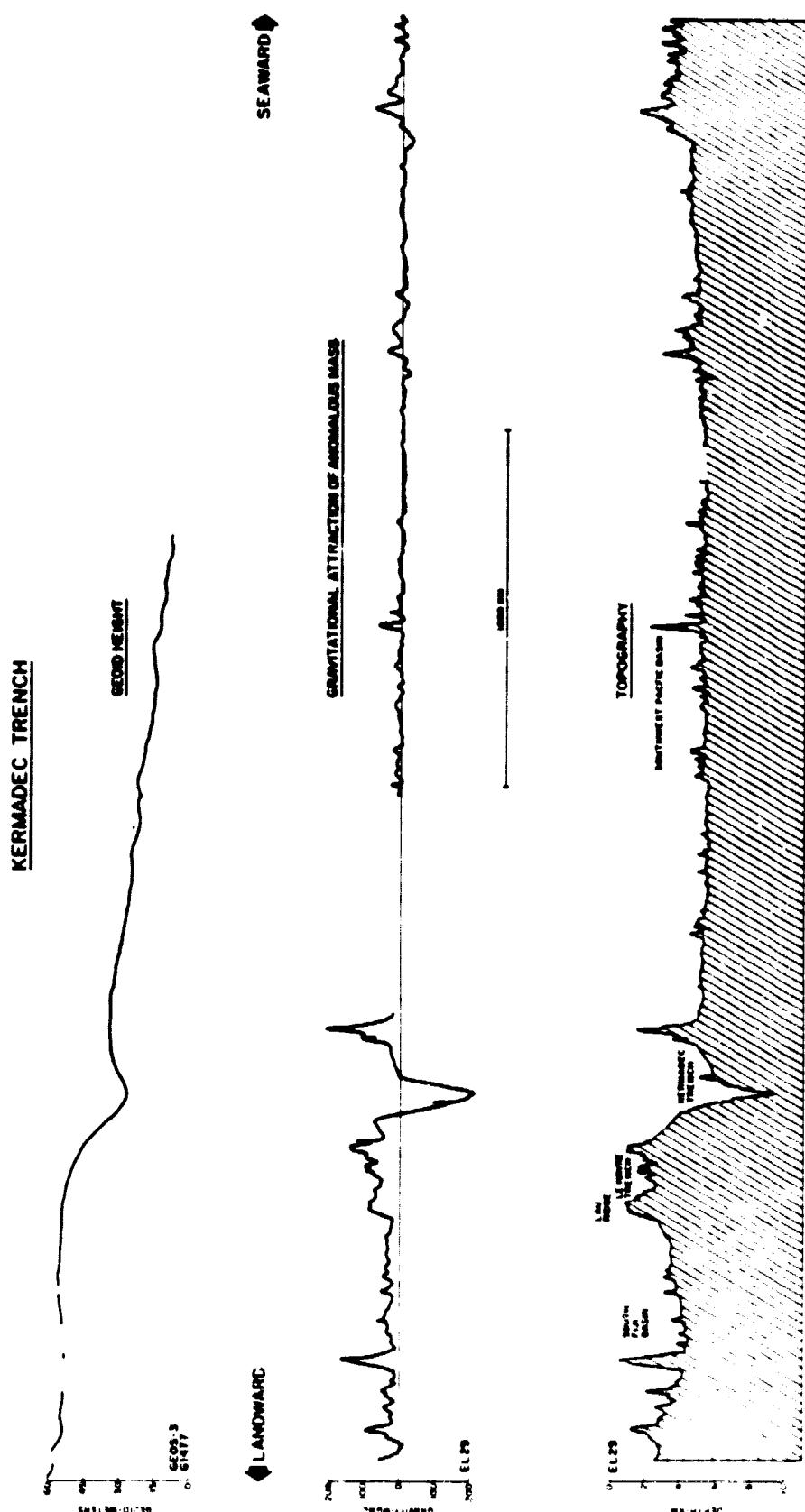
Figure 10

the free-air gravity anomaly. The effect of this correction is to increase the gravity values landward of the trench by 18 mgals maximum. Geoid measurements are from the GEOS-3 satellite. Both gravity and geoid values are referenced to a best fitting ellipsoid with flattening 1/298.255.

With the gravity data there is a 210 mgal high over Osborne Seamount (Part of Louisville Ridge) immediately seaward of the trench axis. Directly above the Kermadec Trench the gravity minimum is -210 mgal, while over Lau Ridge and Le Havre Trough gravity values average +70 mgal with peaks up to +140 mgal. Landward of the arc system there is a regional high of about +35 mgal above the South Fiji Basin. With data from GEOS-3 track G1477 the geoid anomaly characteristic of deep-sea trenches is evident. Beginning 1600 kilometers seaward of the trench axis the geoid is +8 meters; gradually it increases in height to +36 meters. Over the Kermadec Trench there is a low region in the geoid which is at a +27 meter level. Landward of the trench the geoid increases in height up to +56 meters, it remains at this high level above the South Fiji Basin.

Any model of this region must be able to explain the general characteristics of the gravity and geoid. The density model must be able to produce a calculated geoid high landward of the arc, a local minimum above the trench axis and a gradual decrease in geoid height progressively seaward of the trench axis. From the bathymetry it is evident that the South Fiji Basin, Lau Ridge and Le Havre Trough are shallower than the Southwest Pacific Basin. These shallower depths must be at least partially compensated otherwise there would be much higher gravity values landward of the trench. Of primary interest then is where the lower average densities must occur.

163

A standard assumption in gravity modeling is that variations in crustal thickness can be the mechanism of compensation. In our model this was not the sole mechanism. Our final crustal model is illustrated in Figure 11. The gravity effect of this is also shown in comparison with observed data. Quite obviously this model produces gravity values much greater than observed data for the region landward of the trench axis. This calculation indicates the necessity for lower average densities to be present in the mantle landward of the trench. A similar conclusion has been reached by other authors for different trench regions; for example, Segawa and Tomoda (1976) in the Izu-Bonin region.

This model of the crustal structure was obtained by consideration of seismic refraction data from Shor et al. (1971) to help constrain crustal thickness. As their measurements were obtained about 60 nm to 300 nm south of the Eltanin 29 track, they were projected along strike to the ship profile. For the Southwest Pacific Basin no refraction data existed and a standard oceanic crust was assumed. In the standard model there was 5.5 km water, 2.0 km upper crust with density 2.7 gm/cm^3, 4.0 km lower crust with a 2.9 gm/cm^3 density overlaying mantle material with density 3.4 gm/cm^3. In the Southwest Pacific ˙ ˛sin any deviations from the standard model were fully compensated in an Airy manner. After inclusion of mantle densities, crustal structure landward of the trench was slightly adjusted until calculated gravity values agreed with observed data. Even though the refraction data was not perfectly coincident with the ship track, our final crustal model is in good agreement with seismic results. Table 2 has a comparison of the density model and seismic refraction values of Shor et al. (1971).

For both this crustal model and the entire model including the deeper mantle a spherical Earth method was used. Johnson and L˙tehiser (1972)

164

Figure 11

Table 2

Depth to base of layer

Number	Water	Depth	Sediment	Depth	Upper Crust	Depth	Intermediate	Depth	Lower Crust	Depth	
N24	1.50	4.29	2.15	5.43	6.02	6.73			6.90	10.04	Velocity
	1.03	4.00			2.70	6.50			2.90	10.40	Density
N25	1.50	4.28+	2.15	5.22	6.02	6.42+			6.90	12.62+	Velocity
	1.03	3.80+			2.70	6.25+			2.90	12.25	Density
N26	1.50	1.71	2.33	3.15+	5.14	5.85+	6.20	8.25	7.00	20.05+	Velocity
	1.03	2.00	2.50	3.00+	2.70	6.25+	2.80	8.00	2.90	18.75+	Density
N27	1.50	2.33	2.33	3.73	5.14	5.13	6.20	9.23	7.00	14.03	Velocity
	1.03	2.00	2.50	3.75	2.70	5.25	2.80	9.00	2.90	14.00	Density
N29	1.50	2.90	2.15	3.95	4.39	5.95			6.62	8.65	Velocity
	1.03	2.50	2.50	3.75	2.70	6.00			2.90	13.00	Density
N30	1.50	.68	2.81	2.17	5.42	9.07			6.92	19.07	Velocity
	1.03	1.00	2.50	2.50	2.70	9.50			2.90	16.50	Density
N32	1.50	8.37	2.15	8.38	5.54	13.98				14.10	Velocity
	1.03	9.25			2.70	11.50			2.90	13.00	Density

Velocity is in km/sec; density in gm/cm^3. Depth is in km.

†Note: These refraction stations occur at a discontinuity in the model and the stated depth to the density layer is an average value at that location.

Seismic refraction results are from Shor et al, 1971.

166

developed a technique for calculation of gravitational potential and attraction due to a spherical cap with polygonal sides. Geoid height is computed by dividing anomalous potential by normal gravity. In our utilization of this method the body is a input in cross section. Each segment is a spherical lamina which extends perpendicular to the cross section a certain distance. In our model the width was 2000 kilometers. Modeling was initially done assuming a plane two dimensional earth, later modeling only used spherical earth calculations. It was discovered that due to neglect of curvature the plane earth models gave erroneous values seaward of the trench. To insure that anomalous mass was being used, the gravitational effect of a standard Earth was subtracted. The standard model contained standard oceanic crust as previously defined and uppermost mantle 88.5 km thick with density 3.40 gm/cm^3. Only horizontal differences in density are important thus any effect of adiabatic compression was neglected. Our model thus contains no information on vertical density contrasts. All that is important are the lateral density differences.

Inclusion of mantle structure completes our final density model as shown in Figure 12. Crustal structure is identical to that which is illustrated in Figure 11. This model contains structures which were defined by seismic research. Seismicity studies have shown the presence of the Benioff zone (Sykes et al., 1969), while seismic velocity and attenuation anomalies (Mitronovas and Isacks, 1971; Oliver and Isacks, 1967) indicate this zone is caused by descending lithosphere. In our model ᐧ location of the descending lithospheric slab is based on the most recent seismicity study by Billington (1979). Thickness of the slab was constrained at 55 km down to a depth of 250 km and at 40 km for depths to 600 km. Studies of attenuation of shear waves indicate the

167

KERMADEC TRENCH

LANDWARD ← → SEAWARD

GEOID HEIGHT

GEOS-3
G1477

GRAVITATIONAL ATTRACTION OF ANOMALOUS MASS

EL29

3.40

3.35

3.50

3.37

Figure 12

168
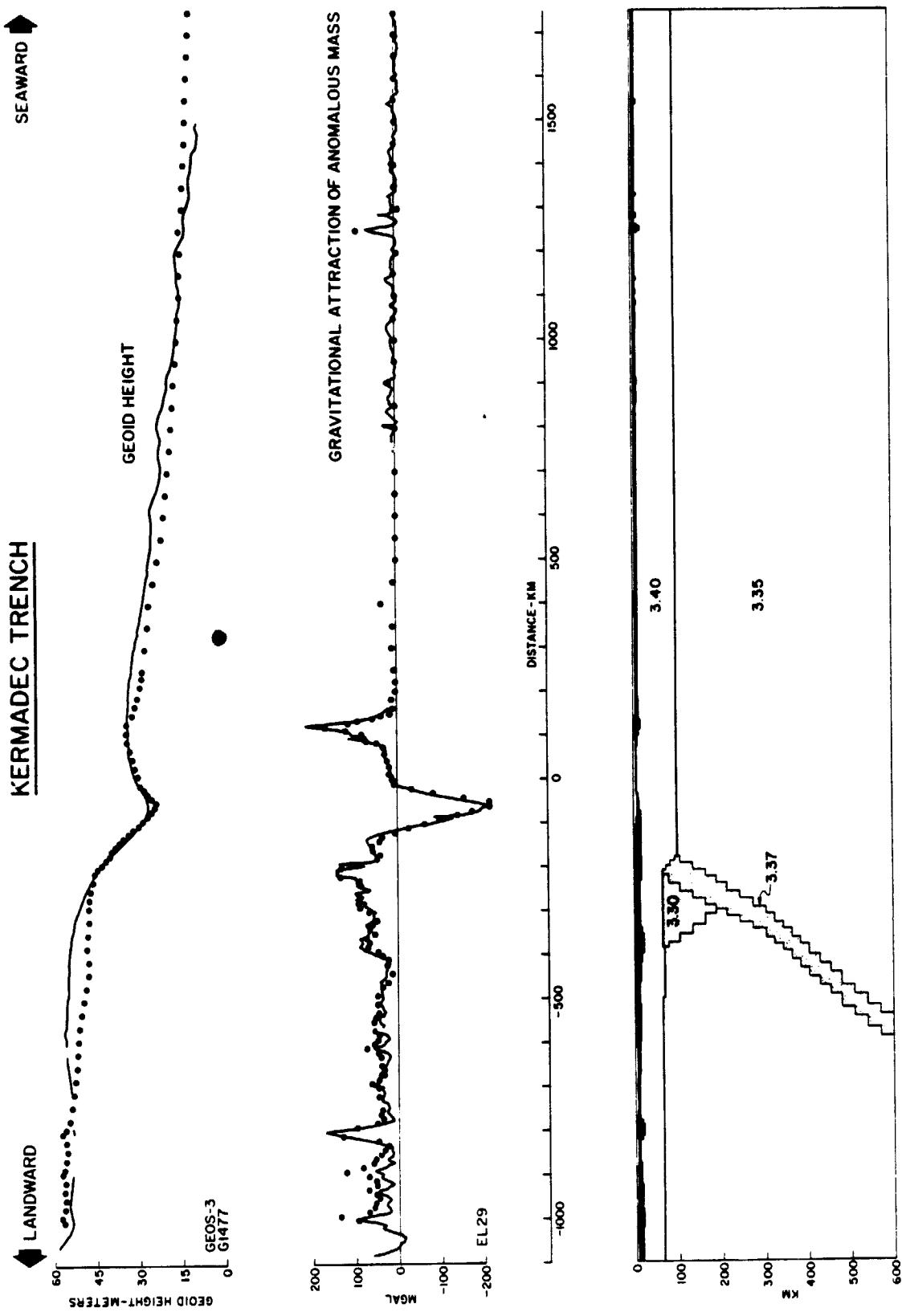
presence of a low Q zone above the slab near Tonga (Oliver and Isacks,
1967). Possibly this indicates an anomalous zone, thus a region of low
density material was included between 65 km and 180 km depth beneath the
island arc. This anomalous zone may extend to shallower depth or also
further landward. Because there was no definite seismic evidence concerning
its upper limit, this was not done.

Our procedure in modeling was to first use seismic refraction data
to constrain crustal structure. For the mantle location of a descending
slab and low Q Zone were then fixed, constrained as well as possible by
seismic studies. Density of the uppermost mantle was assumed to be
3.4 gm/cm^3 while underlaying mantle was fixed at 3.35 gm/cm^3. For the
mantle region densities within the slab and low Q Zone were varied, as
was the thickness of the uppermost mantle landward of the slab. Minor
adjustments in crustal structure were also made until calculated values
of geoid height and gravity agreed with the measurements.

Mantle structure in this final model has the following charac-
teristics. Depth to the lower density mantle landward of the trench is
35 km less than beneath the Southwest Pacific Basin. Thinning of the
uppermost mantle body is the mechanism for generating a mass deficit
within the mantle. This is because density of the lower density mantle
is .05 gm/cm^3 less than density of the uppermost mantle body at similar
depth. These lower average densities are the compensating mechanism for
the higher average densities at shallow depths landward of the trench.
However, this model is not fully compensated. At a depth of 100 km
there is a difference in pressure of 60 bars beneath the South Fiji
Basin compared to the Southwest Pacific Basin. There is an excess of
mass amounting to 7.3 x 10^4 gm/cm^2 in a column beneath the South Fiji
Basin relative to the Pacific Basin. This mass excess would correspond

169

to a +31 mgal anomaly over the South Fiji Basin, assuming a Bouguer approximation.

In this model the effect of the slab is relatively small. Compared to the surrounding mantle the slab has a density contrast of +.02 gm/cm^3. During our modeling procedure it was discovered that if the density contrast of the slab was +.05 gm/cm^3 or larger there would be no calculated low in the geoid over the trench axis, although there would still be a -190 mgal minimum above the axis. Use of the geoid data constrains the density contrast of the slab to be less than .05 gm/cm^3 relative to the surrounding material. In order to match the observed data, however, the density contrast was only +.02 gm/cm^3. Gravitational effect of the slab is illustrated in Figure 13. Both geoid and gravity are maximum above the slab with values of +13 m and +24 mgal respectively. Presence of lesser densities in the low Q zone negate the effect of the slab. Due to both bodies the total effect is -8 m and -38 mgal at maximum. As regards the effect of the slab, several conclusions are possible. There is a maximum density contrast of +.05 gm/cm^3 for the slab, although in our model it is required to be a lower value, +.02 gm/cm^3. Calculated geoid heights and gravity values due to the slab explain only a small portion of the observed anomaly. Presence of lesser densities in the low Q zone counteract the influence of the slab and result in a total effect which is slightly negative. As the net effect of both the slab and low Q zone explains only a small portion of the observed anomaly, it might be possible to construct a total model excluding those bodies. Such a possibility was not tested however, because there is definite seismic evidence for these bodies. But it is clear that from gravity and geoid evidence alone, the evidence of a dense slab cannot be inferred.

170

GRAVITATIONAL EFFECT OF DESCENDING SLAB

Figure 13

171
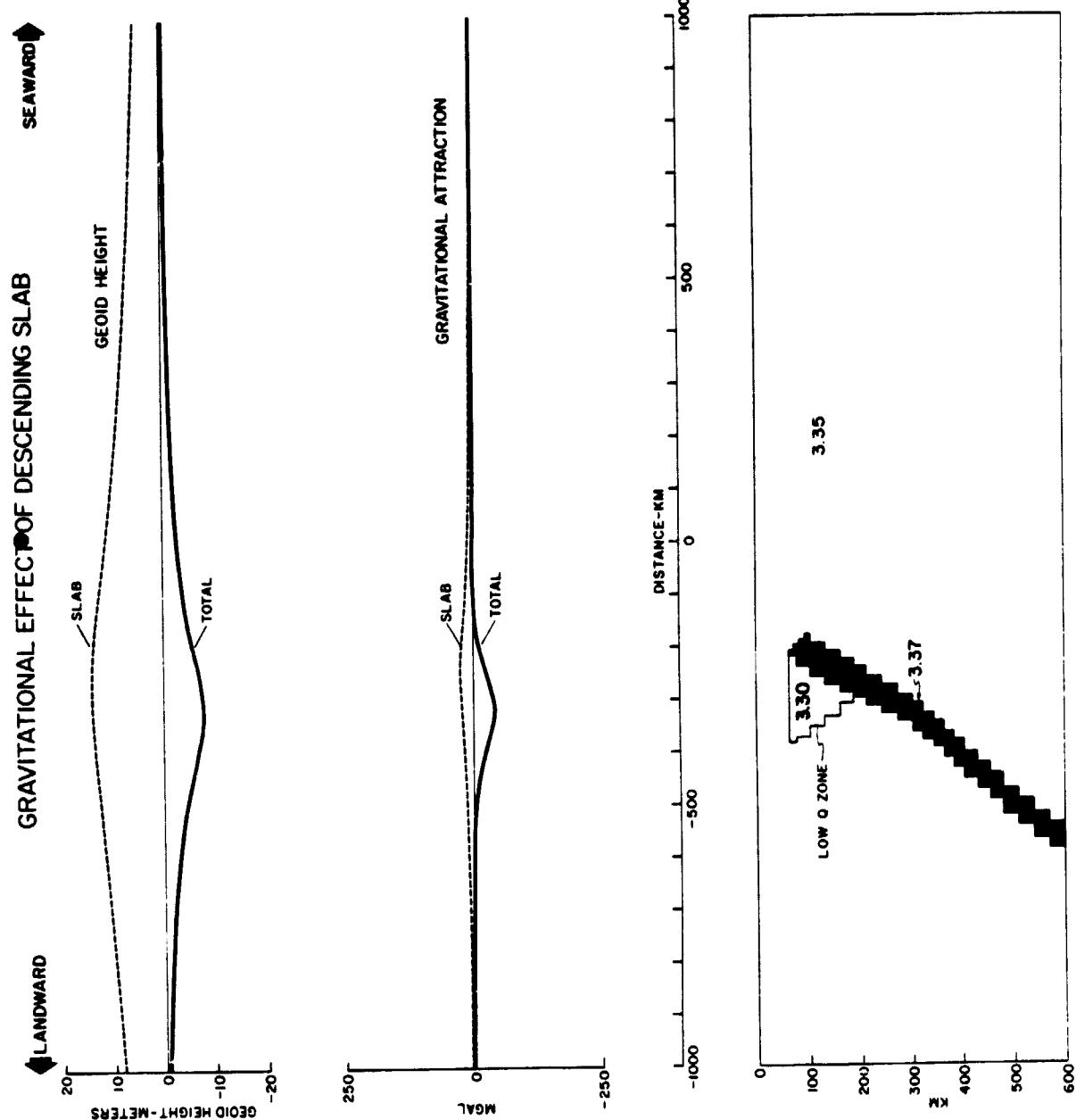
Summary and Conclusions

After observing GEOS-3 radar altimeter data, a characteristic geoid anomaly has been identified which occurs over all major deep-sea trenches. Seaward of the trench there is a gradual increase in geoid height with higher values near the trench and lower geoid heights progressively seaward. Slope of this very long increase ranges between 7 meters and 37 meters per 1000 km of distance. This gradual slope begins anywhere between 1000 and 3000 km seaward of the trench. In some regions the slope is concave downward as at the Aleutian Trench. Other areas have a slope which is fairly linear (Tonga Trench) or concave upward (Java Trench). Directly above the axis of trenches the geoid forms a narrow low from 100 to 200 km in width and anywhere between 3 m and 15 m in depth. Beginning at the base of the trench axis low there is a steep increase in geoid height of up to 30 m to a high region landward of the trench axis. Over some island arcs, for example the Bonin Islands or the Aleutian Arc, there is a distinct geoid high. This is between 5 and 10 m in amplitude. Landward of the trench axis the geoid has a generally high level relative to the deep sea basins. In this region however, slope of the geoid is variable. Behind the Aleutians the geoid has a slow decrease progressively landward, while over the Java Sea there is a progressive increase. In other regions the geoid remains fairly constant landward of the trench.

In utilizing data to study the Earth it is best to combine both geoid and gravity measurements. Gradual undulations of the geoid constrain densities deep within the Earth while gravity anomalies help determine crustal density. In using both types of data it is important to correct the free-air gravity anomaly for undulations of the geoid. Addition of a geoid correction term insures that gravity values are equal to the attraction of

172

the anomalous mass.

A density model of the Tonga-Kermadec region has been constructed which explains both the observed gravity and geoid values. Occurence of both a geoid and gravity high landward of the trench is caused by a dipolar type mass distribution. Landward of the trench axis, water depths are shallower when compared to the deep ocean basin. Thus at shallow depths there are higher densities relative to the Southwest Pacific Basin. An abnormally thick crust is not the mechanism for compensating these higher relative densities. Rather, in our model, compensation occurs by thinning of the uppermost mantle body. Beneath the South Fiji Basin lower density mantle material occurs at a depth 35 km shallower than beneath the Southwest Pacific Basin. These lower relative densities do not provide full compensation. At 100 km depth, pressure beneath the South Fiji Basin is 60 bars greater than beneath the Southwest Pacific Basin.

Perhaps one could associate the uppermost mantle body (density equal to 3.4 gm/cm^3) with lithosphere and the less dense, underlying mantle body, with asthenosphere. Using this terminology, partial compensation occurs within the mantle by a thinning of the lithosphere beneath the South Fiji Basin. According to Watts et al. (1977) age of the ocean floor in this region is approximately 30 m.y.b.p. If this were normal oceanic lithosphere, depth to the asthenosphere would be expected to be approximately 65 km (Forsyth, 1977). This coincides with our model and is an interesting observation, but most likely fortuitous.

In explaining the geoid anomaly any effect of the descending lithospheric slab is limited. Density contrast for the slab cannot exceed .05 gm/cm^3, but in our model is only .02 gm/cm^3. In our model

173

gravity values due to the slab are +24 mgal at maximum.

In the characteristic geoid anomaly at deep sea trenches there is an increase in geoid height as the trench is approached from the seaward side. This gradual sloping of the geoid seaward of the trench is entirely explained by the mass distribution landward of the trench axis. No anomalous mass (relative to landward regions) beneath the Pacific Basin is required to explain the gradual slope in the geoid.

During our modeling, it was found that it was quite difficult to match both gravity and geoid values. This is a qualitative observation that they provide complementary information. Also the geoid was quite sensitive to changes in mantle structure. If the depth to the lower density mantle material landward of the arc was altered by 5 km, there was a 10 m change in calculated geoid height. Yet in gravity this caused only a 10 mgal difference.

As in any study of the gravitational field there are limitations to our model. For example landward of the trench we cannot distinguish between thinning of an uppermost mantle body or lesser densities within the uppermost mantle. A thinner mantle body is the mechanism we utilized to produce a mass deficit at depth, but a seismic study would be necessary to confirm this conclusion. Similarly for the descending slab a qualification is necessary. For a slab thickness of 55 km thinning to 40 km, it was found that the density contrast could not be .05 gm/cm^3 or greater. Otherwise the geoid low above the trench axis could not be computed. If however a thicker slab were utilized, the density contrast would decrease. This data would not be able to distinguish between different thickness of descending lithospheric slabs. Lastly, in our model density within the mantle was assumed to have no lateral variation.

174

This is an untested assumption, but perhaps seismic surface wave studies in the ocean basins could detect any such variability within the mantle.

Study of the Tonga-Kermadec region raises interesting questions. Can the sloping geoid anomaly seaward of all trenches be explained by mass distribution landward of the trench axis? As this anomaly is variable in shape, perhaps mass heterogeneities are also required beneath the deep ocean basins.

Another enigma is the variability in geoid height landward of the trench axis. Can a model be constructed which would produce a variable geoid slope in this region? Our modeling seemed to suggest this would be possible by varying the horizontal extent of the dipolar type mass distribution.

Another intriguing result in our model is the excess pressure at 100 km depth landward of the trench. What are the forces required to sustain this model in equilibrium? Presumably any dynamic model which can generate such forces, would give rise to a geoid and gravity anomaly. In our model any variation in density within the asthenosphere was neglected, yet such differences would be required to maintain our model in equilibrium. Sleep (1975) has suggested a model for flow beneath island arcs. In his work topography was explained by stresses amounting to several hundred bars. It would be most interesting to construct a geophysical model capable of explaining any possible dynamic flow along with observed geoid and gravity anomalies.

CHAPTER VI ACKNOWLEDGMENTS:

References

Billington, S., The morphology and tectonics of the subducted lithosphere in the Tonga-Fiji-Kermadec region from seismicity and focal mechanism solutions, Ph.D. Thesis, Cornell University, 1979.

Bomford, B., GEODESY, Oxford University Press, Oxford, England, 561pp, 1962.

Bott, M.H.P., The mantle transition zone as possible source of global gravity anomalies, Earth and Planet. Sci. Lett., 11, 28-34, 1971.

Chapman, M.E., Techniques for interpretation of geoid anomalies, J. Geophys. Res., in press, 1979.

Chapman, M.E., and J. Bodine, Geoid corrections in marine gravimetry, J. Geophys. Res., in press, 1979.

Chapman, M.E., and M. Talwani, Comparison of gravimetric geoids with GEOS-3 altimetric geoid, J. Geophys. Res., in press, 1979.

Forsyth, D.W., The evolution of the upper mantle beneath mid-ocean ridges, Tectonophysics, 38, 89-118, 1977.

Griggs, D.T., The sinking lithosphere and the focal mechanism of deep earthquakes, in The Nature of the Solid Earth, (ed.) E.C. Robertson, McGraw-Hill, New York, N.Y., 361-384, 1972.

Grow, J.A., Crustal and upper mantle structure of the central Aleutian arc, Geol. Soc. Amer. Bull., 84, 2169-2192, 1973.

Grow, J.A., and C.O. Bowin, Evidence for high-density crust and mantle beneath the Chile Trench due to descending lithosphere, 80, 1449-1457, 1975.

Hanks, T.C., The Kuril Trench - Hokkaido Rise system: large shallow earthquakes and simple models of deformation, Geophys. J. R. astr. Soc., 23, 173-189, 1971.

Hayes, D.E., M. Talwani, R. Houtz, and W.C. Pitman III, Preliminary

    report of volume 22, U.S.N.S. Eltanin cruises 28-32, Technical

    Report No. CU-1-72, Lamont-Doherty Geological Observatory of

    Columbia University, 232 p., 1972.

Johnson, L.R., and J.J. Litehiser, A method for computing the

    gravitational attraction of three-dimensional bodies in a spherical

    or ellipsoidal Earth, J. Geophys. Res., 77, 6999-7009, 1972.

Karig, D.E., Origin and development of marginal basins in the Western

    Pacific, J. Geophys. Res., 76, 2542-2561, 1971.

Kaula, W.M., A tectonic classification of the main features of the

    Earth's gravitational field, J. Geophys. Res., 74, 4807-4826, 1969.

Mitronovas, W., and B. L. Isacks, Seismic velocity anomalies in the

    upper mantle beneath the Tonga-Kermadec Island Arc, J. Geophys.

    Res., 76, 7154-7180, 1971.

Ockendon, J.R., and D.L. Turcotte, On the gravitational potential and

    field anomalies due to thin mass layers, Geophys. J. R. astr. Soc.,

    48, 479-492, 1977.

Oliver, J., and B. Isacks, Deep earthquake zones, anomalous structures

    in the upper mantle, and the lithosphere, J. Geophys. Res., 72,

    4259-4275, 1967.

Ringwood, A.E., Phase transformations in descending plates and implications

    for mantle dynamics, Tectonophysics, 32, 129-143, 1976.

Segawa, J., and Y. Tomoda, Gravity measurements near Japan and study

    of the upper mantle beneath the oceanic trench-marginal sea tran-

    sistion zones, in The Geophysics of the Pacific Oc   Basin and

    its Margin, (ed): G.H. Sutton, M. Manghnani, R. Moberle, Geophysical

    Monograph 19, American Geophysical Union, Washington, D.C., 35-52,

    1976.

Shor, G.G., H.K. Kirk, and H.W. Menard, Crustal structure of the Melanesian Area, J. Geophys. Res., 76, 2562-2586, 1971.

Sleep, N.n., Stress and flow beneath island arcs, Geophys. J. R. astr. Soc., 42, 827-857, 1977.

Solomon, S., and S. Biehler, Crustal structure from gravity anomalies in the Southwest Pacific, J. Geophys. Res., 74, 6696-6702, 1969.

Sykes, L.R., B. Isacks, and J. Oliver, Spatial distribution of deep and shallow earthquakes of small magnitude in the Fiji-Tonga region, Bull. Seismol. Soc. Amer., 59, 1093-1113, 1969.

Talwani, M., J.L. Worzel. and M. Ewing, Gravity anomalies and crustal section across the Tonga Trench, J. Geophys. Res., 66, 1265-1278, 1961.

Vening Meinesz, F.A., Indonesian Archipelago: A geophysical study, Geol. Soc. Amer. Bull., 65, 143-164, 1954.

Watts, A.B., Gravity field of the Northwest Pacific ocean basin and its margin: Philippine Sea, Geol. Soc. Amer. Spec. Map and Chart Series MC-12, 1976.

Watts, A.B., A preliminary analysis of geoid heights derived from GEOS-3 altimeter data along the Hawaiian-Emperor Seamount Chain, submitted to J. Geophys. Res., 1979.

Watts, A.B., and M. Talwani, Gravity anomalies seaward of deep-sea trenches and their tectonic implications, Geophys. J. R. astr. Soc., 36, 57-90, 1974.

Watts, A.B., and M. Talwani, Gravity effect of downgoing lithospheric slabs beneath island arcs, Geol. Soc. Amer. Bull., 86, 1-4, 1975.

Watts, A.B., J.K. Weissel, and F.J. Davey, Tectonic evolution of the South Fiji marginal basin, in Island Arcs, Deep Sea Trenches and Back-Arc Basins, (ed.): M. Talwani and W.C. Pitman, American Geophysical Union, Washington, D.C., 419-427, 1977.

Yoshii, T., Features of the upper mantle around Japan as inferred from gravity anomalies, J. Phys. Earth, 20, 23-34, 1972.

A) Finite Vertical Sheet

$$N = \frac{G \cdot \sigma}{\gamma} \int_{z_1}^{z_2} \log_e \left\{ (x-x') + \left[(x-x')^2 + (y-y')^2 + (z-z')^2 \right]^{\frac{1}{2}} \right\} \Bigg|_{x_1}^{x_2} dz$$

This integral is of the form

$$\log_e \left\{ a + \left[B^2 + x^2 \right]^{\frac{1}{2}} \right\} dx$$

letting $u^2 = B^2 + x^2$, restricting $u > 0$ and integrating by parts we obtain

$$= \left[u^2 - B^2 \right]^{\frac{1}{2}} \log_e (a + u) - \int \left[\frac{u^2 - B^2}{a + u} \right]^{\frac{1}{2}} du$$

and after integrating again

$$= \left[u^2 - B^2 \right]^{\frac{1}{2}} \log_e (a + u) - \left[u^2 - B^2 \right]^{\frac{1}{2}}$$

$$+ a \log_e \left\{ \left[u^2 - B^2 \right]^{\frac{1}{2}} + u \right\} + \frac{(b^2 - a^2)}{\left[b^2 - a^2 \right]^{\frac{1}{2}}} \sin^{-1} \left[\frac{-1 \ (b^2 + au)}{|a + u| \ |b|} \right]$$

or finally

$$\int \log_e \left\{ a + \left[B^2 + x^2 \right]^{\frac{1}{2}} \right\} dx = x \log_e \left\{ a + \left[b^2 + x^2 \right]^{\frac{1}{2}} \right\} - x$$

$$+ a \log_e \left\{ x + \left[b^2 + x^2 \right]^{\frac{1}{2}} \right\} +$$

$$\left[b^2 - a^2 \right]^{\frac{1}{2}} \sin^{-1} \left[\frac{-1 \left\{ b^2 + a \ \left[b^2 + x^2 \right]^{\frac{1}{2}} \right\}}{\left| a + \left[b^2 + x^2 \right]^{\frac{1}{2}} \right| |B|} \right]$$

restricting $x > 0$

B) Two dimensional rectangle

$$N = - \frac{G \rho}{\gamma} \int_{z_1}^{z_2} \left\{ (y - y') \log_e \left[(y - y')^2 + (z - z')^2 \right] - 2y \right.$$

$$\left. + 2 |z - z'| \ \tan^{-1} \left[\frac{(y - y')}{|z - z'|} \right] \right\} \Bigg|_{y_1}^{y_2} dz$$

restricting $(z - z') > 0$ (this is the same integral as used for the two dimensional

sheet) and integrating

$$N = -\frac{G \rho}{\gamma} \left\{ (y-y') \left[(z-z') \log_e [(y-y')^2 + (z-z')^2] - 2z \right. \right.$$

$$\left. + 2 |y-y'| \; Tan^{-1} \; \frac{(z-z')}{|y-y'|} \right] - 2 \; y \; z$$

$$\left. + \int_{z_1}^{z_2} 2 \; (z-z') \; Tan^{-1} \; \frac{(y-y')}{(z-z')} \; dz \right\} \left| \begin{matrix} y_2 \\ \\ \\ y_1 \end{matrix} \right.$$

This last integral is of the form

$$\int z \; Tan^{-1} \; \frac{a}{z} \; dz$$

Letting $w = \frac{a}{z}$ then integrating by parts we find

$$\int \frac{1}{w^3} \; Tan^{-1} \; w \; dw = -\frac{1}{2} \left\{ (1 + \frac{1}{w^2}) \; Tan^{-1}(w) + \frac{1}{w} \right\}$$

so finally

$$N = -\frac{G \rho}{\gamma} \left\{ (y-y') \left[(z-z') \log_e [(y-y')^2 + (z-z')^2] \right. \right.$$

$$\left. - 2z + 2 |y-y'| \; Tan^{-1} \; \frac{(z-z')}{|y-y'|} \right] - 2 \; y \; z$$

$$\left. + [(z-z')^2 + (y-y')^2] \; Tan^{-1} \; \frac{(y-y')}{(z-z')} + (z-z') \; (y-y') \right\} \left| \begin{matrix} y_2 \\ \\ \\ y_1 \end{matrix} \right. \left| \begin{matrix} z_2 \\ \\ \\ z_1 \end{matrix} \right.$$

C) Two dimensional polygon

For the $_i$th side of the polygon we have

$$n_i = \int \left\{ (y-y') \log_e [(y-y')^2 + (z-z')^2] - 2 \; (y-y') \right.$$

$$\left. + 2 \; (z-z') \; Tan^{-1} \; \frac{(y-y')}{(z-z')} \right\} \; dz$$

and we integrate along a linear line segment defined by $z = m_i \; y + b_i$;

assuming m_i and $1/m_i$ are not zero we obtain

$$n_i = \int_{z_{i-1}}^{z_i} \left\{ [(z-B_i)/m_i - y'] \log_e \left[\left(\frac{z-B_i - y'}{m_i} \right)^2 + (z-z')^2 \right] \right.$$

$$\left. -2 \left(\frac{z-B_i - y'}{m_i} \right) + 2 (z-z') \operatorname{Tan}^{-1} \left[\frac{\left(\frac{z-B_i - y'}{m_i} \right)}{(z-z')} \right] \right\} dz$$

$$\text{where } m_i = \frac{z_i - z_{i-1}}{y_i - y_{i-1}}$$

$$B_i = z_i - m_i y_i$$

First part of the integral is of the form $\int x \log_e (a+bx+cx^2) \, dx$ and is a standard integral. Third part of the integral is of the form $\int x \operatorname{Tan}^{-1} [(Cx + D)/x] \, dx$. Letting $u = (Cx + D)/x$ and integrating by parts, this becomes

$$- \frac{D^2}{2} \left[- \frac{\operatorname{Tan}^{-1} u}{(u-c)^2} + \int \frac{du}{(u-c)^2 (1+u^2)} \right]$$

After the final integration we find for the third part

$$\int x \operatorname{Tan}^{-} [(Cx+D)/x] = \frac{1}{2} \left\{ x^2 \operatorname{Tan}^{-1} [(Cx+D)/x] \right.$$

$$- \frac{C D^2}{(1+C^2)^2} \log_e \left[\frac{(1+C^2) x^2 + 2CDx + D^2}{D^2} \right]$$

$$\left. + \frac{D x}{(1+C^2)} + \frac{(1-C^2) D^2}{(1+C^2)^2} \operatorname{Tan}^{-1} [(Cx+D)/x] \right\}$$

Thus formula 23 can be integrated to obtain formula (24).

In evaluating the line integral the following special cases are also important.

Case (a). If $m_i = 0$, then dz is zero and consequently n_i is also zero.

Case (b). If $1/m_i = 0$ then y is constant along the line segment and the line integral (23) is written as:

$$n_i = \int_{Z_{i-1}}^{Z_i} \Big\{ (y_i-y') \log_e [(y_i-y')^2 + (z-z')^2]$$

$$-2 (y_i-y') + 2 (z-z') \operatorname{Tan}^{-1} \frac{(y_i-y')}{(z-z')} \Big\} \, dz$$

This is identical in form to the integral for the two dimensional rectangle and is solved in an identical fashion.

Case (c). If the extension of the line segment passes through the observation point (when $B_i/m_i + y' = 0$) then the line integral (23) is written as

$$n_i = \int_{Z_{i-1}}^{Z_i} \Big\{ \frac{Z}{m_i} \log_e [(1+1/m_i^2) z^2] - 2 z/m_i$$

$$+ 2 Z \operatorname{Tan}^{-1} (1/m_i) \Big\} \, dz$$

$$\text{assuming } Z' = 0, \ Z > 0$$

This is easily integrated to become equation (27).

D)   Three dimensional polyhedron. For the j'th line segment of the i'th facet we have, after integrating equation 36 by parts and rearranging

$$L_j^i = \frac{G\rho\theta_i}{2\gamma} \left\{ n \log_e\Big\{ (m_j n+\zeta_j^\circ) + [(m_j n+\zeta_j^\circ)^2 + n^2+\theta_i^2]^{\frac{1}{2}} \Big\} \right\} \Bigg|_{n_i}^{n_{i+1}}$$

$$- \int_{n_i}^{n_{i+1}} \frac{n^2 \, d\eta}{n^2+\theta^2} + \int_{n_i}^{n_{i+1}} \frac{\zeta_j^\circ \, d\eta}{[(m_j n+\zeta_j^\circ)^2+n^2+\theta_i^2]^{\frac{1}{2}}}$$

184

$$- \int_{\eta_i}^{\eta_{i+1}} \frac{(m_j \theta_i^2 \eta + \zeta_j^\circ \theta_i^2) \, d\eta}{(\eta^2 + \theta_i^2) \left[(m_j \eta + \zeta_j^\circ)^2 + \eta^2 + \theta_i^2\right]^{1/2}} \Bigg\}$$

The first integral is independent of the path of integration, thus when L_j^i is summed over all line segments for a closed path this integral will sum to zero. Consequently, we ignore this term. The second integral is in a standard form. To solve the third integral the substitution is made.

$$\eta = \frac{m_j^2 \theta_i^2 - \zeta_j^{\circ 2} x}{(m_j \zeta_j^\circ)(x+1)}$$

This will transform the last integral into

$$\left[m_j^2 \theta_i^2 + \zeta_j^{\circ 2}\right]^{1/2} m_j^2 \theta_i^2 \zeta_j^\circ \int \frac{dx}{(\zeta_j^{\circ 2} x^2 + m_j^2 \theta_i^2) \left[\zeta_j^{\circ 2} x^2 + m_j^2 \theta_i^2 + m_j^2 (m_j^2 \theta_i^2 + \zeta_j^{\circ 2})\right]^{1/2}}$$

which is a standard form and can be integrated. This same integral (36) has also been solved for gravity problems by Barnett (1976) and Paul (1974).

1. Report No. NASA CR-156859	2. Government Accession No.	3. Recipient's Catalog No.
4. Title and Subtitle Shape of the Ocean Surface and Implications for the Earth's Interior - Final Report of GEOS-3 Results		5. Report Date February 1979
		6. Performing Organization Code
7. Author(s) Michael Edward-Dewey Chapman, Manik Talwani, Hans-Gert Kahle, John H. Bodine		8. Performing Organization Report No.
		10. Work Unit No.
9. Performing Organization Name and Address Lamont-Doherty Geological Institute Columbia University Palisades, New York 10964		11. Contract or Grant No. NAS6-2519
		13. Type of Report and Period Covered Contractor Report
12. Sponsoring Agency Name and Address National Aeronautics and Space Administration Wallops Flight Center Wallops Island, Virginia 23337		14. Sponsoring Agency Code

15. Supplementary Notes

16. Abstract

Traditionally, mapping of the marine geoid has utilized gravimetric techniques. For the Indian Ocean a new set of 1°x1° mean free-air anomalies is used to construct a gravimetric geoid by Stokes' formula.

Utilizing such 1°x1° geoid comparisons have been made with GEOS-3 radar altimeter estimates of geoid height. Most commonly there are constant offsets and long wavelength discrepancies between the two data sets; there are many probable causes including radial orbit error, scale errors in the geoid, or bias errors in altitude determination. Across the Aleutian Trench the 1°x1° gravimetric geoids do not measure the entire depth of the geoid anomaly due to averaging over 1° squares and subsequent aliasing of the data. After adjustment of GEOS-3 data to eliminate long wavelength discrepancies, agreement between the altimeter geoid and gravimetric geoid is between 1.7 and 2.7 meters in rms errors. errors.

For purposes of geological interpretation techniques are developed to directly compute the geoid anomaly over models of density within the Earth.

In observing the results from satellite altimetry it is possible to identify geoid anomalies over different geologic features in the ocean. For example, a feature that is characteristic of the geoid in the vicinity of deep sea trenches includes a gradual long increase as the trench is approached from the ocean basin, a narrow low over the trench axis, and a high but with variable slope landward of the trench.

For the Tonga-Kermadec region a modeling study of the densities within the Earth indicates the following conclusions about the origin of the geoid anomaly. Landward of trench, in this model, the ocean depths are shallower than in the deep ocean basin. Thus for these depths average densities are higher relative to the Southwest Pacific Basin. Lower relative densities occur deeper within the mantle. These lesser densities partially compensate the higher values at shallow depth. This is a dipolar type, layered mass distribution and is the fundamental cause of the relatively high geoid values landward of the trench. The effect of the descending lithosphere is only of secondary importance in explaining this geoid anomaly. A gradual slope of the geoid seaward of the trench axis is explained as simply due to the mass distribution landward of the trench.

17. Key Words (Suggested by Author(s)) GEOS-3 gravity geoid altimetry	18. Distribution Statement Unclassified - unlimited STAR category - 42,46,48		
19. Security Classif. (of this report) Unclassified	20. Security Classif. (of this page) Unclassified	21. No. of Pages 202	22. Price*